



Universidade de Brasília
Instituto de Geociências
Programa de Pós-graduação em Geologia

**STRAIN LOCALIZATION IN THE LOWER
OCEANIC CRUST: THE ATLANTIS BANK
OCEANIC CORE COMPLEX, SOUTHWEST
INDIAN RIDGE – IODP EXPEDITION 360**

RHANDER TAUFNER ALTOÉ

Doctorate Thesis N° 191

Supervisor: Prof. Dr. Luis Gustavo Ferreira Viegas

Brasília | September 09 | 2022



Universidade de Brasília
Instituto de Geociências
Programa de Pós-graduação em Geologia

STRAIN LOCALIZATION IN THE LOWER OCEANIC CRUST: THE ATLANTIS BANK OCEANIC CORE COMPLEX, SOUTHWEST INDIAN RIDGE – IODP EXPEDITION 360

RHANDER TAUFNER ALTOÉ

Thesis presented to the Post-Graduation Program in Geology – Geosciences Institute – IG at the University of Brasília – UnB as a partial prerequisite to obtain the title of Doctor of Philosophy in Geology.

Concentration Area: Mineralogy and Petrology

Supervisor: Prof. Dr. Luis Gustavo Ferreira Viegas

Examination Panel:

Prof. Dr. Caio Arthur Santos (IG/UnB)

Prof. Dr. Andreia Tommasi (Montpellier University)

Prof. Dr. Leonargo Lagoeiro (Federal University of Paraná)

Prof. Dr. Catarina Laboure Benfica Toledo (Substitute IG/UnB)

TT224s TAUFNER ALTOE, RHANDER
 STRAIN LOCALIZATION IN THE LOWER OCEANIC CRUST: THE
 ATLANTIS BANK OCEANIC CORE COMPLEX, SOUTHWEST INDIAN RIDGE –
 IODP EXPEDITION 360 / RHANDER TAUFNER ALTOE; orientador
 LUIS GUSTAVO FERREIRA VIEGAS. -- Brasília, 2022.
 109 p.

 Tese(Doutorado em Geologia) -- Universidade de Brasília,
 2022.

 1. Atlantis Bank. 2. Oceanic core complex. 3. Strain
 localization. 4. Fluid-rock interaction. 5. Shear zones. I.
 FERREIRA VIEGAS, LUIS GUSTAVO, orient. II. Título.

(...)

Tive muita dô di num tê nada
pensano qui esse mundo é tud'tê
mas só dispois di pená pelas istrada
beleza na pobreza é qui vim vê.
Vim vê na procissão u Lôvado-seja
o malassombro das casa abandonada
côro di cego nas porta das igreja
i o êrmo da solidão das istrada.
Apois pro cantadô i violêro
só hai treis coisa nesse mundo vão:
amô, furria, viola, nunca dinhêro.
Viola, furria, amô, dinhêro não.

Violêro, Elomar Figueira Melo

Agradecimentos

Toda a minha trajetória acadêmica e de pesquisa foi realizada em instituições públicas, com dinheiro público. Espero poder retornar esse investimento para a sociedade, contribuindo com ensino e pesquisa de qualidade.

Ao meu orientador, Gustavo Viegas, obrigado por ser presente, profissional, ético e, sobretudo, compreensivo. Obrigado por respeitar meus limites e dar-me liberdade para desenvolver meu trabalho, sempre aparando as arestas para induzir-me à maturação científica. Agradeço-te pela sensibilidade em me motivar a continuar quando duvidei da minha capacidade. Vida longa aos milonitos.

Às minhas inclusões fluidas em cristais de diamante, Talita, Raissa, Camila e Rafael Grapper, obrigado por serem ausência-presente nesses quatro anos de doutoramento. Vocês, para mim, 'são como haste fina, que qualquer brisa verga, mas nenhuma espada corta'.

Aos meus amigos Fábio Popinigis e Rafael Bitencourt, obrigado por me acolherem nessa minha breve estadia no quadrado, pelos conselhos e noites de vinho regadas a balbúrdia e reflexões sobre a vida durante a nefasta pandemia. Obrigado, Rafa, por ter feito parte do ciclo que, hoje, julgo ser o mais importante da minha vida. Sua presença foi fundamental e, certamente, tornou todo o processo mais doce. 'A amizade é um santo remédio'.

A todos os docentes, técnicos, profissionais de limpeza, alimentação e segurança da Universidade de Brasília, muito obrigado por manterem a ordem na casa. Em especial, à Alice Falchetto, pelo excelente trabalho junto à secretaria do PPG-UnB. Obrigado pelo afeto materno todas as vezes em que me encontrava em apuros por conta das obrigações acadêmicas.

À Dra. Claudia Trepman, por me receber em seu laboratório no período sanduíche em que estive em Munique, na Alemanha, com projeto financiado pelo DAAD, e por ser um exemplo de cientista, para mim. Agradeço aos meus colegas de trabalho na Ludwig-Maximilians Universität, Fabian Delefant e Lisa Brückner, pelas discussões geológicas e recepção calorosa na cultura alemã. À minha amiga Clarisa Margarita, pelos banhos gelados no rio Isar, passeios de bicicleta, longas conversas nos cafés de Munique, e por me apresentar à cultura sul-bavariana. Ao querido colega Johannes, pelas longas discussões sobre o sentido da vida (a qual nunca chegamos à conclusão alguma: talvez esse seja o sentido da vida). Obrigado por me mostrar os Alpes do norte austríaco aos olhos de um ciclista.

À Brasília, cidade que me acolheu mesmo antes eu não a conhecendo pessoalmente. Obrigado por me ensinar a gostar de pequi, de casas sem muros, de terra vermelha manchando os pés, de pôr do sol em dias de inverno, de café sem açúcar, de arquitetura moderna, de simetrias, de cobogó; obrigado por me ajudar a crescer asas, torná-las fortes, mas não para voar a esmo: ‘carcará...quando vê roça queimada, sai voando, cantando, carcará...vai fazer sua caçada’. Mesmo apartado de ti, Brasília, ainda sinto cheiro de dama-da-noite nas tuas noites úmidas de verão, de tua florada de ipês anunciando o fim do inverno e o começo do inferno, dos teus flamboyants apaixonados. Obrigado, Brasília, por ser um oásis de concreto, de verde, de vida, no nosso planalto central. ‘(...) Eu não como pão. O trigo para mim é inútil. Os campos de trigo não me lembram coisa alguma. E isso é triste! Mas tu tens cabelos cor de ouro. O trigo, que é dourado, fará lembrar-me de ti. E eu amarei o barulho do vento no trigo (...)’.

À música popular brasileira, por me contar a ‘verdadeira história e a verdadeira sociologia do Brasil’. Obrigado por me salvar de mim e do mundo; por me dar um lampejo de esperança nesse ‘trem do desejo, que penetra na noite escura, e que vai abrindo sem censura o ventre da morena Terra’.

Aos meus pais e irmãos – Arlindo, Ione Ágata, Renan e Taísa -, obrigado por todo apoio afetivo, moral, intelectual... por serem exemplo de vida... Obrigado pela honestidade, resiliência e incentivo. Obrigado por me darem a liberdade de seguir meus passos, mesmo sabendo que as consequências nem sempre são doces. Aos meus sobrinhos, Liz, Ian, Léo e Maya, obrigado por resgatarem em mim esse amor inocente, que beira a bobice. De ora avante, sigamos fazendo bagunça.

Manoel de Barros, *gradicado* por me mostrar a cor no canto dos pássaros: ‘Tenho sede de passarinho, pedra e rã’.

O presente trabalho foi realizado com apoio da Coordenação de Aperfeiçoamento de Pessoal de Nível Superior - Brasil (CAPES) - Código de Financiamento 001.

CONTENTS

1	Introduction and relevance	12
2	Objectives	15
3	Oceanic core complexes in slow-spreading ridges	17
3.1	The Atlantis Bank oceanic core complex	19
4	Methods	22
4.1	Quantitative microstructural analysis.....	22
4.2	Elemental chemistry mapping and pressure, temperature conditions of deformation	23
5	Results.....	28
5.1	Manuscript #1: Deformation mechanisms of granulite-facies mafic shear zones from hole U1473A, Atlantis Bank, Southwest Indian Ridge (IODP Expedition 360)	28
5.2	Manuscript #2: Interplay between crystal-plasticity, fracturing and dissolution- precipitation creep in lower-crustal ultramylonite from hole U1473A, Atlantis Bank, Southwest Indian Ridge	47
6	Final remarks	104
	References.....	105

Abstract

Detachment faulting has been hypothesized as the main process of tectonic spreading in slow-spreading mid-ocean ridges, leading to exhumation of lower crustal rocks interlayered with pristine upper-mantle aggregates through large-scale normal faulting, namely ocean core complexes (OCC). Although many models have been proposed for the rooting of detachments and the exhumation of ocean core complexes, the interplay between deformation and fluid-assisted metamorphic reactions during mylonitization and unroofing of OCC is still poorly constrained. Particularly, the role of ductile shear zones at depth and their potential pathways for melt and/or fluids in enhancing phase transformation during large-scale faulting is still contentious. Thus, the influence of fluids on the modes which strain is localized in the oceanic crust is yet to be constrained in terms of their impact on the mechanical behavior of the lithosphere.

In this contribution, we have investigated the mechanical characteristic of lower crustal rocks through a detailed tectono-metamorphic analysis of gabbro mylonites recovered in the hole U1473A from the Atlantis Bank ocean core complex, Southwest Indian Ridge (IODP Expedition 360), to better understand strain localization processes during uplift of the high-temperature ocean crust, taking into account the influence of fluids as a potential weakening mechanism.

We have shown that mylonites in gabbroic shear zones localize deformation at granulite facies conditions by a combination of mechanical fragmentation and viscous flow (e.g., dislocation and diffusion creep) in the presence of fluids. The percolating fluids promote syn-kinematic hydration reaction products (i.e., amphibole), and the amount of amphibole produced is intimately linked to the degree of strain the rock experienced. Our results evidence that fluids contribute to the development of fine-grained shear zones in 'dry' gabbroic rocks and play a crucial role on the overall mechanical behavior of the lower oceanic crust. Hence, the rheology of the lower crust at slow-spreading ridges would be best modeled with flow laws for polymineralic aggregates, taking into account the role of water in promoting reaction-softening. Such fluid-rock interactions are complex and indicate the way strain is distributed in the footwall of oceanic core complexes during large-scale, detachment faulting and exhumation of the lower crust/upper mantle boundary.

Resumo

Falhas de *detachment* têm sido hipotetizadas como a principal estrutura que permite acreção crustal em dorsais meso-oceânicas de espalhamento lento, levando à exumação de rochas da crosta inferior, intercaladas com agregados primitivos do manto superior, denominados de complexos de núcleo metamórfico oceânicos (OCC). Embora diversos modelos propõem um contraste reológico que permite a nucleação de falhas de *detachment* em profundidade, a interação entre deformação e transformação mineral assistida por fluidos durante milonitização e exumação de OCC ao longo das falhas de *detachment* ainda é pouco compreendida. Particularmente, o papel de zonas de cisalhamento dúcteis em profundidade como condutos para percolação de fluidos, favorecendo interação fluido-rocha e transformação mineral, ainda é controverso. Logo, a influência dos fluidos nos processos pelos quais a deformação se localiza na crosta oceânica, e seu impacto no comportamento mecânico da litosfera, precisa ser melhor investigado.

Nesta contribuição, investigamos os processos de localização da deformação na crosta oceânica inferior através de uma análise tectono-metamórfica detalhada em gabro milonitos do complexo de núcleo metamórfico do Atlantis Bank (Sudoeste da Cordilheira Índica), recuperados no furo U1473A, alvo da Expedição IODP 360. Nosso objetivo é melhor compreender os mecanismos de deformação responsáveis pelo soerguimento da porção de alta temperatura da crosta oceânica através de zonas de cisalhamento, levando em conta a influência dos fluidos no enfraquecimento mecânico da litosfera.

Nossos resultados mostram que milonitos em zonas de cisalhamento gabróicas localizam a deformação em condições de fácies granulito por uma combinação de fragmentação mecânica e fluxo viscoso (e.g., fluências por deslocamento e difusão) na presença de fluidos. Interação-fluido rocha promove enfraquecimento mineral e formação de anfibólio, favorecendo mistura de fases e mantendo fluência por difusão. Reações metamórficas assistidas por fluidos são mais pervasivas e localizadas em rochas intensamente deformadas (i.e., ultramilonito), indicando um *feedback* positivo entre deformação e metamorfismo. Nossos resultados indicam que fluidos contribuem para o desenvolvimento de zonas de cisalhamento em rochas gabróicas anidras, e desempenham um papel crucial no comportamento mecânico da crosta oceânica inferior. Desse modo, a reologia dessa porção da litosfera seria melhor modelada a partir de leis de fluxo aplicadas em agregados poliminerálicos, levando em conta o papel da água promovendo mecanismos de enfraquecimento mineral. Tais interações fluido-rocha são complexas e indicam a forma

como a deformação é distribuída na base dos complexos de núcleo metamórfico oceânicos durante falhamento de *detachment* e exumação do limite crosta inferior/ manto superior.

CHAPTER 1

1 Introduction and relevance

Slow-spreading oceanic ridges comprise more than 60% of present-day ocean floor (Blackman et al., 1998). These areas are mainly composed of ocean core complexes (OCC), which are denuded elevations of the lower oceanic crust/upper mantle boundary through large-scale detachment faulting (Tucholke et al., 1998). The interplay between tectonic faulting and magmatic activity leads to the exposure of pristine sectors of the deep crust and consists in one of the main mechanisms of seafloor spreading (Karson, 1990; Smith and Cann, 1993).

Several models have been proposed for the nucleation of OCC at the boundary of detachment faults, either invoking rooting of the detachment at i) the brittle-ductile transition (Tucholke et al., 2001, Schroeder and John, 2004), ii) at a melt-rich crustal zone (Dick et al., 1991, Dick et al., 2000), or iii) at an alteration/serpentinization front (Escartin et al., 2003). The available database of recovered rocks from these complexes displays a varied spectrum of mafic lithologies comprising serpentinized peridotite, gabbro, diabase and basalt (MacLeod et al., 2009), with several degrees of deformation ranging from high-temperature (> 600°C) solid-state to low-temperature (<400°C) semi-brittle to brittle fabrics (Hansen et al., 2013).

Unravelling the processes involved in the formation of OCC and the mechanisms of nucleation of detachment faulting is critical to the understanding of the rheology of the crust/mantle boundary, and has direct implications for plate tectonic processes. Even though there are several models proposed for the rooting of detachments and consequent exposure of domal core complexes (see Ildefonse et al., 2007 for a review), the interplay between magmatism, deformation and fluid-rock interactions is yet not fully understood.

In particular, the role of pre-existing structures at depth (ductile shear zones) and their consequent exploitation as potential pathways for melt and/or fluids during large-scale faulting is still debatable. Major mechanical anisotropies (faults) generated at shallow structural levels can potentially propagate into shear zones at depth and this can lead to feedbacks between brittle and ductile strain regimes; deformation mechanisms and the overall rheological strength of the crust-mantle boundary would therefore be a response of strain localization processes due to melt/fluid rock interactions (Handy et al., 2007). However, it is still not clear how fluids weaken the lower ocean crust because these rocks are often erased during the geodynamic cycle, hindering access to samples that can tell us the deformation history in such structural levels.

In this context, the International Ocean Discovery Program (IODP) Expedition 360 aimed to drill the ocean crust to reach the boundary between the lower crust and upper mantle (Moho) at the Atlantis Bank massif. The hole U1473A recovered ~780 meters of gabbro exposing a thick sequence of gabbroic rocks extensively deformed under high-temperature solid-state flow that are subsequently overprinted by semi-brittle to brittle fabrics in the upper levels of the sequence. These data suggest that the Atlantis Bank was nucleated at high-temperature and later reworked at low-grade conditions during uplift through detachment fault (Dick et al., 2019; Miranda and John, 2010). Thus, the Atlantis Bank provides a “natural laboratory” to study deformation mechanisms active in shear zones during unroofing of the lower crust/upper mantle boundary.

CHAPTER 2

2 Objectives

This contribution seeks to address two main questions: i) the processes responsible for strain localization during detachment faulting of the Atlantis Bank OCC, and ii) the role of shear zones as anisotropic channels for fluid circulation along the gabbroic lower crust. To answer those questions, we have conducted a detailed petrostructural study in mylonitic and ultramylonitic shear zones that occur in the lower gabbroic section (>520 mbsf of the core section) of Site U1473A, the target of IODP Expedition 360. The lower sections of the core exhibit several mesoscale shear zones in which variable degrees of high-temperature mylonitization are observed. We seek to combine microstructures, deformation mechanisms and geochemical studies of fluid-rock interaction processes in order to better understand the mechanical behavior of the oceanic crust during detachment faulting at (de)coupled lower crust/upper mantle boundaries. Since the structural characteristics of these rocks seem to be heavily influenced by fluid-assisted mineral reactions, we aim to investigate the possible influence of water and/or percolating fluids in the overall rheological weakening of the lower crust during shear zone nucleation and subsequent development.

CHAPTER 3

3 Oceanic core complexes in slow-spreading ridges

Seafloor spreading at slow (rates of 5.5–2.0 cm/y) and ultra-slow (rate < 2.0 cm/y) spreading ridges (Fig. 1) is dominantly accommodated by tectonic processes with transient magmatic activity (e.g., Ildefonse et al., 2007). During ocean floor extension, the brittle upper crust fractures along normal faults, and ongoing spreading exposes ductile material from deeper levels of the lithosphere, resulting in exhumation of lower crustal and upper mantle rocks in the footwall of the low-angle detachment normal fault (Fig. 2). The resulting structure is a core complex (Figs. 1 and 2), and the detachment fault associated to it is interpreted as the main structure responsible for spreading of the oceanic crust, being therefore the major tectonic expression in (ultra)slow spreading ridges (Smith and Cann, 1993; Cannat et al., 2006; Smith et al., 2006).

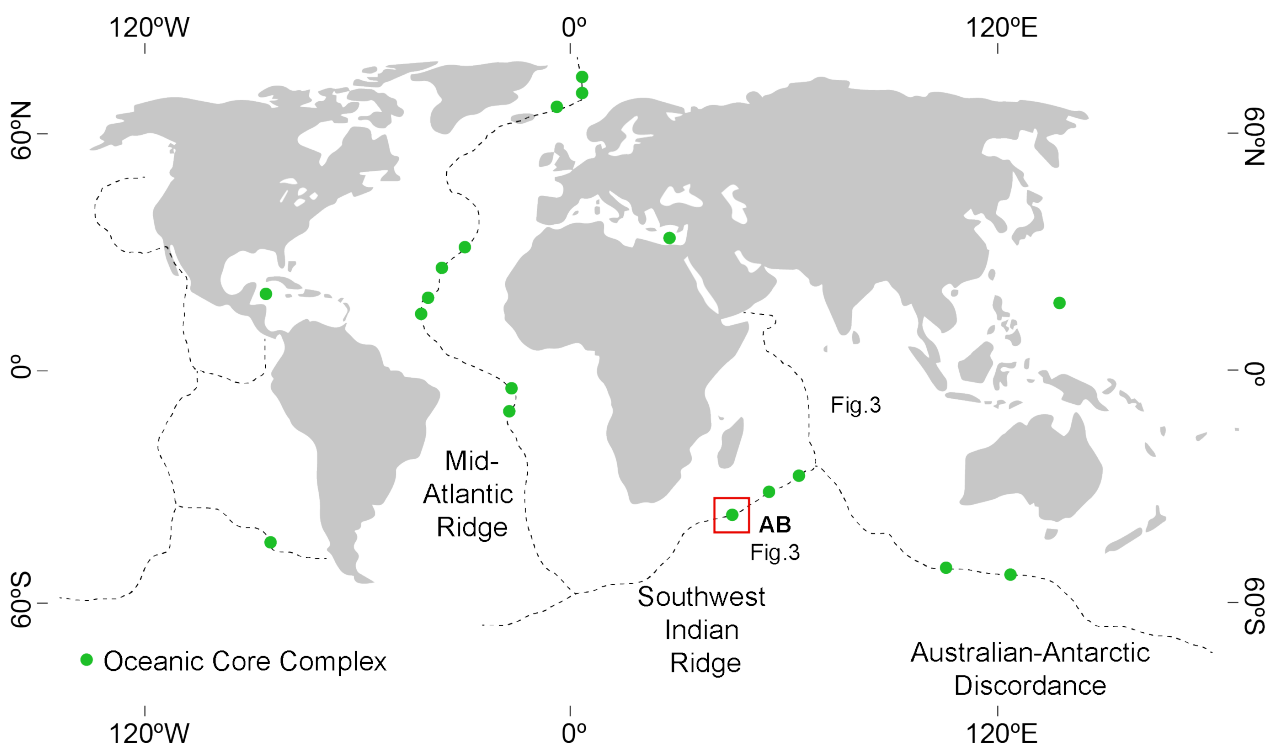


Figure 1. Map of the world showing the locations of some slow and ultra-slow spreading ridges and the development of oceanic core complexes in oceans that were sampled via the Ocean Drilling Program (ODP) or the Integrated Ocean Drilling Program (IODP). The Atlantis Bank – AB – is highlighted in the red box and details are shown in Figure 3. Modified from Whitney et al. (2013).

Oceanic core complexes have a mild convex upward shape (Ranero and Reston, 1999; Canales et al., 2004) bounded by large scale normal detachment faults that become increasingly steeper at depth, down to the brittle-ductile transition or magma chambers (Tucholke et al., 1998; Fig. 2). The upper flat part of detachments often forms dome-like structures with prominent striations parallel to the spreading direction (e.g., Cann et al.,

1997; MacLeod et al., 2002). The asymmetry of core complexes (Fig. 2) is in contrast with the conventional view of mid-ocean ridges as symmetric structures dominated by volcanic systems (Brun et al., 2018). Modelling shows that the main physical parameters determining the final asymmetry of a core complex are: i) the development of a detachment fault, and ii) the asymmetric growth of the metamorphic dome (i.e., the core itself; Lavier et al., 1999; Mezri et al., 2015). Regardless of the parameters used to model the ridges (e.g., rate of symmetry during displacement, thickness of the crust, partial melting in the lower crust, temperature, pressure), the continued motion on the detachment fault rotates the footwall around an upper rolling hinge into a sub horizontal orientation (Fig. 2). Phase transitions controlled by pressure, temperature and local availability of fluids show a positive feedback between the asymmetry of the detachment fault and strain localization as a result of strain softening (Mezri et al., 2015).

Strain localization during detachment faulting and exhumation of oceanic core complexes is accompanied by distributed and gently dipping, high-temperature ductile shear zones that accommodate deformation by viscous flow (e.g., Cannat, 1991; Schroeder and John, 2004; Mehl and Hirth, 2008; Miranda et al., 2010). With progressive exhumation of the lower crust to higher crustal levels and lower temperature conditions, deformation tends to localize in schistose shear zones associated with pervasive semi-brittle to brittle deformation under fluid-present conditions. The previous high temperature fabrics are overprinted by fluid-assisted mineral reactions promoting reaction softening and cataclastic flow (e.g., Schroeder and John, 2004; Miranda et al., 2010).

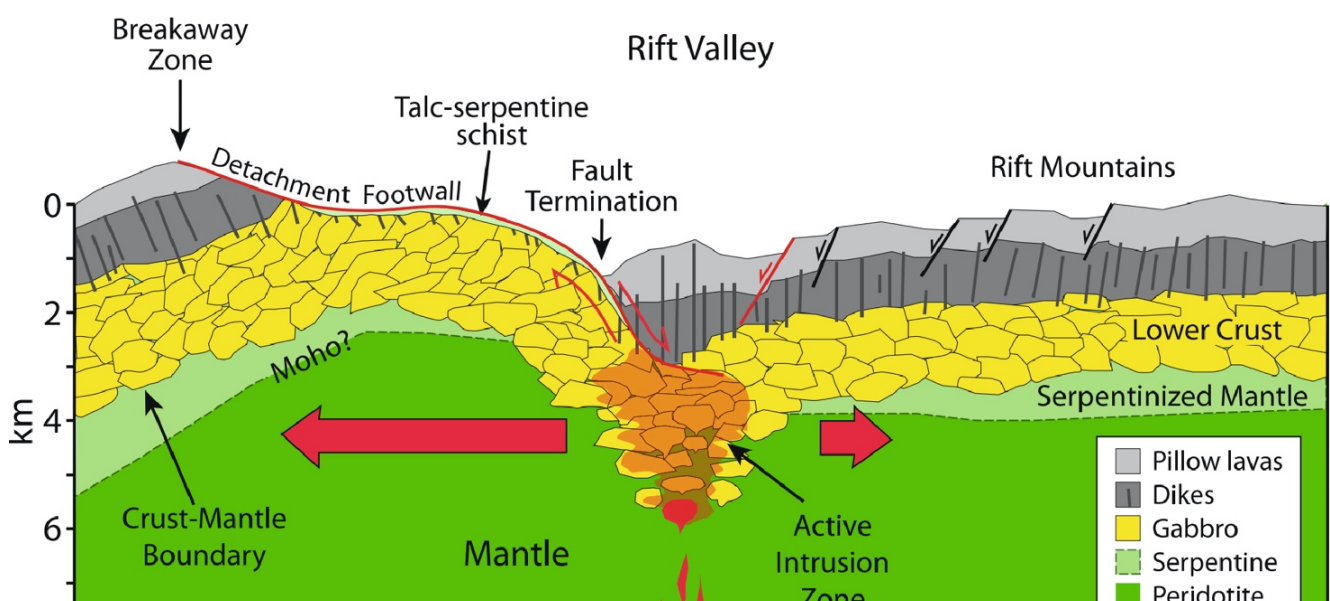


Figure 2. Idealized formation of an oceanic core complex bounded by an oceanic detachment fault. Red arrows show spreading asymmetry similar to that documented at Atlantis Bank. Note the progressing rolling of the upper part of the footwall into a subhorizontal position (rolling hinge). From Dick et al. (2019).

3.1 The Atlantis Bank oceanic core complex

The Atlantis Bank OCC (Fig. 3a) is a 40 km long by 20 km wide massif elongated in the N–S direction that lies at ~720 meters below sea level. It is located ~110 km south of the present-day Southwest Indian Ridge (Dick et al., 2019; Fig. 1) near the center of the ridge segment between the Atlantis II Transform and the non-transform discontinuity at 57°40'E (Fig. 3; Dick et al., 1991; Stakes et al., 1991; Matsumoto et al., 2002; Natland and Dick, 2002; Hosford et al., 2003; Schwartz et al., 2005; Baines et al., 2007; Baines et al., 2008). The irregular topography of the Atlantis Bank platform is a result of flexural uplift following extension of the Southwestern Indian Ridge on the outward dipping, moderate–high-angle normal faults that bound it, at ~ 10 to 13 Ma. (Baines et al., 2003).

The atypical elevation of the Atlantis Bank makes it a prospective target for drilling and submersible sampling (John et al., 2004; Schwartz et al., 2005), providing a unique opportunity to investigate the evolution of deformation processes responsible for accommodating long-living ocean plate motion through detachment faulting.

IODP Site U1473A is located at ~710 meters below sea-level and was drilled on top of Atlantis Bank during Expedition 360, in 2016 (Fig. 1b-c). It lies 1-2 km away from two previous Sites: 1.508 m deep Site 735B, drilled during two legs in 1987 (Shipboard Scientific Party, 1989) and 1997, (Shipboard Scientific Party, 1999a, 1999b) and 158-m deep Site 1105A, drilled in 1998 (Pettigrew et al., 1999). Site U1473A drilled 789.7 m, recovering ~ 469.4 m of core with average recovery of 59% (Dick et al., 2019). Drilled rocks mainly comprise olivine gabbro (76.5%), gabbro (14.6%) and oxide-rich gabbro (7.4%; oxide content >2%), cut by several slightly to non-deformed felsic veins, microgabbros and minor diabase (Fig. 4a; see Dick et al. 2019 for a complete description of the lithologies recovered in Site U1473A). Grain size and modal mineral variation define the igneous layering which is frequently obliterated by crystal-plastic deformation. The gabbroic rocks bearing Fe-Ti oxides are usually associated with shear zones, and the presence of oxides is attributed to the percolation of late-stage melts through an olivine gabbro framework. (Dick et al., 2016).

Crystal-plastic deformation is heterogeneous, with 1- to 10-m scale zones of dominantly porphyroclastic fabrics separated by relatively weakly deformed gabbros (Fig. 4b). Mylonite zones in the order of one meter-scale to tens of meters-scale and thin ultramylonites are present throughout the hole (Figs. 4b and 4c). The dip of the crystal plastic foliation is typically shallow, in the range of 10 to 40°, although locally the dip can progressively increase and steepen to vertical.

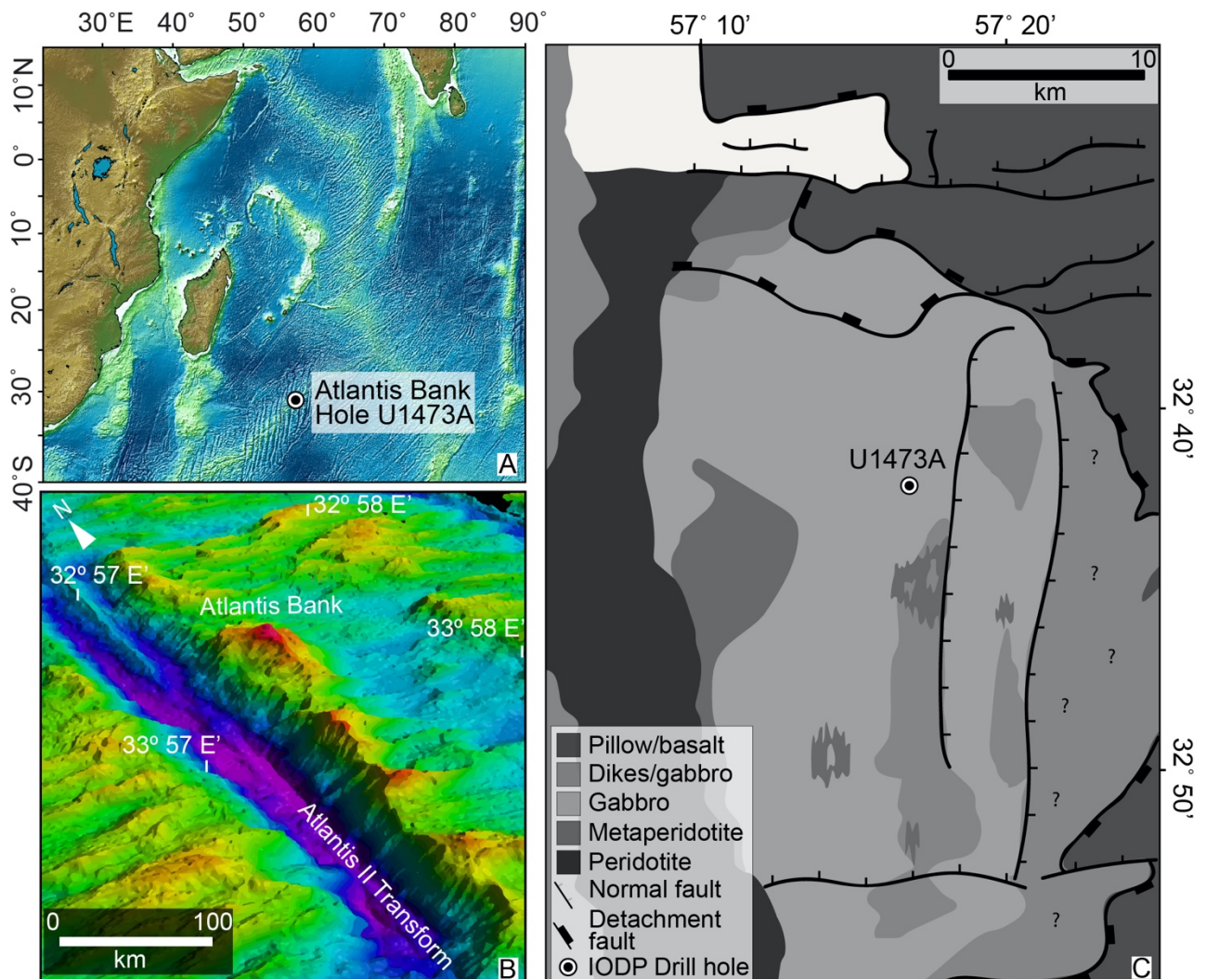


Figure 3 Geological setting of the Atlantis Bank, Southwest Indian Ridge: (a) Satellite image of the Southwest Indian Ridge with the location of Site U1473A; (b) 3D bathymetric reconstruction of the Atlantis Bank at the edge of the Atlantis II Transform fault; (c) Simplified geological map (based on drill core data and ocean topography of the seafloor) of the Atlantis Bank showing main rock units at Site U1473A. The core of the massif is mostly composed by gabbro (modified from Dick et al., 2000).

CHAPTER 4

4 Methods

We analyzed mylonites and ultramylonite in shear zones from the lower section of Site U1473 (Fig. 4a), mainly composed of olivine-gabbro deformed under lower crustal, high-temperature conditions (Dick et al., 2019). These fabrics are best preserved at the lower ~500 mbsf length of the core (Figs. 4a and 4b), which has not been affected by late brittle-ductile deformation (Dick et al., 2019). Cores of deformed gabbro were drilled and cut into two identical half pieces. Structures were studied on the split face of the working half of the core (Fig. 4c). Orientation of the core faces could be obtained if a piece was cut directly perpendicular to their strike. Otherwise, two apparent dips and dip azimuth measurements were necessary in order to acquire a true dip value. For preparation of thin sections, samples were cut normal to foliation and, whenever possible, parallel to the XZ plane of the strain ellipsoid. We prepared five thin sections of the gabbroic shear zones (Fig. 1d): four mylonite samples (Figs. 4a and 5) collected at depth intervals of 519.6-529.95 mbsf (58R), 626-636.26 mbsf (69R), 683.7-694.26 mbsf (78R) and 712.8-721.35 mbsf (81R), and one ultramylonite sample (68R) collected at depths intervals of 616.3-626 mbsf (Figs. 4a and 5).

The methods of study consisted of (Fig. 6): i) quantitative microstructural characterization of the deformed mineral assemblage; ii) chemical determination of major elements distribution during deformation in the presence (or absence) of fluids; iii) thermodynamic modelling to constrain the conditions at which the microfabrics developed. This multidisciplinary approach will contribute to a better understanding of the ways strain is accommodated and further localized into shear zones during detachment faulting associated with plate motion at slow-spreading ridges

4.1 Quantitative microstructural analysis

Deformation microstructures in the bulk mineral assemblage of the selected samples were investigated through detailed microstructural analysis with light microscopy and scanning electron microscopy (SEM), coupled with Electron Backscatter Diffraction (EBSD) and Energy Dispersive X-ray spectrometry (EDS) in order to correlate microstructures with chemical composition. The Electron Backscatter Diffraction (EBSD) technique consists of a detector coupled to a Scanning Electron Microscope (SEM-EBSD) that images the crystallographic preferred orientations of a given sample. An electron-charged beam hits the sample in a fixed stage in which a 70° tilted position of the sample allows for the electrons to scatter around the sample surface. Backscattered electrons are captured by a phosphor camera and then compared with a mineralogical database present in the SEM computer. In

a rock, interaction of the electron beam with the crystallographic planes of the rock-forming minerals generates diffraction patterns known as Kikuchi bands. By analyzing Kikuchi bands patterns emitted from crystallographic planes in a crystal, it is possible to derive grain-scale processes such as deformation and recrystallization of a certain mineral phase (Prior et al., 1999).

The crystallographic information constrained from the deformed mineral phases in the gabbro mylonites will allow us to infer the main deformation mechanisms active during strain localization. For example, in the dislocation creep regime, the movement of dislocations along specific crystallographic planes and directions in the mineral produces a strong crystallographic preferred orientation (CPO; e.g., Mehl and Hirth, 2008). Conversely, aggregates deforming via diffusion creep usually lack a well-defined CPO because the diffusion of material away from or at the grain boundary usually involves a rotational component that weakens any pre-existing CPO (e.g., Mori et al., 1998). Thus, the combination of the observed microstructures and chemical analysis with a detailed EBSD information is a reliable way to assess deformation processes in deformed rocks.

4.2 Elemental chemistry mapping and pressure, temperature conditions of deformation

The cartography of full thin sections by elemental chemistry mapping is possible due to wavelength dispersive spectroscopy (WDS) detectors that identify specific wavelengths associated with known chemical elements, which directly correlates with the qualitative distribution of major elements in a given sample (Goldstein, 2003). Maps of the chemical composition of rocks and of selected microstructural sites were acquired in order to investigate the chemical composition of major mineral phases involved in deformation. Equilibrium temperature was estimated through the application of two-phase mineral geothermometers that use chemical compositions of main mineral phases. Electron Probe Micro Analysis (EPMA) of areas previously imaged with elemental maps were performed in order to obtain quantitative chemical compositions that were used to calculate temperature estimates. To further constrain the conditions of pressure and temperature of deformation, we combined the modal abundance of the mineral assemblage with the distribution of major elements in thermodynamic modelling of the equilibrium conditions of the deformed/recrystallized mineral assemblage. The results are shown as pressure and temperature graphs of stable mineral assemblages in a wide range of conditions with isopleths narrowing the stability field of the deformed gabbro.

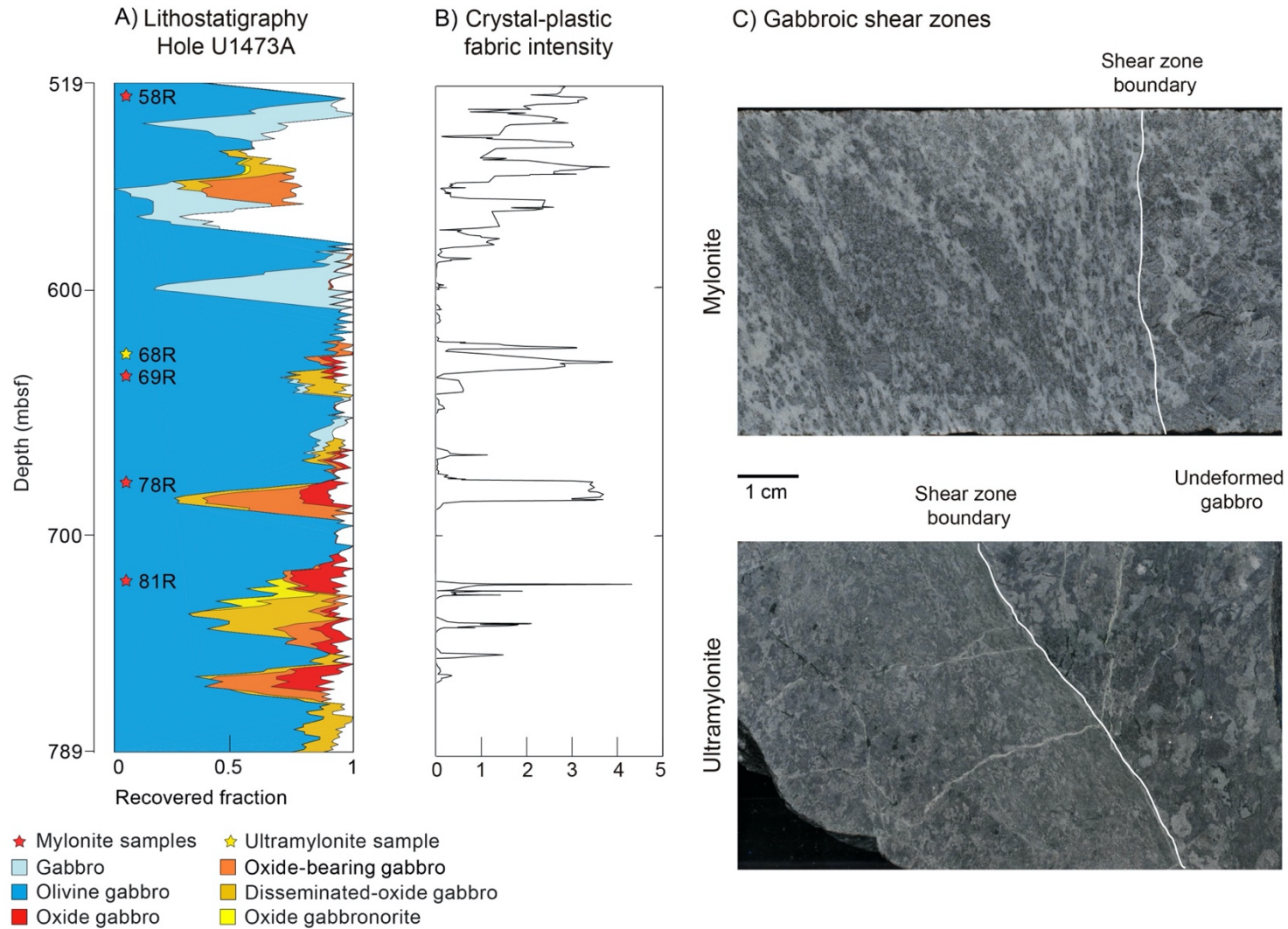
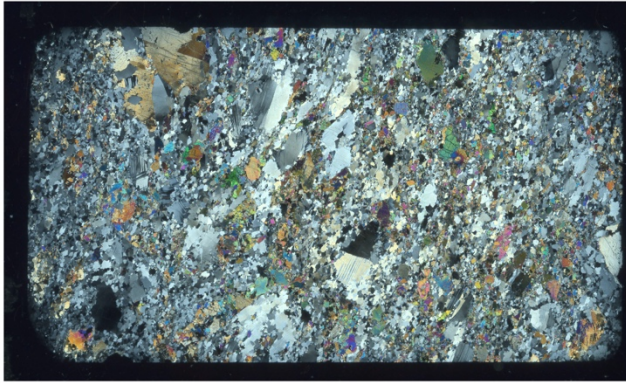
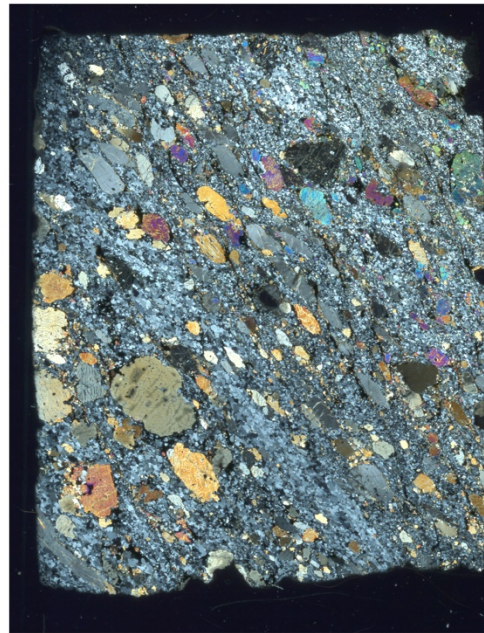


Figure 4. Shear zone samples collected for this study: (a) Lower, high-temperature sector of Hole U1473A showing gabbro compositions recovered in drill cores and location of the analyzed samples (star symbols); (b) Crystal-plastic fabric intensity downhole. Scale bar at the horizontal axis: 0: undeformed, 1: weakly-deformed; 2: recrystallized; 3: Porphyroclastic; 4: mylonitic; 5: ultramylonitic. Gaps in the profile relate to undeformed or not recovered intervals (Dick et al., 2019); (c) Mesoscopic shear zones showing mylonite and ultramylonite in abrupt contact with undeformed gabbro.

★ 58R



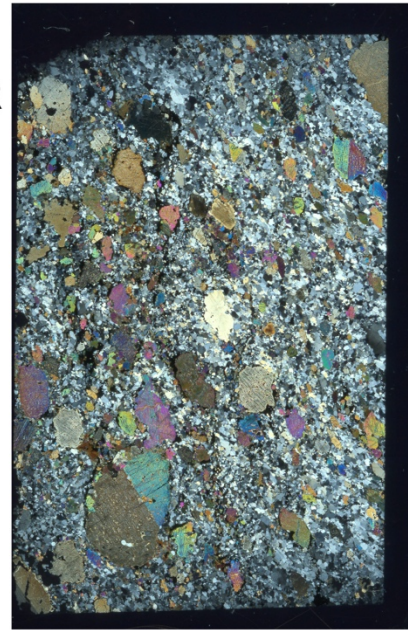
★ 78R



★ 68R



★
81R



★ 69R



- ★ Mylonite samples
- ★ Ultramylonite sample

Figure 5. Scanned images showing the samples under thin sections through cross-polarized light. The position of the samples in respect to the depth of the Hole U1473A is outlined in Figure 4a. Length of each thin section is approximately 3 cm.

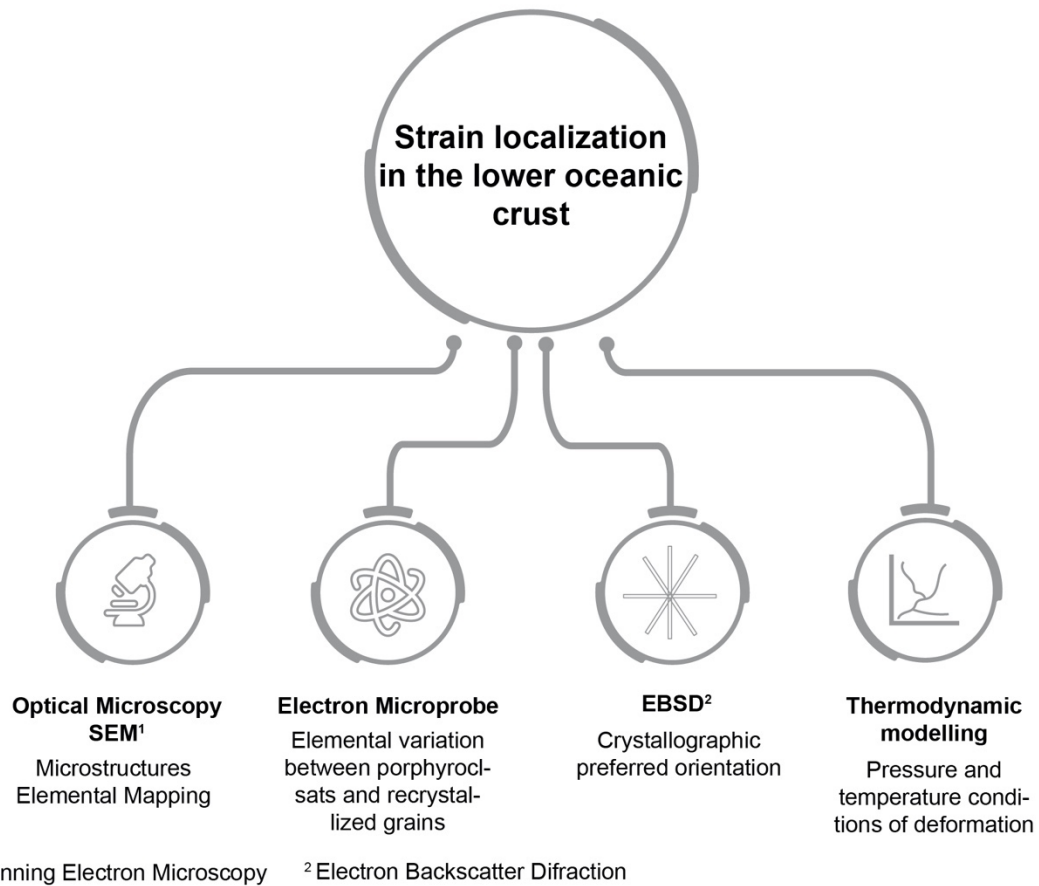
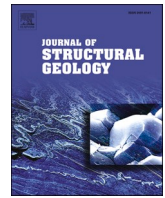


Figure 6. Diagram showing the techniques used to answer the guiding questions in this study. See text for a brief explanation of the methods and techniques.

CHAPTER 5

5 Results

5.1 Manuscript #1: Deformation mechanisms of granulite-facies mafic shear zones from hole U1473A, Atlantis Bank, Southwest Indian Ridge (IODP Expedition 360)



Deformation mechanisms of granulite-facies mafic shear zones from hole U1473A, Atlantis Bank, Southwest Indian Ridge (IODP Expedition 360)

Rhander Taufner^{a,*}, Gustavo Viegas^a, Frederico Meira Faleiros^b, Paulo Castellan^a, Raylline Silva^a

^a Institute of Geosciences, University of Brasília, Brasília, Brazil

^b Institute of Geosciences, University of São Paulo, São Paulo, Brazil

ARTICLE INFO

Keywords:

Atlantis bank
Oceanic core complex
Dislocation creep
Melt-rock interaction
Detachment faults

ABSTRACT

Lower-crustal shear zones from hole U1473A (IODP Expedition 360) were studied via quantitative microstructural analysis and thermodynamic modelling to constrain deformation conditions during detachment faulting. Porphyroclasts of clinopyroxene and orthopyroxene, plagioclase and olivine are included in a fine-grained, polyphase matrix that contains plagioclase-rich layers. Microfractures occur in orthopyroxene, and core-mantle structures are common in all porphyroclasts. Crystallographic fabrics in clinopyroxene clasts indicate activation of (010)[001] slip system, whereas the rimming neoblasts show activity of both (010)[001] and (001)[100]. Fabrics of plagioclase-rich layers suggest the activation of the (010)[100] slip system. Phase mixing and weak crystallographic fabrics in the polyphase matrix point to oriented-growth during diffusion-assisted grain boundary sliding. Thermodynamic modelling indicates that the gabbroic shear zones formed at ~900–920 °C and 2.2–2.7 kbar, under melt-present conditions, and re-equilibrated down to 835 °C during exhumation, as indicated by hornblende–plagioclase thermometry. Our results suggest that deformation in the lower parts of Atlantis Bank was accommodated by a combination of brittle fragmentation and viscous flow during in-situ melt-consumption back-reaction. Such mechanisms effectively resulted in strain localisation in fine-grained, polyphase shear zones that contributed to the weakening of the ocean crust during detachment faulting and subsequent exhumation of the Atlantis Bank core complex.

1. Introduction

Detachment faults at slow and ultraslow mid-ocean spreading ridges (<55 mm/year) can accommodate large offsets (>10 km) and result in the exposure of otherwise deep crustal gabbro and mantle peridotite at the sea floor (Blackman et al., 1998; Cann et al., 1997; Escartín et al., 2003; Smith et al., 2006; Tucholke et al., 1998). The exposed footwalls of detachment faults are typically dome-shaped, bathymetrically elevated and record corrugations that are parallel to plate motion direction (Cann et al., 1997; Escartín et al., 2003; MacLeod et al., 2009; Tucholke et al., 1998). These structures are termed oceanic core complexes (OCCs) and constitute the major tectonic feature in slow and ultra-slow-mid-ocean spreading ridges (Cannat et al., 2006; Smith et al., 2006; Smith and Cann, 1993).

Several models have been proposed for the nucleation of OCCs at the boundaries of detachment faults, either invoking rooting of the detachment at i) the brittle-ductile transition (Schroeder and John,

2004; Tucholke et al., 2001), ii) a melt-rich crustal zone (Dick et al., 2000), or iii) an alteration/serpentinization front (Escartín et al., 2003). The available database of recovered rocks from these complexes display a varied spectrum of mafic lithotypes, comprising serpentinised peridotite, gabbro, diabase and basalt (MacLeod et al., 2002), which show a full set of structures ranging from high-temperature (>600 °C) solid-state to low-temperature (<400 °C) semi-brittle to brittle deformation (Hansen et al., 2013).

During progressive detachment faulting and unroofing of OCCs, the main processes attributed to strain localisation from high- to low-temperature conditions can be summarised as follows: i) distributed, gently dipping ductile gabbroic shear zones that accommodate deformation by crystal plasticity and diffusion creep at granulite to upper amphibolite facies conditions (Cannat, 1991; Mehl and Hirth, 2008; Miranda and John, 2010; Schroeder and John, 2004) and ii) localised, semi-brittle to brittle deformation in schistose shear zones associated with pervasive, lower amphibolite to greenschist facies fluid-rock interaction.

* Corresponding author.

E-mail address: rhander.altoe@gmail.com (R. Taufner).

<https://doi.org/10.1016/j.jsg.2021.104380>

Received 22 March 2021; Received in revised form 19 May 2021; Accepted 26 May 2021

Available online 1 June 2021

0191-8141/© 2021 Elsevier Ltd. All rights reserved.

Dissolution-precipitation creep, reaction softening and cataclastic flow overprint all previous ductile fabrics (Miranda and John, 2010; Schroeder and John, 2004).

The Atlantis Bank (Southwest Indian Ridge, Fig. 1) exposes a sequence of gabbros extensively deformed under high-temperature solid-state flow and subsequently overprinted by semi-brittle to brittle fabrics in the upper levels (Dick et al., 2019a). These characteristics suggest that the Atlantis Bank OCC was nucleated at high-temperature and later reworked at low-grade conditions during uplift through the

detachment fault (Miranda and John, 2010). This site was the target of the recent IODP Expedition 360 (Southwest Indian Ridge Lower Crust and Moho), which aimed to drill into the crust/mantle transition in order to ultimately reach the Moho at a depth of ~4–5 km (Dick et al., 2019b).

Unravelling the processes involved in the formation of OCCs and the mechanisms of nucleation of detachment faulting is critical to better understand the rheology of the crust/mantle boundary, and has direct implications for plate tectonic processes. Even though there are several

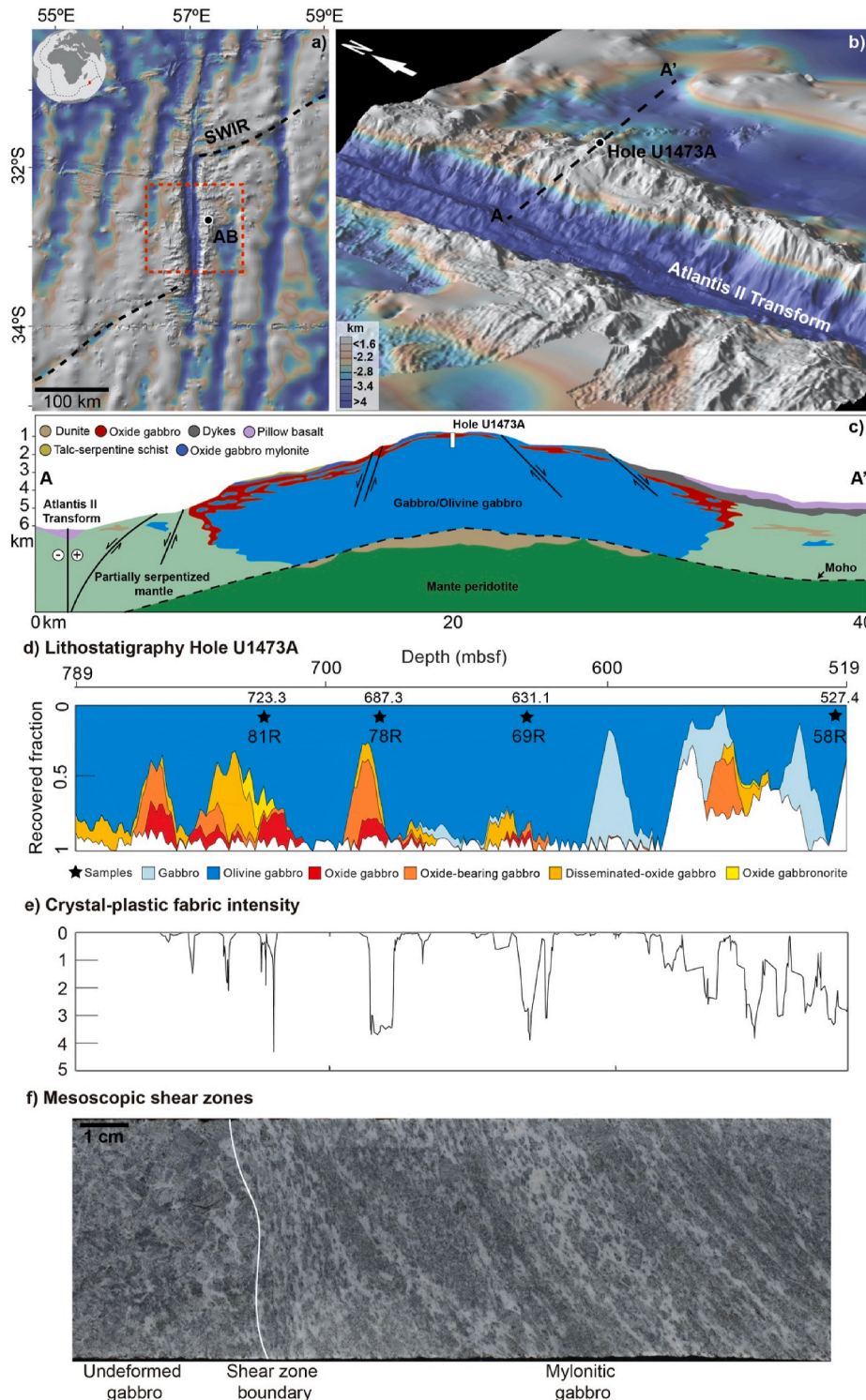


Fig. 1. Geological setting of the Atlantis Bank, Southwest Indian Ridge, and shear zones sampled in this study. AB: Atlantis Bank; SWIR: Southwest Indian Ridge. (a) Location of the Atlantis Bank. (b) Location of hole U1473A at the edge of the Atlantis II Transform fault. Figures (a) and (b) made with GeoMapApp (<https://geomapapp.org>, last access January 2021; Ryan et al., 2009). (c) East-west schematic profile of Atlantis Bank based on cross-sections from Dick et al. (2019a). The morphological aspects of sea floor are derived from ODP and IODP drill cores, and the interpretation of geology at depth and the seismic-derived location of Moho are based on current knowledge (modified from Dick et al., 2019a). (d) Lower, high-temperature sector of hole U1473A showing gabbro compositions recovered in drill cores (Dick et al., 2016). Black stars represent the analysed sample locations and corresponding depths (upper part of the column) from which they were cored. (e) Crystal-plastic fabric intensity downhole. Scale bar at the vertical axis: 0: undeformed; 1: weakly-deformed; 2: recrystallised; 3: porphyroclastic; 4: mylonitic; 5: ultramylonitic. Gaps in the profile relate to undeformed or unrecovered intervals (Dick et al., 2016). (f) Hand sample (81R) from a representative asymmetric and anastomosing, discrete set of shear bands in contact with undeformed gabbro.

models proposed for the rooting of detachments and the consequent exposure of domal core complexes (Ildefonse et al., 2007), the interplay between magmatism, deformation, and fluid-rock interaction is still contentious. In particular, the role of pre-existing structures at depth (ductile shear zones) and their consequent exploitation as potential pathways for melt and/or fluids during large-scale faulting is not fully constrained.

In this contribution, we present the results of a petrostructural study conducted on shear zones that occur in the lower gabbroic section (≥ 600 m below sea-floor – mbsf) of hole U1473A, the target of IODP Expedition 360. Through a combination of quantitative microstructural analysis, crystallographic fabric studies, mineral chemistry, and thermodynamic modelling, we aim to characterise the dominant deformation mechanisms active during shear zone deformation and to assess their influence on the mechanical behaviour of the lower oceanic crust. Our results have implications for the overall processes of strain localisation during exhumation of the Atlantis Bank oceanic core complex at the ultraslow-spreading Southwest Indian Ocean Ridge.

2. Geological setting and the site U1473A

The Atlantis Bank oceanic core complex located along the Southwest Indian Ridge (Fig. 1a) is a N–S trending, ~ 40 km long by ~ 30 km wide dome-shaped platform located close to the Atlantis II Transform (Fig. 1a–b; Dick et al., 1991; Matsumoto et al., 2002; Stakes et al., 1991). This shallow platform (~ 700 m below sea level – mbsl) represents the foot-wall of a detachment fault and is located ~ 100 km away from the present-day ultraslow-spreading (~ 14 mm/year) Southwest Indian Ridge trace (Fig. 1a; Dick et al., 1991).

Flexural uplift and extension on the moderate-high angle normal faults surrounding the Atlantis Bank led to anomalous uplift and asymmetric detachment faulting exposing gabbros and peridotites from the lower crust-upper mantle boundary deformed at high temperatures (Fig. 1c), suggesting that deformation was contemporaneous with gabbro emplacement and solidification (Dick et al., 2019b; Miranda and John, 2010).

IODP hole U1473A is located at 32.42°S, 57.69°E, 710 m below sea-level and was drilled on the top of Atlantis Bank during Expedition 360, in 2016 (Fig. 1b–c). It lies 1–2 km north/northeast of two previously drilled holes: i) 1.508 km deep hole 735B, drilled during two legs in 1987 (Shipboard Scientific Party, 1989) and 1997 (Shipboard Scientific Party, 1999a, 1999b) and ii) 158 m deep hole 1105A, drilled in 1998 (Pettigrew et al., 1999). Hole U1473A drilled 789.7 m of rocks, recovering ~ 469.4 m of core (average recovery of 59%; Dick et al. (2019a)) mainly composed of olivine gabbro (76.5%), gabbro (14.6%) and oxide-rich gabbro (7.4%; oxide content $>2\%$), cut by several slightly deformed to non-deformed felsic veins, microgabbro and minor diabase (Fig. 1c–d; see Dick et al., 2019a for a complete description of the lithologies recovered at hole U1473A). Grain size and modal mineral variation define the igneous layering which is frequently obliterated by crystal-plastic deformation. The gabbroic rocks bearing Fe–Ti oxides are usually associated with shear zones, and the presence of oxides is attributed to the percolation of late-stage melt through an olivine gabbro framework (Dick et al., 2016).

3. Methods

3.1. Sample acquisition and quantitative microstructural analysis

The shear zones analysed in this study derive from the lower section of hole U1473, mainly marked by olivine-gabbro deformed under high-temperature, granulite facies conditions (Dick et al., 2019a). Although crystal-plastic deformation occurs in intervals along the entire length of the hole (Fig. 1e), the upper 450 mbsf are characterized by significant greenschist-facies alteration and the development of low-temperature veins and fractures that obliterate the early ductile deformation (Dick

et al., 2019a). Therefore, we collected samples from below 500 mbsf in order to target the high-temperature deformation mechanisms that are recorded in the rocks prior to lower-grade, brittle-ductile reworking.

Cores of deformed gabbro were drilled and cut into two identical half pieces. Structures were studied on the split face of the working half of the core. Orientation of the core faces were obtained by cutting directly perpendicular to the strike of the sample. If a perpendicular strike cut was not possible, two apparent dips and dip azimuth measurements were necessary to acquire a true dip value. Information about the dip azimuth was not always possible to acquire because the rock core might be subjected to rotation during drilling. A complete outline of sample acquisition methodology is given in MacLeod et al. (2017). For preparation of thin sections, samples were cut normal to foliation and, whenever possible, parallel to the XZ plane of the finite strain ellipsoid. The stretching lineation was identified by the elongation of amphibole grains on the foliation plane. We analysed four samples of gabbroic shear zones (Fig. 1d), collected at depths of 527.4 mbsf (Sample 58R), 631.1 mbsf (Sample 69R), 687.3 mbsf (Sample 78R) and 723.3 mbsf (Sample 81R). Mineral abbreviations used to describe the samples are after Whitney and Evans (2010).

Deformation microstructures were analysed by both optical and scanning electron microscopy (SEM). Grain boundaries were manually traced based on secondary electron and backscatter electron images. The grains were contoured as polygons with the area of each polygon being as close as possible to the grain. Grain sizes were later calculated using *ImageJ* software as the diameter of the circle with the area equivalent to that of the grain.

3.2. EBSD analysis

The samples used for the EBSD analysis were polished in a Buehler Minimet® 1000 grinder-polisher for 40 min in 1-mm diamond suspension solutions and finalised with colloidal silica solution.

We used EBSD-derived analyses to identify mineral phases, describe microstructures, and measure the crystallographic orientation to generate misorientation information within and between grains. Crystallographic preferred orientation (CPO) information was acquired for plagioclase, clinopyroxene, orthopyroxene, and amphibole.

Crystallographic patterns were obtained using an EDAX–TSL system in a JEOL JSM 7100F Field Emission Scanning Electron Microscope (FE SEM) at the Scientific Centre for Optical and Electron Microscopy (ScopeM), ETH Zurich, Switzerland, and in an FEI QUANTA 450 Scanning Electron Microscope (SEM) at the Geochronology Laboratory at University of Brasilia, Brazil. Analytical conditions were set at 20 kV accelerating voltage, 25–23 mm working distance, 7 nA beam current, 70° sample tilt, and step sizes of 3–10 μm for data capture.

The raw EBSD output data was processed using the MATLAB toolbox MTEX 5.1.1 (available at <https://mtextoolbox.github.io>, last access: February 2021; Bachmann et al., 2010). Grains were detected using an angle of 10° or higher, whereas subgrain boundaries were classified as having 2–10° of misorientation between neighbouring grains. Data were noise-reduced by removing grains containing less than 10 pixels, as these grains may be error-prone. The orientation distribution function used to contour the pole figures and calculate the fabric strength were derived based on the de la Vallée Poussin kernel with optimal halfwidth for the population of grains (one point per grain) to avoid over-estimation of texture for small orientation data (i.e., grains; Bachmann et al., 2011). For contouring of inverse pole figures, we used a kernel halfwidth of 13°.

The data is presented as pole figures, grain- and phase-boundary maps, intragranular misorientation maps, misorientation histograms, and inverse pole figures for subgrains. The data in pole figures are displayed in the kinematic reference frame in lower hemisphere, equal area projections, measured in multiples of uniform distribution. The difference in lattice distortion between two grains is described by a rotation angle (misorientation angle) about a rotation axis (misorientation axis).

We display misorientation angles for correlated (neighbour grains), uncorrelated (random grains), and uniform (theoretical) distributions in histograms in which the relative frequency of occurrence is plotted against the angle of misorientation as measured in degrees. In the histograms, misorientation angles are binned into 5° increments, and the minimum misorientation angle is 2° to reduce errors at very low angles. The inverse pole figures (misorientation axes) are displayed relative to the crystal reference frame. In the intragranular misorientation maps ('mis2mean' function in MTEX toolbox), the misorientation was calculated by deviation of the reference orientation at a given position in the grain and the mean orientation of the grain (Hielscher and Schaeben, 2008).

The texture strength is defined by both the J- and M-index. J-index (Bunge, 1982) ranges from 1 (random fabric) to infinite (single crystal). M-index (Skemer et al., 2005) spans from 0 (random fabric) to 1 (single crystal fabric). We refer to (hkl) to indicate a specific crystallographic plane and $[uvw]$ to indicate a specific crystallographic direction.

3.3. Mineral chemistry and P–T estimates

Pyroxene, plagioclase, and amphibole chemical compositions were measured using a wavelength-dispersive (WDS) JEOL JXA–8900 electron microprobe at the Microprobe Laboratory at University of Brasilia, Brazil. Representative chemical analyses are listed in Table 1. The analyses were acquired with an accelerating voltage of 15 kV and a beam

current of 10 nA from a beam diameter of 1 µm.

Equilibrium temperatures were calculated using the edenite–richterite geothermometer (Holland and Blundy, 1994), applied on adjacent grains of amphibole and recrystallised plagioclase (Table 2).

3.4. EDS chemical element map analysis

Maps of modal composition and mineral chemistry were acquired via energy dispersive spectroscopy (EDS) at specific areas of ~0.5 mm² containing the representative, deformed mineral assemblage of the mafic shear zones. The analyses were made using a scanning electron microscope (SEM) equipped with an EDAX Ametek Apollo X EDS detector operating with an accelerating voltage of 15–20 kV and a beam current of 90 µA, at the Geochronology Laboratory at University of Brasilia, Brazil.

3.5. Thermodynamic modelling

P–T pseudosection modelling was carried out with the software Perple_X 6.7.5 (Connolly, 2005) using an internally consistent thermodynamic dataset (Holland and Powell, 2011). The pseudosection was calculated in the nine components system: SiO₂–TiO₂–Al₂O₃–FeO–MgO–CaO–Na₂O–O₂–H₂O (NCFMASHTO). The modelled bulk composition was estimated using the mineral chemistry and modal proportion of the bulk representative mineral assemblage

Table 1

Representative microprobe analyses of the main minerals in gabbroic shear zones from hole U1473A.

	Plagioclase		Clinopyroxene				Orthopyroxene			Amphibole	
	Clasts	Rex	Clasts	Rex		Clasts	Rex		Pyr-der	Rex	
				Core	Rim		Core	Rim			
SiO ₂	52.57	54.19	52.70	49.83	51.37	52.41	50.33	51.11	42.11	42.28	
TiO ₂	0.13	0.22	0.38	0.27	0.17	0.69	0.03	0.17	3.05	3.38	
Al ₂ O ₃	29.13	27.82	1.85	1.53	1.16	0.93	0.58	0.48	11.99	11.80	
Cr ₂ O ₃	0.00	0.00	0.18	0.02	0.00	0.05	0.00	0.00	0.29	0.13	
FeO	0.21	0.20	7.30	9.91	9.46	22.47	23.64	23.62	11.03	11.17	
F	0.00	0.00	0.00	0.00	0.00	0.00	0.00	0.00	0.07	0.08	
Cl	0.00	0.00	0.00	0.00	0.00	0.00	0.00	0.00	0.01	0.01	
MnO	0.02	0.02	0.18	0.23	0.25	0.45	0.55	0.68	0.14	0.08	
MgO	0.05	0.00	14.82	14.41	14.36	21.32	21.70	21.82	13.22	13.27	
CaO	12.58	11.14	21.96	20.96	21.91	1.56	0.87	1.06	11.62	11.72	
Na ₂ O	4.41	5.37	0.40	0.51	0.39	0.02	0.00	0.05	2.68	2.59	
K ₂ O	0.08	0.09	0.00	0.00	0.01	0.01	0.00	0.00	0.56	0.50	
Total	99.17	99.07	99.77	97.66	99.09	97.91	97.70	98.98	96.77	97.00	
O	8.00	8.00	6	6	6	6	6	6	23	23	
Si	2.40	2.47	1.95	1.92	1.95	1.96	1.95	1.95	6.23	6.24	
Ti	0.00	0.01	0.01	0.01	0.00	0.02	0.00	0.00	0.34	0.38	
Al	1.57	1.49	0.08	0.07	0.05	0.04	0.03	0.02	2.09	2.05	
Cr	0.00	0.00	0.01	0.00	0.00	0.00	0.00	0.00	0.03	0.01	
Fe	0.00	0.00	0.23	0.32	0.30	0.70	0.76	0.75	1.37	1.38	
Mn	0.00	0.00	0.01	0.01	0.01	0.01	0.02	0.02	0.02	0.01	
Mg	0.00	0.00	0.82	0.83	0.81	1.19	1.25	1.24	2.92	2.92	
Ca	0.62	0.54	0.87	0.87	0.89	0.06	0.04	0.04	1.84	1.85	
Na	0.39	0.47	0.03	0.04	0.03	0.00	0.00	0.00	0.77	0.74	
K	0.00	0.01	0.00	0.00	0.00	0.00	0.00	0.00	0.11	0.09	
Total	4.99	4.99	4	4	4	4	4	4	15.72	15.69	
X _{An} ^a	60.89	53.13									
X _{Or} ^b	0.46	0.51									
X _{Mg} ^c			0.78	0.72	0.73	0.63	0.62	0.62	0.71	0.70	
X _{Ca} ^d			0.45	0.43	0.44	0.03	0.02	0.02			
X _{ivAl}									0.33	0.30	

Clasts = Porphyroclasts Rex = Recrystallised Pyr-der = Pyroxene-derived.

$$^a X_{An} = Ca/(Ca + Na + K).$$

$$^b X_{Or} = K/(Ca + Na + K).$$

$$^c X_{Mg} = Mg/(Mg + Fe^{2+}).$$

$$^d X_{Ca} = Ca/(Ca + Mg + Fe^{2+}).$$

Table 2
Chemistry of amphibole and plagioclase pairs used to estimate equilibrium temperatures.

Pair Amp - Plag	Pyroxene-derived aggregates					Avg	Std Dev	Recrystallised matrix					Avg	Std Dev
	3	4	17	22	23			7	14	15	20	21		
Amphibole														
SiO ₂	41.58	41.51	42.43	42.03	41.99	41.99	0.37	41.92	42.28	41.99	41.82	41.78	41.96	0.20
TiO ₂	3.54	3.86	3.19	3.48	3.59	3.53	0.24	3.82	3.38	3.79	3.64	4.07	3.74	0.26
Al ₂ O ₃	11.83	12.44	11.84	12.30	11.45	11.97	0.40	11.95	11.80	11.81	11.70	12.27	11.91	0.22
FeO	11.26	10.71	11.55	10.45	11.33	11.06	0.46	11.23	11.17	10.92	11.10	10.86	11.06	0.16
MgO	13.31	13.04	13.55	12.89	13.26	13.21	0.25	13.22	13.27	13.02	12.94	13.30	13.15	0.16
MnO	0.07	0.13	0.07	0.13	0.17	0.12	0.04	0.15	0.08	0.16	0.12	0.05	0.11	0.04
CaO	11.46	11.35	11.41	11.38	12.27	11.57	0.39	11.60	11.72	11.31	11.44	11.61	11.53	0.16
Na ₂ O	2.77	2.84	2.64	2.56	2.18	2.60	0.26	2.69	2.59	2.74	2.63	2.64	2.66	0.06
K ₂ O	0.45	0.50	0.54	0.61	0.64	0.55	0.08	0.54	0.50	0.49	0.52	0.52	0.51	0.02
Total	96.27	96.37	97.22	95.84	96.88	96.52	0.54	97.12	96.79	96.22	95.91	97.09	96.62	0.54
X _{Mg}	0.72	0.70	0.74	0.70	0.69	0.71	0.02	0.70	0.70	0.70	0.70	0.71	0.70	0.01
Plagioclase														
SiO ₂	53.75	54.59	54.43	54.65	54.30	54.34	0.36	54.15	54.77	54.94	54.46	54.74	54.61	0.31
TiO ₂	0.02	0.06	0.00	0.06	0.11	0.05	0.04	0.05	0.05	0.14	0.00	0.00	0.05	0.06
Al ₂ O ₃	28.52	28.91	27.29	28.09	27.89	28.14	0.62	27.99	27.99	28.97	27.79	28.61	28.27	0.50
FeO	0.21	0.25	0.38	0.20	0.20	0.25	0.07	0.19	0.20	0.33	0.18	0.25	0.23	0.06
CaO	10.89	11.53	10.48	10.49	10.42	10.76	0.47	10.58	10.69	10.75	10.35	10.55	10.58	0.15
Na ₂ O	5.23	5.30	5.79	5.62	5.66	5.52	0.24	5.46	5.72	5.47	5.65	5.61	5.58	0.12
K ₂ O	0.09	0.06	0.09	0.08	0.06	0.08	0.02	0.08	0.11	0.10	0.10	0.08	0.09	0.02
Total	98.72	100.71	98.45	99.19	98.63	99.14	0.92	98.50	99.54	100.70	98.52	99.85	99.42	0.93
X _{An}	53.21	54.40	49.77	50.52	50.25	51.63	2.05	51.49	50.47	51.77	50.04	50.72	50.90	0.72
T (°C)	900.93	896.54	876.75	846.41	835.59	871.25	29.32	891.00	862.79	884.45	871.49	886.11	879.17	11.65

from sample 69R, as measured in thin sections. The H₂O content of the system was defined so that the mineral assemblage was saturated immediately below the solidus (White et al., 2008). The amount of Fe³⁺ of the modelled bulk composition was calculated using a T-X (O₂) pseudosection and the proportion of magnetite measured from thin sections using back scattered electron images (Fig. S1), and is available in the supplementary material (Tables S1–S7). Solution models used for melt, amphibole, and clinopyroxene are from Green et al. (2016), orthopyroxene and garnet from White et al. (2014), plagioclase from Holland and Powell (2003), olivine from Holland and Powell (1998), spinel (including magnetite) from White et al. (2002), and ilmenite from White et al. (2000).

Mineral chemistry was obtained via WDS analyses, and the modal proportion of each mineral phase was estimated based on EDS maps acquired in a SEM. Isoleths of modal proportion of olivine and melt, and contents of X_{An} (Ca/Ca + Na + K) in plagioclase were traced to constrain the *P*–*T* conditions of deformation.

4. Results

4.1. Mesoscale gabbroic shear zones

The sheared gabbros cover ~72% of the hole U1473A and record a heterogeneous deformation primarily dominated by crystal-plastic-related fabrics (Fig. 1d–e; Dick et al., 2016). The rocks were partially overprinted by millimetre to centimetre-thick carbonate and clay-rich cataclastic zones (<400 °C) that extend up to ~300 mbsf. Dissolution-precipitation processes and amphibole veining formed at 500–700 °C are concentrated in the upper (400 m) sections of the hole (Dick et al., 2016). Whenever possible, apparent shear sense has been determined primarily by asymmetries in porphyroclast tails and foliation morphology, and crosscutting relationships between mylonitic fabrics (MacLeod et al., 2017). These observations indicate that the apparent shear sense is normal in the upper part of the hole and mostly reverse in the lower part.

The high-temperature shear zones from the lower part of hole U1473A developed at depths below ~520 mbsf and comprise elongated plagioclase, pyroxene, brown amphibole, and olivine grains with varied amounts of ilmenite and magnetite. The shear zones are characterized by 1- to 10-cm-thick discrete mylonitic bands that are commonly

alternated with relatively undeformed rocks, defining an anastomosed framework (Fig. 1), similar to the ductile shear zone pattern reported in Carreras et al. (2010). Locally, thin ultramylonite bands (maximum width of 1 cm) with fine grain size and segregated compositional layering crosscut the previous mylonitic foliation. Dips of the mylonitic fabric range between 10° to 40°, with local subvertical inclinations.

4.2. Microstructure

Representative microstructural features of the mylonitic shear zones are shown in Figs. 2–7. The gabbroic shear zones (Fig. 1e; 2) consist of plagioclase (60%), clinopyroxene (26%), amphibole (6%), orthopyroxene (5%), ilmenite (0.5–1%), magnetite (0.5–1%), and olivine (0.5–1%). Minor trace amounts of apatite occur as inclusions in plagioclase and pyroxene grains.

Large (up to 5 mm in size), relict porphyroclasts of clinopyroxene, orthopyroxene, plagioclase, and olivine are embedded in a fine-grained (<30 μm), polyphase matrix composed of plagioclase, clinopyroxene, orthopyroxene, amphibole, ilmenite, magnetite, and olivine. Plagioclase-rich layers (Fig. 2a; 3a, b) are in abrupt contact with the fine-grained mixture (Figs. 2a and 3c, d) and define the mylonitic foliation that pervasively occur within the shear zone domains (Fig. 2a).

4.2.1. Porphyroclasts

The relict porphyroclasts comprise grains of clinopyroxene, orthopyroxene, olivine, and plagioclase (Fig. 2a; b; d; f, g). Most pyroxene grains are flattened and have a shape-preferred orientation (SPO; aspect ratio: ~4) parallel to the foliation with sizes ranging from 300 μm up to 5 mm (Fig. 2a).

Some clinopyroxene porphyroclasts show orthopyroxene exsolution lamellae and kink bands perpendicular to the foliation plane, formed by local bending of the cleavage planes (Fig. 2b; c; 4a). These kink bands are swept by recrystallised grains of clinopyroxene ranging in size from 50 to 80 μm (Fig. 2b). Amphibole occurs filling the interstices of the recrystallised clinopyroxene grains (Fig. 2c).

The clinopyroxene and orthopyroxene porphyroclasts are mantled by recrystallised grains (<90 μm) defining a core and mantle structure, locally forming recrystallised tails (Fig. 4a). The recrystallised grains surrounding the clasts display local evidence for internal deformation, such as undulose extinction, and few grains develop subgrain

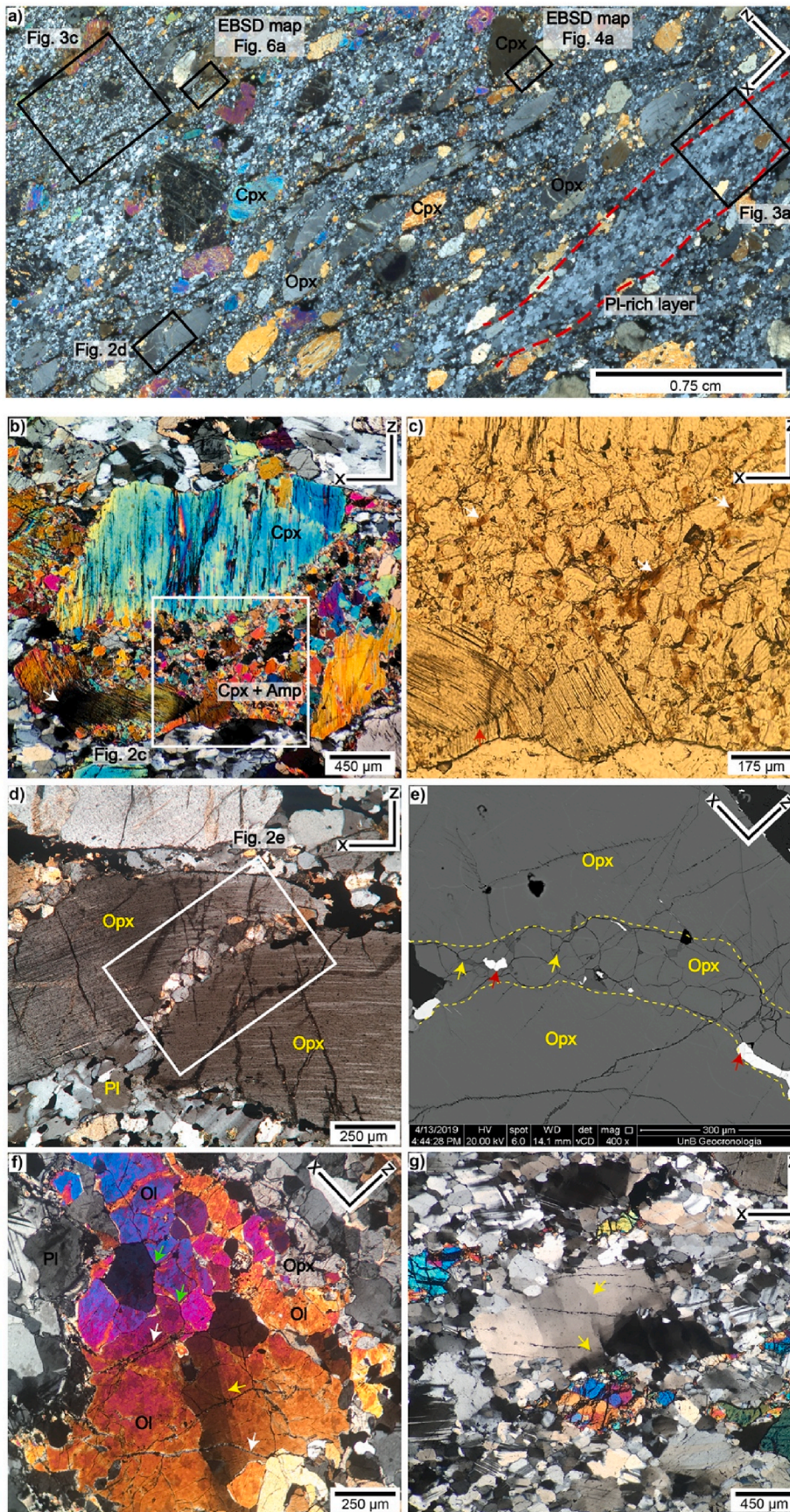


Fig. 2. Representative deformation microstructures of the gabbroic shear zones from hole U1473A in cross-polarized light (a, b, d, f, g), plane-polarized light (c) and backscatter electron (BSE) image (e). The black boxes in (a) indicate the corresponding microphotographs in Figs. 2 and 3, and the areas where EBSD analyses were performed. (a) Scanned thin section (sample 78R) shows the mylonitic foliation defined by alternating bands of plagioclase-rich layers and the polyphase matrix. Fe–Ti oxide bands (ilmenite and magnetite) and elongated clinopyroxene and orthopyroxene grains are oriented parallel to the mylonitic fabric. (b) Bent cleavage planes (white arrow) and exsolution kink bands at which recrystallised grains are common (69R). (c) Close-up photo from (b) showing a kink band (red arrow) and brown amphibole (white arrows) filling the interstices of recrystallised clinopyroxene grains. (d) Healed microfracture crosscutting an orthopyroxene porphyroclast (78R). (e) Close-up image from (d). The microfracture is filled with a mixture of fine-grained orthopyroxene, amphibole, and magnetite. Note the presence of interstitial and cusp-like feature of amphibole (yellow arrows) and magnetite (red arrows). (f) High birefringence mantled olivine porphyroclast showing subgrain boundaries (yellow arrow) and recrystallised grains with curved to straight boundaries (green arrows). Fractures that crosscut the clast (perpendicular to the subgrain boundaries; white arrows) are filled with plagioclase, amphibole, and ilmenite (58R). (g) Plagioclase porphyroclast showing undulose extinction, subgrain boundaries oriented in both normal and parallel directions in relation to the mean grain orientation (yellow arrows), and mantling neoblasts (81R). Pl: Plagioclase, Cpx: Clinopyroxene, Opx: Orthopyroxene, Ol: Olivine, Amp: Amphibole, Ilm: Ilmenite, Mag: Magnetite. (For interpretation of the references to colour in this figure legend, the reader is referred to the Web version of this article.)

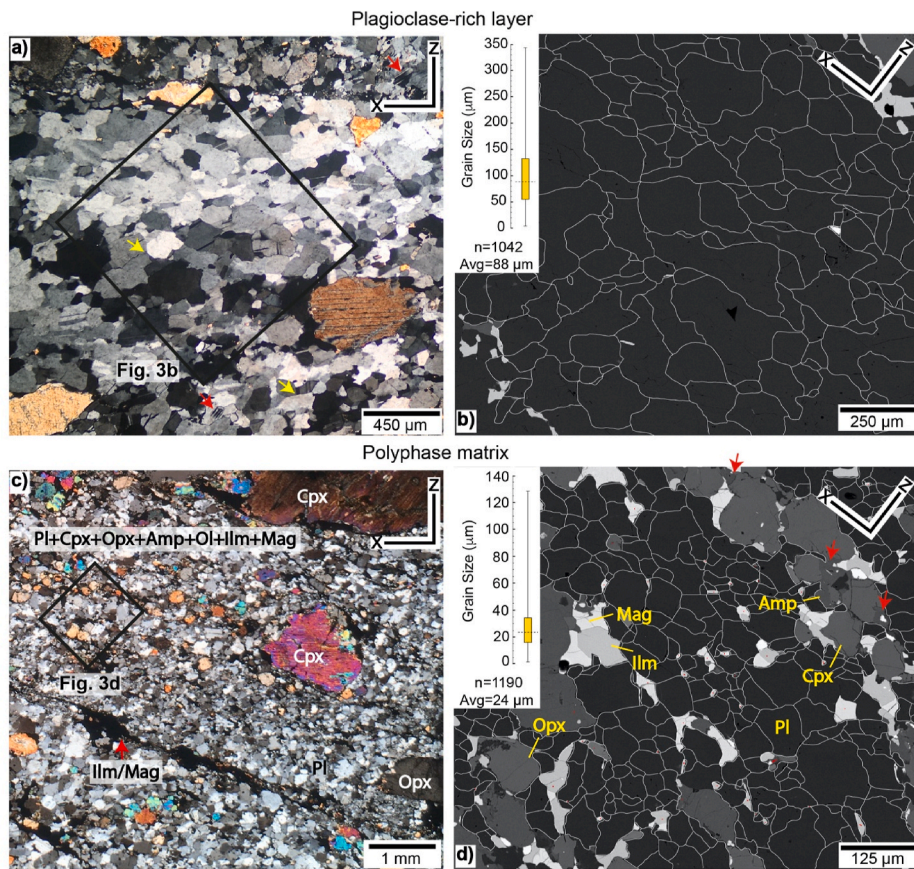


Fig. 3. Deformation microstructures and plagioclase grain-size analysis of the plagioclase-rich (a) and (b), and the polyphase matrix (c) and (d) of the gabbroic shear zones from Site U1473A (sample 78R). The number of analysed grains (n) and the average grain size is shown for each microstructural domain. The dashed black line in the yellow box in (b) and (d) represent the average grain size, respectively. (a) Optical microphotograph showing recrystallised plagioclase grains with deformation twins (red arrows), undulose extinction and triple junctions (yellow arrows). (b) Close-up BSE image from (a) showing the grain contours of a plagioclase-rich layer. Average grain size is 88 μm . (c) Optical microphotograph of the fine-grained, polyphase mixture mainly composed of plagioclase (Pl), clinopyroxene (Cpx), orthopyroxene (Opx), amphibole (Amp), ilmenite (Ilm), and magnetite (Mag). (d) Close-up BSE image from (c) showing phase distribution in the polyphase matrix, and average grain size (24 μm) of plagioclase grains. Red arrows are amphibole grains at pressure shadows of pyroxene grains. (For interpretation of the references to colour in this figure legend, the reader is referred to the Web version of this article.)

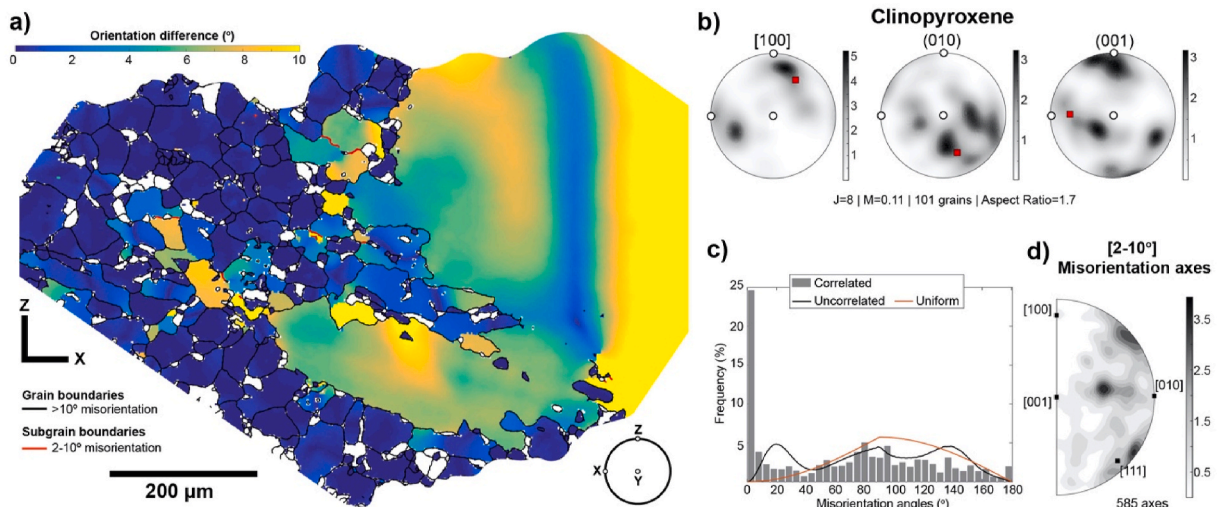


Fig. 4. EBSD analysis of a clinopyroxene porphyroblast and recrystallised grains (core and mantle microstructure) from inset box in Fig. 2a. The number of grains used to construct the pole figures, J- and M-index (J and M), and the aspect ratio are designated below the pole figures. All plots are lower hemisphere projections and represent one point per grain as multiples of uniform distribution (m.u.d). The corresponding gray scale legend for m.u.d is indicated at the right side of each pole figure. The orientation of the pole figures in respect to the strain axes X, Y, and Z is shown in the schematic pole figure at bottom right in (a). (a) Intragranular misorientation map showing the internal misorientation patterns in the porphyroblast and recrystallised grains. (b) Pole figures showing the crystallographic orientation of the clinopyroxene porphyroblast (red squares in the diagram) and recrystallised grains. (c) Misorientation angles between correlated (gray bars) and uncorrelated (black line) distributions for the recrystallised grains surrounding the porphyroblast. (d) Inverse pole figures illustrating the misorientation axes between 2 and 10° shown in the crystal reference frame for the mantling recrystallised grains. (For interpretation of the references to colour in this figure legend, the reader is referred to the Web version of this article.)

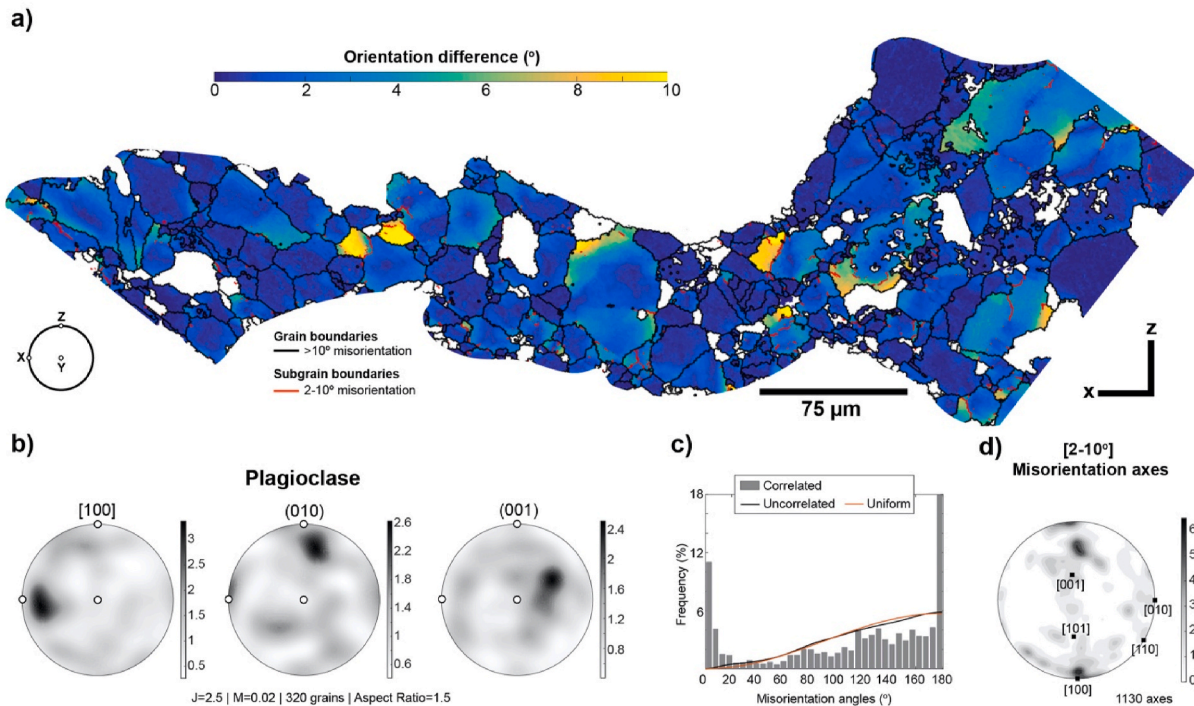


Fig. 5. EBSD analysis of plagioclase-rich layer (sample 69R). The number of grains used to construct the pole figures, J - and M -index (J and M), and the aspect ratio are designated below the pole figures. All plots are lower hemisphere projections and represent one point per grain as multiples of uniform distribution (m.u.d). The corresponding gray scale legend for m.u.d is indicated at the right side of each pole figure. The orientation of the pole figures in respect to the strain axes X , Y and Z is shown in the schematic pole figure at bottom left corner in (a). (a) Intragranular misorientation map. Large grains show an accumulation of dislocations at grain boundaries. (b) Pole figures showing the crystallographic orientation of recrystallised plagioclase grains. (c) Distribution of misorientation angles between correlated (gray bars) and uncorrelated (blue line) grains. (d) Inverse pole figures illustrating the misorientation axes between 2 and 10° shown in the crystal reference frame. See text for discussion. (For interpretation of the references to colour in this figure legend, the reader is referred to the Web version of this article.)

boundaries commonly concentrated close to the grain edges (Fig. 4a).

Orthopyroxene porphyroclasts have healed microfractures (up to 100 μm thick; Fig. 2d) that crosscut the clasts and are filled with fine-grained (~30 μm) orthopyroxene, amphibole, and magnetite (Fig. 2e) that lack internal deformation microstructures. Within the microfractures, orthopyroxene grains have a polygonal shape with straight and curved grain boundaries (Fig. 2e). Amphibole and magnetite occur along grain boundaries of orthopyroxene. They commonly form irregular, interstitial shapes with cusp-like terminations at orthopyroxene grains. Fine grains of strain-free brown amphibole (<20 μm in size) also occur within cleavage planes of clinopyroxene and orthopyroxene clasts and at the rims of these porphyroclasts.

Olivine clasts occur locally and have grain sizes up to 2 mm with fractures filled by fine-grained plagioclase, amphibole, and ilmenite (~20–40 μm; Fig. 2f). Undulose extinction and prismatic subgrains are common (Fig. 2f). Recrystallised grains of olivine (~50–70 μm) occur at the margins of the olivine porphyroclasts. These new grains display local undulose extinction and subgrains, and have straight boundaries with triple junctions (Fig. 2f).

Plagioclase porphyroclasts have sizes up to 1 mm (Fig. 2g) with sweeping undulose extinction, subgrains oriented in both perpendicular and parallel directions in relation to the mean grain elongation, and mechanical twins that are preferentially oriented parallel to the foliation (Fig. 2g). The edges of the porphyroclasts are often mantled with equant, recrystallised plagioclase grains slightly smaller than the subgrains in the large clasts (<80 μm; Fig. 2g). The new grains show undulose extinction and subgrains, mechanical twins and have straight and curved grain boundaries with common triple junctions (Fig. 2g).

4.2.2. Plagioclase-rich layers

The plagioclase-rich bands are ~2 millimetre-thick, discontinuous and in abrupt contact with the polyphase matrix (Fig. 2a). Average grain

size within these bands is ~88 μm (Fig. 3a and b), which is similar to the subgrains and recrystallised grains around porphyroclasts. Undulose extinction and subgrain boundaries are ubiquitous in the larger grains (>70 μm; Fig. 5a) within the layers. Mechanical twin lamellae occur in some grains regardless of grain size (Fig. 3a; 5a). The grain boundaries are mostly straight and curved with common triple junctions (Fig. 3a and b; 5a). Plagioclase grains show a weak shape preferred orientation (aspect ratio: 1.5) with their long axes parallel to the main planar fabric of the shear zone (Fig. 2a and b; 5a).

4.2.3. Polyphase matrix

The recrystallised matrix contains a mixture of fine-grained (~25 μm), heterogeneously distributed grains of plagioclase, clinopyroxene, orthopyroxene, brown amphibole, and minor ilmenite, magnetite, and olivine. All grains have a shape-preferred orientation parallel to the foliation (Fig. 3c and d; 6a) with average aspect ratio of ~1.5.

Plagioclase is mostly recrystallised into fine-grained and typically strain-free aggregates with straight and curved grain boundaries (Figs. 3d and 6a), but is also preserved as small grains (<60 μm), locally showing some twins (Fig. 6a).

Clinopyroxene and orthopyroxene are the coarsest phases in the polyphase matrix (~39 μm) and occur both as bands intermixed with grains of amphibole and plagioclase, and as isolated aggregates in the fine-grained mixture. The boundaries between clinopyroxene and orthopyroxene grains are mostly straight and wavy, while interphase boundaries are essentially curved (Figs. 3d and 6a). The majority of clinopyroxene and orthopyroxene grains lack systematic internal deformation microstructures but a few grains display local undulose extinction.

Fine grains of amphibole (<20 μm) are strain-free and occur as interstitial phases at triple junctions, along pressure shadows of pyroxene grains (Fig. 3d), and as fine-grained bands intermixed with ilmenite

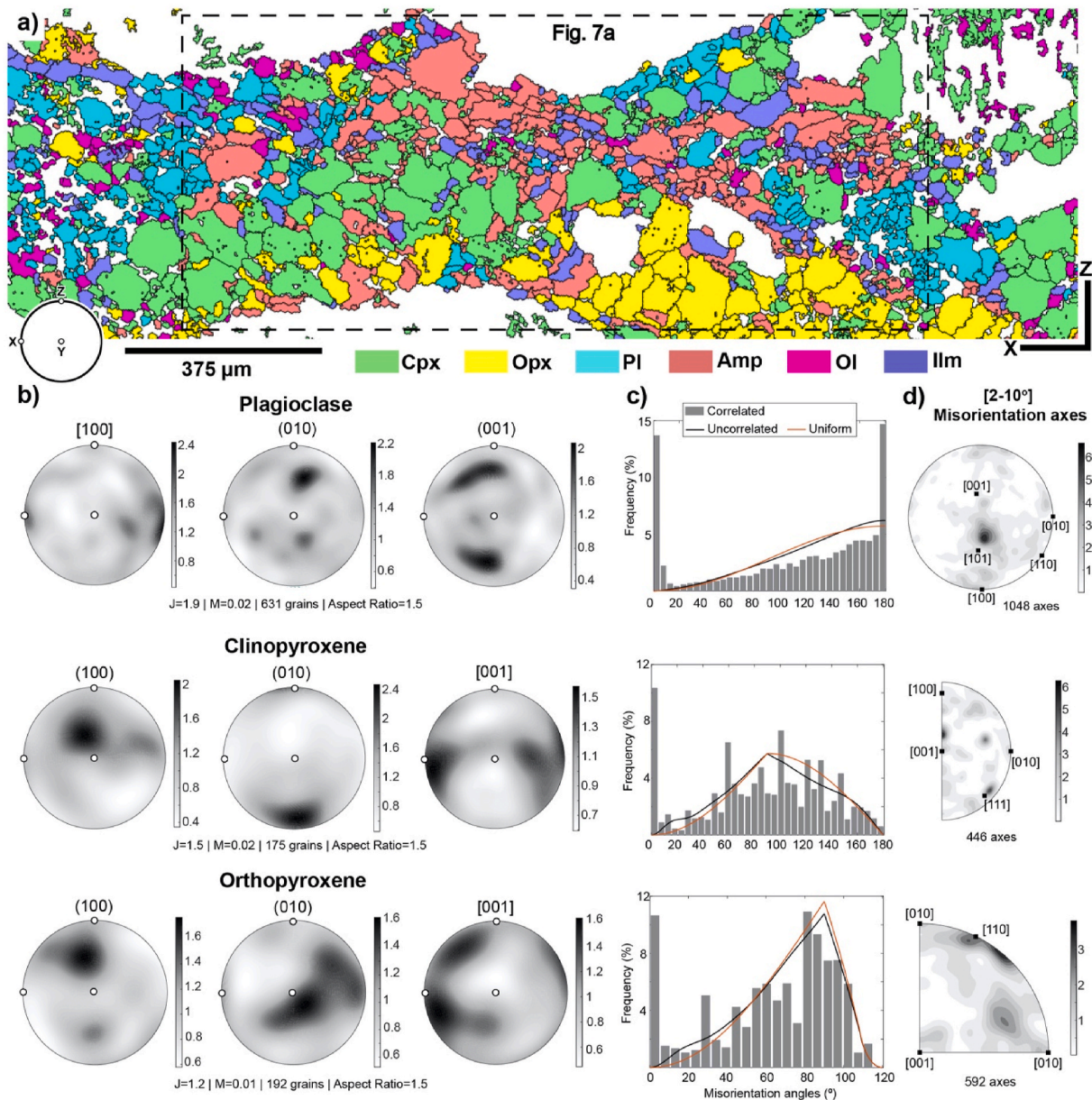


Fig. 6. EBSD analysis of the polyphase matrix from the selected area in Fig. 2a. The number of grains used to construct the pole figures, J - and M -index (J and M) and the aspect ratio are designated below the pole figures. All plots are lower hemisphere projections and represent one point per grain as multiples of uniform distribution (m.u.d). The corresponding gray scale legend for m.u.d is indicated at the right side of each pole figure. The orientation of the pole figures in respect to the strain axes X , Y and Z is shown in the schematic pole figure at bottom left in (a). (a) Phase distribution map comprising clinopyroxene (Cpx), orthopyroxene (Opx), plagioclase (Pl), amphibole (Amp), and ilmenite (Ilm) grains. (b) Pole figures showing the crystallographic orientation of the fine-grained matrix. (c) Distribution of misorientation angles. (d) Inverse pole figures showing the misorientation axes between 2 and 10° in respect to the crystal reference frame. See text for discussion.

(Figs. 6a and 7a).

Ilmenite and magnetite occur associated with pyroxene grains or partially wrapping around plagioclase grains (Figs. 3d and 6a). Some elongated trails of ilmenite and magnetite also occur interstitially, parallel to the foliation, showing irregular shapes and cusp-like terminations at grain boundaries (Fig. 3d). Olivine grains ($\leq 25 \mu\text{m}$), when present, are strain-free and are heterogeneously distributed within the matrix, mostly associated with ilmenite, magnetite, plagioclase, clinopyroxene, and amphibole (Fig. 6a).

4.3. EBSD analysis

4.3.1. Porphyroclasts rimmed by recrystallised grains (core-mantle structure)

Clinopyroxene porphyroclasts (Fig. 4a and b) surrounded by a mantle of recrystallised grains are preferentially oriented with the $[100]$ axes and poles to (010) planes at oblique angles from Z , in intermediate positions between Y and Z . Poles to (001) align close to X .

Texture strength of the recrystallised grains is moderate, with J - and M -index of 8 and 0.11 , respectively. $[100]$ axes of the recrystallised grains that rim the clast form two main maxima close to Z and X (Fig. 4b). Poles to (010) planes have maxima between X and Y , and Y and Z . Poles to (001) planes have maxima clustered around Z , and around intermediate positions slightly offset from X and Y (Fig. 4b). The

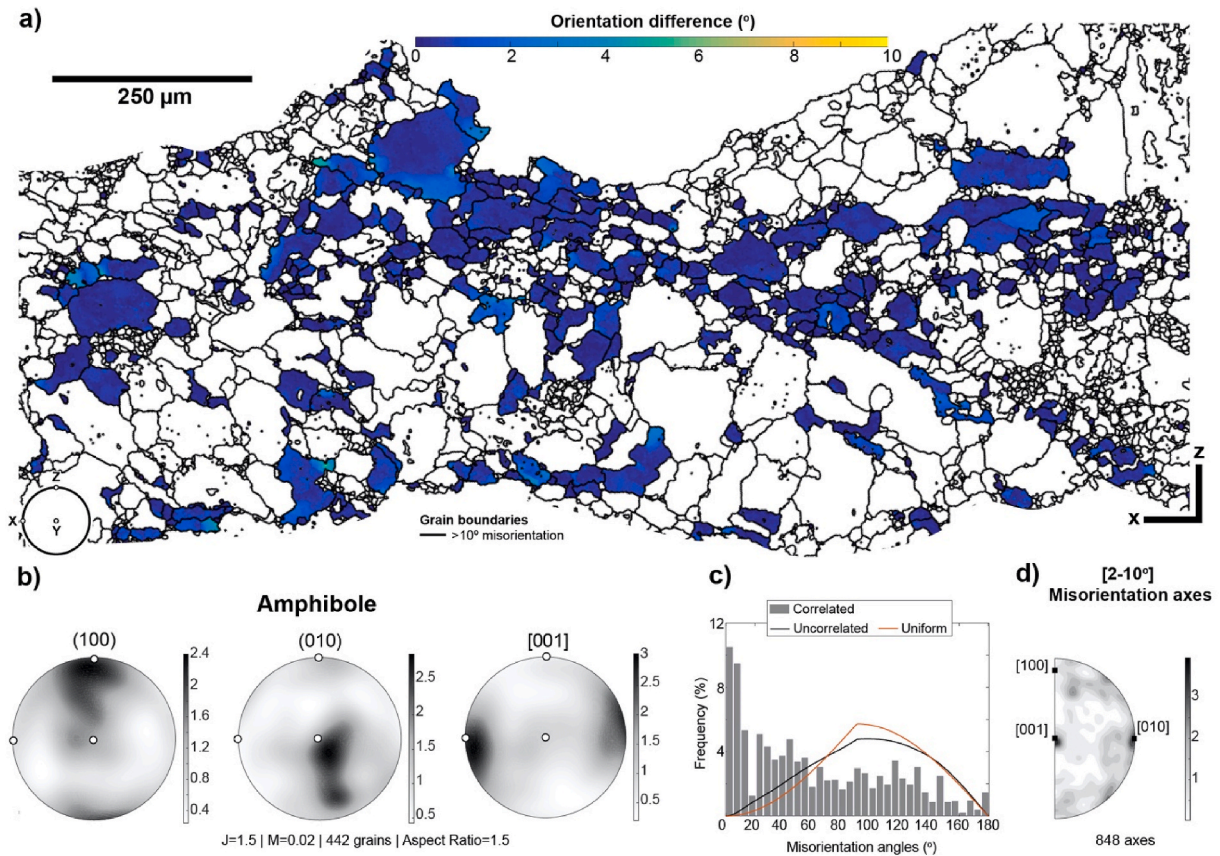


Fig. 7. EBSD subset analysis for amphibole from the inset area highlighted in Fig. 6a. The number of grains used to construct the pole figures, J - and M -index (J and M), and the aspect ratio are designated below the pole figures. All plots are lower hemisphere projections and represent one point per grain as multiples of uniform distribution (m.u.d). The corresponding gray scale legend for m.u.d is indicated at the right side of each pole figure. The orientation of the pole figures in respect to the strain axes X , Z , and Y is shown in the schematic pole figure at bottom left. (a) Intragranular misorientation map showing that amphibole grains are virtually free of dislocations. (b) Pole figures showing the crystallographic orientation of amphibole grains. (c) Distribution of misorientation angles. (d) Inverse pole figures of the misorientation axes between 2 and 10° in respect to the crystal reference frame. See text for discussion.

misorientation angle distribution for recrystallised clinopyroxene grains shows a high concentration of low-angle boundaries $\leq 5^\circ$ (Fig. 4c). Misorientation axes cluster between the [010] and [001] axes, and close to the [111] axes (Fig. 4d).

4.3.2. Plagioclase-rich layers

Internal lattice distortion of plagioclase grains within the bands is mainly observed as peaks of low-angle misorientations close to the boundaries of the larger grains ($\sim 70 \mu\text{m}$; Fig. 5a) and as peaks in misorientations due to twinning (Fig. 5c). On the other hand, the smaller grains ($\leq 25 \mu\text{m}$) show a more homogeneous intracrystalline orientation; few small grains have low angle boundaries. Some grains show abrupt lattice bending, while others contain a gradual change from a nearly homogeneous intracrystalline orientation in the centre to a high density of dislocations located at grain boundaries (Fig. 5a).

The crystallographic fabric of the plagioclase-rich layers is characterized by a weak (J - and M -index 2.5 and 0.02, respectively) preferred orientation of [100] axes that align close to X , and poles to (010) planes that cluster around Z (Fig. 5b). The (001) planes are oriented at an oblique angle to Y , clustering in an intermediate position between Y and X (Fig. 5b).

Misorientation angles between neighbour grains have a higher frequency at angles from 2 to 15°, and at $\sim 180^\circ$, which are indicative of albite twinning (Fig. 5c). The misorientation axes for angles between 2 and 10° have maxima at [100] and close to [001] (Fig. 5d).

4.3.3. Polyphase matrix

Grains of plagioclase, clinopyroxene, orthopyroxene, and amphibole in the polyphase matrix have very weak CPO patterns (J - and M -index ranging from 1.2 to 1.9 and 0.01–0.02, respectively), with mostly diffuse characteristics (Fig. 6; 7). However, a non-random CPO develops for all grains. Fine-grained trails of plagioclase (Fig. 6a) show concentrations of [100] axes close to X (Fig. 6b). Poles to (010) cluster between Z and Y , while poles to (001) have a two-fold configuration at intermediate positions between Z and Y (Fig. 6b). Misorientation angles between neighbour grains deviate from the uniform theoretical curve at angles smaller than 15° and close to 180° (albite twinning; Fig. 6c). The misorientation axes for angles between 2° and 10° have a maximum close to [101] (Fig. 6d), which is also correlated with the main rotation axis observed in the distribution of (001) poles (Fig. 6b).

Clinopyroxene has poles to (100) planes distributed between Y and Z (Fig. 6b). Poles to (010) align parallel to Z and the [001] axes are mostly parallel to X (Fig. 6b). Misorientation angles between neighbour grains have the highest frequencies at angles smaller than 5°, and frequency peaks close to 60° and 100° (Fig. 6c). Misorientation axes for angles between 2° and 10° show scattered maxima and submaxima across the inverse pole figure (Fig. 6d).

Orthopyroxene grains show poles to (100) planes clustered between Y and Z (Fig. 6b). Poles to (010) tend to form a girdle oriented at an angle to the XY plane (Fig. 6b). The [001] axes are oriented close to X and with clusters between X and Z , close to the periphery of the diagram. Misorientation angles between neighbour grains have a higher frequency than a random distribution at angles smaller than $\sim 15^\circ$, and

small frequency peaks at 30°, 45° and 80° (Fig. 6c). The misorientation axes for angles between 2° and 10° cluster close to [110], though local submaxima are spread across the inverse pole figure (Fig. 6d).

Amphibole grains mixed with plagioclase and ilmenite (Fig. 6a) show little to no internal misorientation (Fig. 7a) and have (100) planes forming maxima around Z, while poles to (010) cluster in Y and between Y and Z (Fig. 7b). The [001] axes are oriented subparallel to X (Fig. 7b). A higher frequency of misorientation angles between 2° to 60° deviates from the theoretical random curve (Fig. 6c). Misorientation axes for angles between 2° and 10° have a tendency to cluster close to [010] and [001] (Fig. 7d).

4.4. Mineral chemistry

The anorthite content in the porphyroclasts and recrystallised grains of plagioclase commonly overlaps (An_{49–64}; average An₅₅; Fig. 8a). No systematic variations are observed through the microstructural domains, and plagioclase composition of porphyroclasts, monomineralic layers, and the polyphase mixture is labradorite.

The clinopyroxene porphyroclasts and recrystallised grains are mostly diopside with [Ca_{0.45–0.43},Mg_{0.43–0.40},Fe_{0.16–0.12}]SiO₃ compositions. Clinopyroxene porphyroclasts have higher Al and X_{Mg} (Mg/(Mg + Fe²⁺)) contents than the recrystallised grains (Fig. 8b).

The orthopyroxene porphyroclasts and recrystallised grains have average enstatite compositions of [Ca_{0.03–0.02},Mg_{0.61},Fe_{0.37–0.36}]SiO₃. Orthopyroxene porphyroclasts have higher Al contents (~0.04–0.05 atoms per formula unit – apfu) than the recrystallised grains (~0.025–0.035 apfu; Fig. 8c). X_{Mg} values for the porphyroclasts and recrystallised grains vary primarily between 62 and 63.5, with few recrystallised grains with contents down to 60.5 (Fig. 8c).

Amphibole grains comprise pargasite and Mg-hastingsite compositions. X_{Mg} values range from 67 to 80 and silica content varies from 6.12 to 6.27 with a negative correlation (Fig. 9). The ^{iv}Al (0.16–0.50 apfu) and alkalis (59–76) contents show a negative correlation (Fig. 9), without systematic variations between pyroxene-derived amphibole grains and those in the fine-grained matrix. The values of F and Cl in amphibole vary from 500 to 2000 ppm and 10–350 ppm, respectively (Fig. 10).

4.5. Thermodynamic modelling

The P–T pseudosection (Fig. 11) was calculated for a shear zone in sample 69R in the intervals of 750–1100 °C and 0–5 kbar, using a bulk rock composition (wt. %) of SiO₂ = 52.78; TiO₂ = 0.44; Al₂O₃ = 18.63; FeO = 4.47; MgO = 6.26; CaO = 13.19; Na₂O = 3.53; O₂ = 0.20; H₂O = 0.50. Melting starts at ~750 °C at 5 kbar and ~920 °C at 1 kbar (Fig. 11), considering 0.5 wt% of water content. The field containing the observed synkinematic mineral assemblage (clinopyroxene + orthopyroxene + amphibole + olivine + plagioclase + ilmenite + magnetite) is only stable in the presence of melt at conditions of 900–980 °C and 2.2–4.7 kbar (Fig. 11). Isopleths of anorthite content in plagioclase and vol% of olivine were used to constrain the stability field of the mineral assemblage. The intersection of isopleths corresponding to 55–60 mol.% of anorthite in plagioclase and 0.5 vol% of olivine constrained metamorphic conditions of 900–920 °C and 2.2–2.7 kbar (Fig. 11).

Additional thermometric constraints were assessed via hornblende-plagioclase geothermometry (Holland and Blundy, 1994). The microstructural sites at which these syn-kinematic pairs were analysed are illustrated in Fig. 12. The equilibrium temperatures calculated through edenite–richterite pairs are in the range of 835 and 900 °C (average of 875 ± 21 °C; Fig. 12a–b). These results are slightly lower than the estimates obtained from the thermodynamic modelling (Fig. 11).

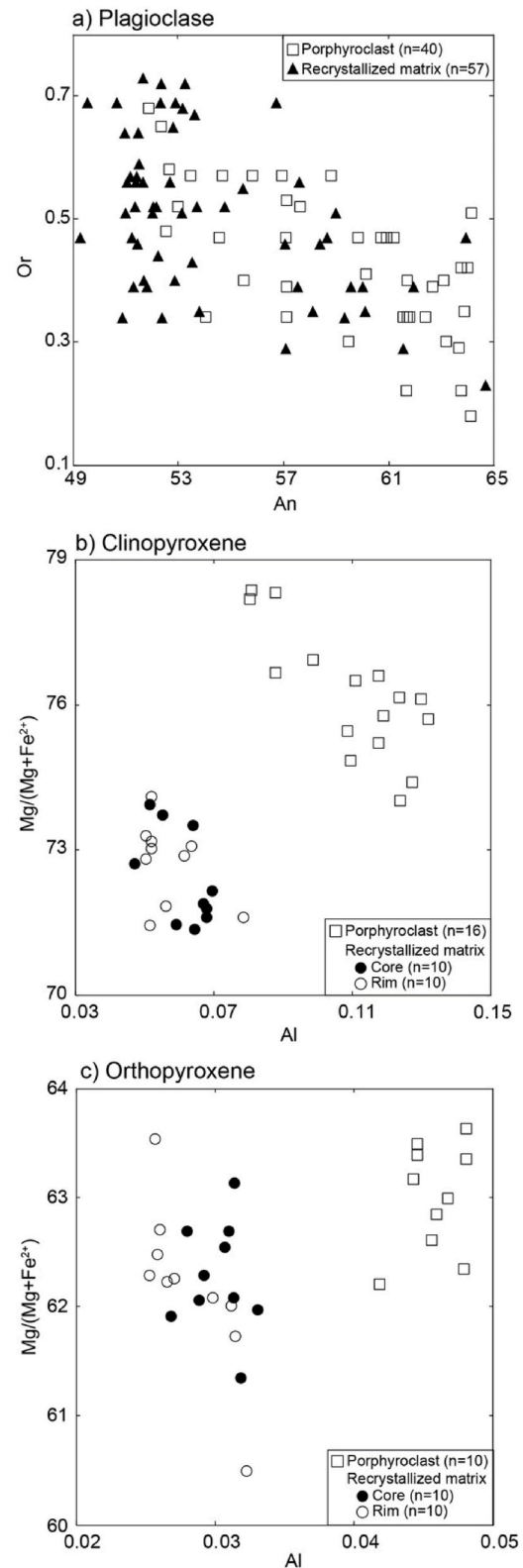


Fig. 8. Chemical compositions of plagioclase (a), clinopyroxene (b), and orthopyroxene (c) from porphyroclasts and recrystallised grains (sample 69R). (a) The An content in porphyroclasts and recrystallised grains of plagioclase overlaps. (b) and (c) The #Mg and Al content in recrystallised grains of clinopyroxene and orthopyroxene is lower than in the porphyroclasts. See text for discussion.

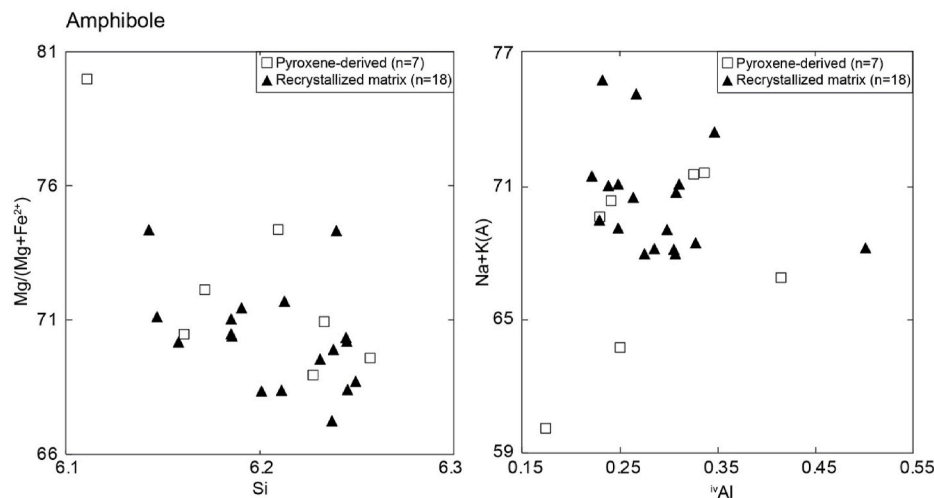


Fig. 9. Chemical compositions of amphibole from pyroxene-derived grains and grains in the matrix (sample 69R). Amphibole grains derived from pyroxene have similar composition as interstitial amphibole in the matrix, while alkalis show a negative correlation between both domains. See text for discussion.

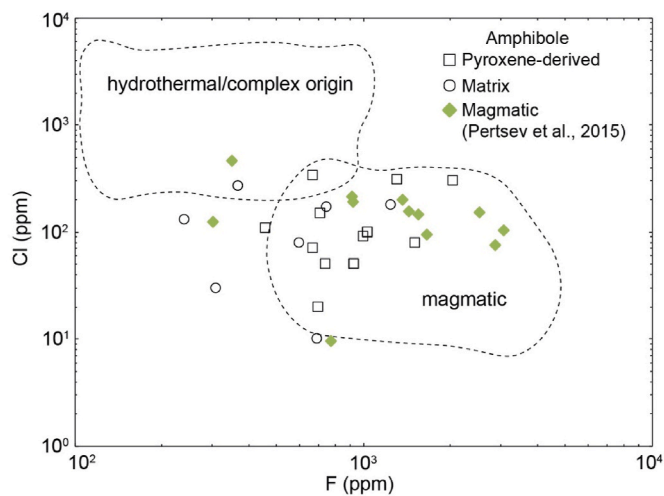


Fig. 10. F versus Cl content of amphibole in the matrix and derived from pyroxene (sample 69R). The region inside the dashed lines was determined based on the maximum and minimum values of F and Cl in amphibole interpreted as formed from interaction of ocean water/unknown origin (hydrothermal/complex origin) and magmatic fluids (magmatic) reported in Coogan et al. (2001). The green diamonds show the composition of amphibole originated from interaction of magmatic fluids with the surrounding gabbro (Pertsev et al., 2015). (For interpretation of the references to colour in this figure legend, the reader is referred to the Web version of this article.)

5. Discussion

5.1. Pressure and temperature conditions of deformation

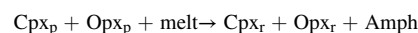
Thermodynamic modelling results agree with the petrographic and microstructural observations that indicate deformation under high-temperature conditions (Fig. 2). When combining the anorthite content in the recrystallised plagioclase (An_{55-60}) with the modal proportion of olivine (0.5–1 vol%) within the stability field of the observed synkinematic mineral assemblage, the isopleths restrict a narrow field of 900–920 °C and 2.2–2.7 kbar (Fig. 11). Estimates of deformation temperatures using the hornblende-plagioclase geothermometry result in metamorphic conditions of 835–900 °C (Fig. 12). Such results indicate that mylonitization initiated at low-pressure ultrahigh temperature conditions, followed by retrograde re-equilibration under granulite

facies conditions during exhumation.

Plagioclase porphyroclasts and recrystallised grains lack systematic variations in anorthite content (Fig. 8a) suggesting that deformation of plagioclase occurred under isochemical conditions (e.g., Mehl and Hirth, 2008). On the other hand, the lower Al content in fine-grained, recrystallised grains of clinopyroxene and orthopyroxene (Fig. 8b–c) and the lower values of X_{Mg} in the recrystallised grains of clinopyroxene indicate that these grains experienced changes in equilibrium compositions during recrystallisation within the shear zones.

The chemical composition of amphibole in both the pyroxene-derived aggregates and in the recrystallised matrix is similar (Fig. 9), suggesting that amphibole was formed during mylonitization. The presence of amphibole as: i) interstitial phase in recrystallised clinopyroxene aggregates (Fig. 2c); ii) small grains at the edges of clinopyroxene porphyroclasts; iii) interstitial phase along orthopyroxene grain boundaries (Fig. 2e); and iv) interstitial, undeformed phase in the fine-grained matrix (Fig. 6a; 7a), suggests that amphibole was formed by reaction-induced replacement of both clinopyroxene and orthopyroxene, which could be caused by infiltration of a late-stage intercumulus hydrous melt (Dick et al., 2019a), or by in situ melt-consumption during back-reaction. Modelled phase relations (Fig. 11) favour the second hypothesis.

The following reaction may explain the generation of amphibole at the expense of clinopyroxene (Cpx_p) and orthopyroxene (Opx_p) porphyroclasts, and the recrystallised grains of clinopyroxene (Cpx_r) and orthopyroxene (Opx_r) present in the shear zones (Smith, 2014):



Ti-rich amphibole (pargasite) is the major high-temperature hydrous phase in gabbro from the lower oceanic crust (e.g., Natland and Dick, 2001; Pertsev et al., 2015). It can form by interaction of a highly evolved hydrated melt with the crystal mush and by reaction of high-temperature seawater-derived aqueous fluids with the gabbro (e.g., Pertsev et al., 2015). As a result, amphibole composition changes in response to the nature of the interacting fluid. For example, seawater-derived fluids have relatively high content of Cl (~20,000 ppm; e.g., Von Damm et al., 1990) and low F values (~2 ppm; Faure, 1991). In contrast, magmatic melts are poor in Cl (~20–50 ppm) in primitive magmas and rich in F (>300 ppm; e.g., Michael and Schilling, 1989). The relative abundances of these elements in the amphibole crystal structure are controlled by the activity of Cl in the interacting fluid phase (hydrous melt or aqueous fluid).

F and Cl contents in amphibole grains derived from pyroxene clasts and in grains within the polyphase mixture in the shear zones from hole

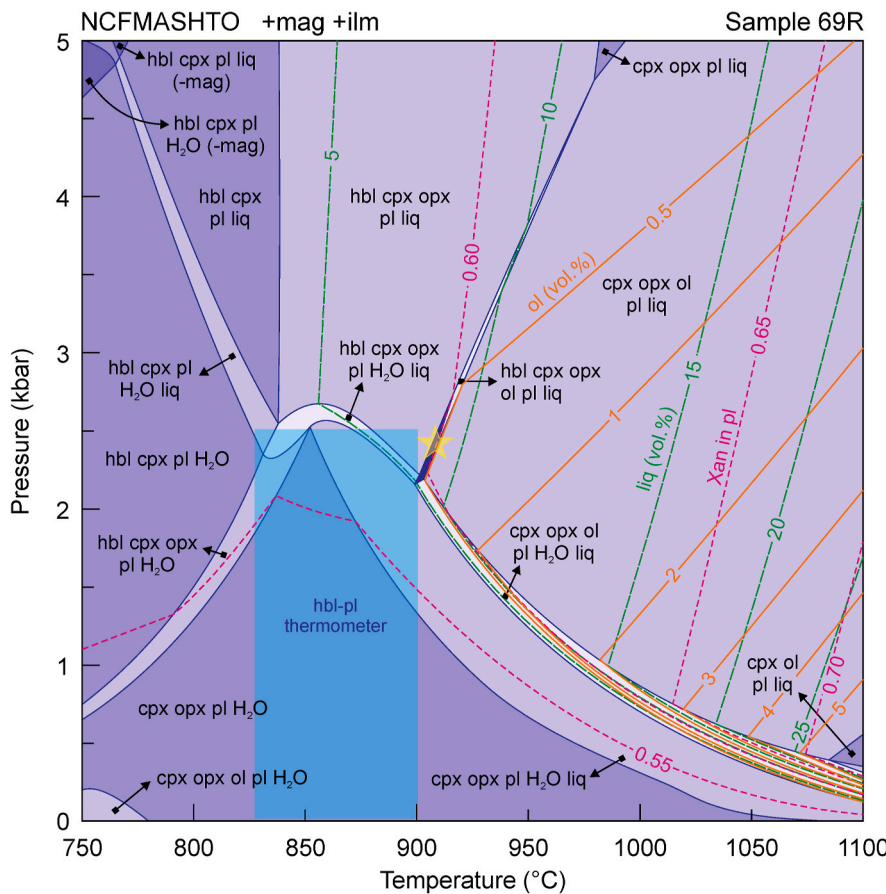


Fig. 11. Pseudosection for sample 69R. Isopleths of modal percentage of olivine (orange dashed lines), melt (green dashed line), and X_{AN} in plagioclase (red dashed line) are plotted. The yellow star represents the best-fit approach of P–T conditions of the syn-kinematic mineral assemblage based on the measured chemical and modal mineral composition of the sample. The light blue field represents temperature ranges estimated using Holland and Blundy (1994) hornblende-plagioclase thermometer. Estimated conditions of deformation are approximately 900–920 °C and 2.2–2.7 kbar, indicated by the dark blue field. See text for discussion. (For interpretation of the references to colour in this figure legend, the reader is referred to the Web version of this article.)

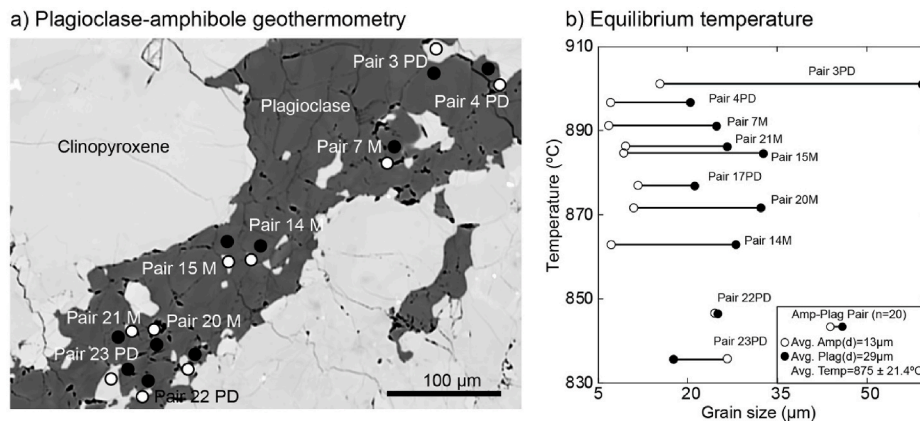


Fig. 12. Metamorphic/deformational temperatures estimated using the hornblende-plagioclase thermometer from Holland and Blundy (1994). (a) Backscatter electron image showing plagioclase and amphibole recrystallised aggregates on which microprobe measurements were performed. PD = pyroxene derived; M = matrix. (b) Grain size versus temperature graph showing the distribution of calculated equilibrium temperatures for the microstructural domain shown in (a).

U1473A are similar to those interpreted as formed from a high-temperature, evolved hydrous melt phase (Fig. 10; Coogan et al., 2001; Pertsev et al., 2015). Given the low water content of mid-ocean ridge basalts, the source of the fluid that stabilised the synkinematic amphibole was likely an evolved water-bearing silicate melt that interacted with the rock during deformation (Pertsev et al., 2015; Dick et al., 2019a). The presence of a low melt fraction (5–10 vol %) in equilibrium with the synkinematic solid metamorphic phases is predicted in the modelled phase diagram section for sample 69R at metamorphic conditions of 900–920 °C and 2.2–2.7 kbar (Fig. 11).

Thus, the presence of synkinematic hydrated amphibole in the gabbroic shear zones from hole U1473A constitutes evidence that fluid-assisted reactions were associated with mylonitization, which may have been triggered by a reactive in situ melt phase during back-reaction. Such melt–rock reactions have been systematically reported in deformed rocks from the lower crust (e.g., Gardner et al., 2020; Getzinger et al., 2013 and references therein).

5.2. Fracturing and development of core-mantle structures in porphyroclasts

Brittle deformation is observed as healed microfractures in porphyroclasts of orthopyroxene (Fig. 2d-e). The presence of a mechanically strong phase (orthopyroxene) deforming under high-temperature conditions with high proportion of crystal/melt ratios and high differential stress, may result in brittle behaviour of pyroxene – and nucleation of planar anisotropies – prior to the development of localised ductile flow (e.g., Handy et al., 2007; Okudaira et al., 2015). In addition, the observed healed fractures may have acted as preferred pathways for melt-assisted diffusion during shearing due to the presence of minute and cusp-like grains of amphibole and magnetite (Fig. 2e).

All porphyroclasts (i.e., clinopyroxene, orthopyroxene, plagioclase and olivine) show undulose extinction and have recrystallised grains along their margins (i.e., core and mantle microstructure; Fig. 2b, f, g; 4a), suggesting widespread evidence of crystal plasticity and grain size reduction being achieved mainly by dynamic recrystallisation (Hirth and Tullis, 1992).

The elongation of clinopyroxene porphyroclasts parallel to the foliation (Fig. 2a), extensive crystal bending (Fig. 2a-b; 4a), and CPO patterns of both porphyroclasts and surrounding neoblasts (Fig. 4b) indicate that clinopyroxene deforms by the activation of the (010)[001] slip system. Although the surrounding neoblasts tend to inherit the porphyroclast CPO, this relation is unclear (Fig. 4b). The concentration of some (001) planes and poles to (100) parallel to the XY plane and X direction, respectively, is not directly related with known slip systems in clinopyroxene, because any potential glide plane should slip along the close packed tetrahedral SiO_4 chains that are parallel to the [001] axis (Cameron and Papike, 1981).

A possible explanation for the activation of the (001)[100] slip system in some of the clinopyroxene neoblasts is mechanical twinning. Although the most common twinning system in clinopyroxene is (001)[100], glide on the (100)[001] twin system has been documented on optical and transmission electron microscope in naturally (e.g., Philippot and van Roermund, 1992) and experimentally (e.g., Avé Lallemant, 1978; Kirby and Kronenberg, 1984) deformed pyroxene-bearing aggregates and may, in part, reflect fluctuations in strain rate during deformation (Philippot and van Roermund, 1992).

Such patterns, which are consistent with the misorientation axes clustered between [010] and [001], have been interpreted as indicative of the activation of dislocation creep mechanisms, as reported in experimentally (e.g., Bascou et al., 2002) and naturally (e.g., Degli Alessandrini et al., 2017) deformed aggregates. The high frequency of misorientation angles smaller than 20° between neighbour grains supports the activation of dislocation creep and dynamic recrystallisation as a recovery mechanism in the formation of the mantling neoblasts at the edges of the porphyroclasts (Fig. 4c).

Thus, our results suggest that deformation in the porphyroclasts was accommodated by combined mechanical fragmentation and crystal plasticity at the clasts edges (core and mantle microstructures), resulting in fractured grains rimmed by recrystallised, mantling neoblasts (Bial and Trepmann, 2013; Okudaira et al., 2017).

5.3. Dynamic recrystallisation in the plagioclase-rich layers

The microstructures (e.g., undulose extinction, subgrain boundaries close to the grain edge; Fig. 5a) indicate that deformation was accommodated by crystal plasticity within the plagioclase-rich layers. The CPO pattern, although weak in terms of texture strength, shows a non-random alignment of poles to (010) planes and [100] axes close to Z and X directions, respectively (Fig. 5b), which may be taken as indicative of activation of the (010)[100] slip system (e.g., Ji and Mainprice, 1990; Mehl and Hirth, 2008).

The misorientation axes around [100] and close to [001] (Fig. 5d) suggest the activity of dislocation glide during intracrystalline

deformation (e.g., Mehl and Hirth, 2008 and references therein). The equigranular microfabrics in the plagioclase-rich layers with triple junctions, similar grain size of subgrains and recrystallised neoblasts adjacent to the porphyroclasts, and high frequency of misorientation angles $<20^\circ$ (Fig. 5c), indicate that the plagioclase-rich layers formed via subgrain rotation recrystallisation. In monomineralic aggregates typical of the mid- and lower crust, larger grain sizes are expected because grain growth is not hindered by phase pinning; thus, dislocation creep is more efficiently activated than diffusion creep (e.g., Paterson, 1990). We found that the average grain size of plagioclase in the plagioclase-rich layers is larger ($88 \mu\text{m}$) than in the polyphase matrix ($24 \mu\text{m}$), allowing the activation of grain size insensitive mechanisms.

Therefore, the present dataset indicates that plagioclase-rich layers formed mainly through dislocation creep evidenced by the activation of the (010)[100] slip system. The monomineralic bands wrap around coarse porphyroclasts and are in abrupt contact with the polyphase mixture, ultimately being parallel to the ductile flow. A similar mechanical behaviour has been documented by Mehl and Hirth (2008), who reported on the parallelism of the orientation of slip planes of plagioclase CPO with the shear plane during high-temperature, crystal-plastic deformation.

5.4. Strain localisation in the fine-grained, polyphase mixture

In the polyphase mixture, the microstructural evidence of: i) weak to no presence of crystal plasticity; ii) small grain size associated with phase mixing (Fig. 3c-d; 6a; e.g., Dimanov et al., 2007; Mehl and Hirth, 2008); and iii) very weak fabric strength (Figs. 6b and 7b; e.g., Bestmann and Prior, 2003), all point to the activity of diffusion creep in the formation of the fine-grained, mixed aggregates (e.g., Mehl and Hirth, 2008; Okudaira et al., 2015; Degli Alessandrini et al., 2017).

Although the microstructural dataset indicates that the fine-grained mixture was formed by diffusion creep, there is a non-random CPO in the individual phases from the polyphase matrix (i.e., plagioclase, clinopyroxene, orthopyroxene and amphibole; Figs. 6b and 7b). Furthermore, all phases show peaks of low-angle misorientation angles that deviate from the theoretical random distribution (Figs. 6c and 7c) and weak clustering of misorientation axes between 2 and 10° in the inverse pole figure (Figs. 6d and 7d). Such observations indicate that there is evidence for crystallographic-controlled processes accommodating the development of the microfabrics in the polyphase matrix (e.g., Halfpenny et al., 2006).

Oriented grain growth associated with grain boundary sliding in the diffusion creep regime has been reported as a mechanism that can lead to the development of a weak to moderate CPO in fine-grained aggregates of plagioclase (e.g., Barreiro et al., 2007; Soda et al., 2019), clinopyroxene and orthopyroxene (e.g., Degli Alessandrini et al., 2017), and amphibole (e.g., Getsinger et al., 2013). In these cases, the presence of a non-random CPO resulted from a kinematically-controlled combination of rigid-body rotation and anisotropic diffusion rate along the crystallographic direction with the fastest rate of diffusion growth (e.g., Bons and Den Brok, 2000). Experimental studies have shown that the [001] axis is the direction of fast diffusion rate in clinopyroxene (e.g., Mauler et al., 2000) and amphibole (e.g., Getsinger and Hirth, 2014). Similar CPO fabrics observed in naturally deformed clinopyroxene (e.g., Degli Alessandrini et al., 2017) and amphibole (e.g., Okudaira et al., 2015) have been interpreted as a result of oriented grain growth during grain size sensitive creep. In the gabbroic shear zones from this study, plagioclase has the [100] axes parallel to the X direction while clinopyroxene, orthopyroxene, and amphibole have the [001] axes parallel to the X direction (Figs. 6b and 7b), while the long axes of all grains are oriented parallel to the foliation. These CPO patterns reflect the local flow field as a result of the grain shape fabric produced during oriented grain growth in the diffusion creep regime (e.g., Okudaira et al., 2015; Van der Werf et al., 2017).

The similar distribution of uncorrelated and theoretical

misorientation angles, and the high frequencies of misorientation for angles smaller than 80° (Fig. 6c) support the activity of diffusion creep, as grain boundary sliding (GBS) promotes the increase in misorientation angles by grain switching and rotation of neighbouring grains (e.g., Halfpenny et al., 2006; Miranda and Klepeis, 2016). Moreover, a matrix deforming via diffusion creep and grain boundary sliding may inherit part of the low angle misorientation axes developed during switch from dislocation creep to diffusion creep as a result of grain size reduction by subgrain rotation recrystallisation. Similar observations have been made by Miranda and Klepeis (2016), who found that the weak CPO and clustering of misorientation axes in fine-grained plagioclase were produced during diffusion creep due to grain size reduction by subgrain rotation recrystallisation. This may explain the occurrence of angles smaller than 10° between neighbouring grains in the polyphase matrix (Fig. 6c).

Taken together, the strain free interstitial character (as evidenced by microstructures and the low misorientation differences in the grains (Fig. 7a)) and the overgrowth of amphibole in strain shadows of pyroxene within the polyphase matrix suggest that amphibole grows at the expense of pyroxene in the presence of a melt phase. Although locally preserved, evidence for the former presence of melt is observed as low dihedral angles and cusp-like features of amphibole and ilmenite/magnetite along grain boundaries (Fig. 2e; 3d; Lee et al., 2018; Stuart et al., 2018). As strain tends to be localised in regions deforming by diffusive processes, the hydrous melt was probably channelised more easily in the polyphase matrix deforming by grain size sensitive mechanisms. As a result, mineral reactions are enhanced and a positive feedback between deformation and local growth of new smaller phases is favoured (e.g., Marti et al., 2018), facilitating phase mixing, preventing grain growth and sustaining diffusive processes (e.g., Mansard et al., 2020; Marti et al., 2018).

Thus, we conclude that the accommodation of strain in the fine-grained, polyphase mixture was attained mainly via diffusion-assisted GBS in which grain growth is controlled by internal lattice anisotropy of the grains in response to the kinematic framework. Grain size reduction and phase mixing were maintained by Zener pinning (Bercovici and Ricard, 2012), a common process observed in the lower oceanic crust that can potentially hinder grain growth, leading to accommodation of large strains while consistently reducing the overall strength of the bulk rock (Maierová et al., 2017; Mansard et al., 2020; Mehl and Hirth, 2008).

5.5. Strength of the lower oceanic crust of Atlantis Bank

The combination of fracturing, viscous-flow (dislocation creep and diffusion creep) and reaction softening mechanisms in the presence of melt suggests that ductile shear zones efficiently localise the deformation in the deepest parts of the Atlantis Bank (Hirth et al., 1998).

Although we did not observe widespread microstructures indicative of melt–rock interaction (e.g., Gardner et al., 2020), the synkinematic amphibole after pyroxene indicates the activity of melt-consuming, back-reactions in the shear zones. The phase mixing, fine grain size and the interstitial character of fine-grained amphibole all indicate that the polyphase matrix deformed by grain size sensitive mechanisms in the presence of small amounts of melt (e.g., Okudaira et al., 2015). The presence of a melt phase may also have triggered fracturing in the mechanically stronger orthopyroxene porphyroclasts by high fluid pressure and local stress build-up (e.g., Dick et al., 2019b; Spiess et al., 2017).

Plagioclase recrystallisation implies that this mineral is the rheologically weak phase compared to pyroxene (e.g., Miranda and John, 2010). Such patterns have been also reported in dry mafic dikes (Degli Alessandrini et al., 2017) and gabbroic rocks (Mehl and Hirth, 2008) deformed under similar conditions and point to a matrix control in the rheology of the aggregate (e.g., Platt, 2015).

Extrapolation of experimentally-derived flow laws indicates that a fine-grained aggregate deforming in the diffusion creep regime is able to

more effectively localise strain because it deforms at faster strain rates than in the dislocation creep regime at a given differential stress (e.g., Mehl and Hirth, 2008; Viegas et al., 2016). The transition from grain-size-insensitive (GSI) to grain-size-sensitive (GSS) creep is suggested to explain the mechanism of strain localisation that led to exhumation of the Atlantis Bank at strain rates of 10^{-12} to 10^{-11} s⁻¹, based on high temperature sheared gabbros from ODP hole 735B (Mehl and Hirth, 2008; Miranda, 2006). In the presence of melt, this weakening may be even more pronounced because it produces fine-grained reaction products, enhances diffusion creep, and further promotes strain localisation (e.g., Degli Alessandrini et al., 2017; Hidas et al., 2016).

Thus, we postulate that exhumation of the lower sector of the Atlantis Bank oceanic core complex occurred through high-temperature, ductile shear zones that accommodated strain via a combination of mechanical fragmentation and viscous flow in the presence of small amounts of melt. Our results evidence the activity of crystal plasticity and melt–rock interaction in the high temperature parts the Atlantis Bank oceanic core complex, indicating that dynamic recrystallisation and melt-enhanced reaction-softening effectively localise strain in ductile shear zones developed at the deeper parts of exhumed core complexes (e.g., Gardner et al., 2020). Such patterns highlight the way strain is localised in the lower crust and point to a significant component of rheological weakening due to melt–rock interactions during large-scale detachment faulting in slow-spreading mid ocean ridges.

6. Conclusions

Analyses of microstructures, crystallographic fabrics, and P–T conditions of deformation in shear zones from the lower parts of hole U1473A in the Atlantis Bank oceanic core complex (Southwest Indian Ridge) indicate that strain was localised in ductile shear zones by brittle and plastic deformation mechanisms (dislocation and diffusion creep) in the presence of melt at conditions of approximately 900–920 °C and 2.2–2.7 kbar. The following conclusions can be drawn from this study:

- All porphyroclasts mainly deformed by dislocation creep as evidenced by undulose extinction and core and mantle microstructures. Grain size reduction is primarily achieved by subgrain rotation recrystallisation.
- Likewise, systematic intracrystalline plasticity indicates that the plagioclase-rich layers deformed by dislocation creep during viscous flow.
- The polyphase matrix formed as a result of grain size reduction and phase mixing. A very weak and non-random CPO in all grains points to crystallographic-controlled grain growth during diffusion-assisted grain boundary sliding.
- Amphibole grew at the expense of pyroxene grains possibly due to in situ melt-consumption and back-reaction during shearing and exhumation of the crust, further decreasing the grain size of the aggregate and enhancing phase mixing.

Our results indicate that the strength of the lower crust at slow-spreading ridges would be best modelled with flow laws for poly-mineralic aggregates in the presence of melt and reaction-softening mechanisms. Since strain tends to localise within the polymineralic matrix, the role of fluids in promoting reaction-softening and contributing to the development of fine-grained shear zones in otherwise dry gabbroic rock exert a significant control on the overall rheological behaviour of the lower oceanic crust. Such fluid–rock interactions are heterogeneous in character and shed light on the manner in which strain is partitioned/distributed in the footwall of oceanic core complexes during large-scale, detachment faulting.

Author statement

Rhander Taufner: Conceptualization, Data curation, Formal analysis, Investigation, Methodology, Validation, Visualization, Writing – original draft. **Gustavo Viegas:** Conceptualization, Data curation, Formal analysis, Investigation, Methodology, Validation, Visualization, Writing – review & editing, Supervision, Project administration, Funding acquisition. **Frederico Meira Faleiros:** Data curation, Formal analysis, Investigation, Methodology, Validation, Writing – review & editing. **Paulo Castellan:** Formal analysis, Investigation, Methodology. **Raylline Silva:** Formal analysis, Investigation, Methodology.

Declaration of competing interest

The authors declare that they have no known competing financial interests or personal relationships that could have appeared to influence the work reported in this paper.

Acknowledgments

This study was funded by the Coordenação de Aperfeiçoamento de Pessoal de Nível Superior – Brasil [CAPES – Finance Code 001] and Fundação de Amparo à Pesquisa do Distrito Federal [Grant Number 0193.001510/2017]. Frederico Faleiros thanks the National Council of Technological and Scientific Development, Brazil, for research productivity scholarship [CNPq – Grant Number 307732/2019–3]. We thank Luiz Morales of ETH Zurich for invaluable assistance during EBSD analysis. The scientific party of IODP Expedition 360 is warmly thanked for stimulating discussions that led to the development of this work. We thank two anonymous reviewers for their constructive comments which greatly enhanced our manuscript, and we also thank Editor Fabrizio Agosta for careful editorial handling. Our dear friend Alex Walsh is thanked for proofreading the manuscript. This paper is part of the first author's PhD thesis.

Appendix A. Supplementary data

Supplementary data to this article can be found online at <https://doi.org/10.1016/j.jsg.2021.104380>.

References

- Avé Lallemand, H.G., 1978. Experimental deformation of diopside and websterite. *Tectonophysics* 48, 1–27. [https://doi.org/10.1016/0040-1951\(78\)90083-5](https://doi.org/10.1016/0040-1951(78)90083-5).
- Bachmann, F., Hielscher, R., Schaeben, H., 2010. Texture analysis with MTEX – free and open source software toolbox. *Solid State Phenom.* 160, 63–68.
- Bachmann, F., Hielscher, R., Schaeben, H., 2011. Grain detection from 2d and 3d EBSD data Specification of the MTEX algorithm. *Ultramicroscopy* 111, 1720–1733. <https://doi.org/10.1016/j.ultramicro.2011.08.002>.
- Barreiro, J.G., Lonardelli, I., Wenk, H.R., Dresen, G., Rybacki, E., Ren, Y., Tomé, C.N., 2007. Preferred orientation of anorthite deformed experimentally in Newtonian creep. *Earth Planet. Sci. Lett.* 264, 188–207. <https://doi.org/10.1016/j.epsl.2007.09.018>.
- Bascou, J., Tommasi, A., Mainprice, D., 2002. Plastic deformation and development of clinopyroxene lattice preferred orientations in eclogites. *J. Struct. Geol.* 24, 1357–1368. [https://doi.org/10.1016/S0191-8141\(01\)00137-7](https://doi.org/10.1016/S0191-8141(01)00137-7).
- Bercovici, D., Ricard, Y., 2012. Mechanisms for the generation of plate tectonics by two-phase grain-damage and pinning. *Phys. Earth Planet. In.* 202–203, 27–55.
- Bestmann, M., Prior, D.J., 2003. Intragranular dynamic recrystallization in naturally deformed calcite marble: diffusion accommodated grain boundary sliding as a result of subgrain rotation recrystallization. *J. Struct. Geol.* 25, 1597–1613. [https://doi.org/10.1016/S0191-8141\(03\)00006-3](https://doi.org/10.1016/S0191-8141(03)00006-3).
- Bial, J., Trepmann, C.A., 2013. The microstructural record of porphyroclasts and matrix of partly serpentinized peridotite mylonites - from brittle and crystal-plastic deformation to dissolution-precipitation creep. *Solid Earth* 4, 315–330. <https://doi.org/10.5194/se-4-315-2013>.
- Blackman, D.K., Cann, J.R., Janssen, B., Smith, D.K., 1998. Origin of extensional core complexes: evidence from the mid-atlantic ridge at Atlantis fracture zone. *J. Geophys. Res.: Solid Earth* 103, 21315–21333. <https://doi.org/10.1029/98JB01756>.
- Bons, P.D., Den Brok, B., 2000. Crystallographic preferred orientation development by dissolution-precipitation creep. *J. Struct. Geol.* 22, 1713–1722. [https://doi.org/10.1016/S0191-8141\(00\)00075-4](https://doi.org/10.1016/S0191-8141(00)00075-4).
- Bunge, H.J., 1982. *Texture Analysis in Materials Science: Mathematical Methods*. Butterworths, London.
- Cameron, M., Papike, J.J., 1981. Structural and chemical variations in pyroxenes. *Am. Mineral.* 66, 1–50.
- Cann, J.R., Blackman, D.K., Smith, D.K., McAllister, E., Janssen, B., Mello, S., Avgerinos, E., Pascoe, A.R., Escartin, J., 1997. Corrugated slip surfaces formed at ridge-transform intersections on the Mid-Atlantic Ridge. *Nature* 385, 329–332. <https://doi.org/10.1038/385329a0>.
- Cannat, M., 1991. Plastic deformation at an oceanic spreading ridge: a microstructural study of Site 735 gabbros (Southwest Indian Ocean). In: *Proceedings of the Ocean Drilling Program, 118 Scientific Results*. Ocean Drilling Program. <https://doi.org/10.2973/odp.proc.sr.118.134.1991>.
- Cannat, M., Sauter, D., Mendel, V., Ruellan, E., Okino, K., Escartin, J., Combier, V., Baala, M., 2006. Modes of seafloor generation at a melt-poor ultraslow-spreading ridge. *Geology* 34, 605. <https://doi.org/10.1130/G22486A.1>.
- Carreras, J., Czeck, D.M., Druguet, E., Hudleston, P.J., 2010. Structure and development of an anastomosing network of ductile shear zones. *J. Struct. Geol.* 32, 5. <https://doi.org/10.1016/j.jsg.2010.03.013>.
- Connolly, J.A.D., 2005. Computation of phase equilibria by linear programming: a tool for geodynamic modeling and its application to subduction zone decarbonation. *Earth Planet. Sci. Lett.* 236, 524–541. <https://doi.org/10.1016/J.EPSL.2005.04.033>.
- Coogan, L.A., Wilson, R.N., Gillis, K.M., MacLeod, C.J., 2001. Near-solidus evolution of oceanic gabbros: insights from amphibole geochemistry. *Geochem. Cosmochim. Acta* 65, 4339–4357. [https://doi.org/10.1016/S0016-7037\(01\)00714-1](https://doi.org/10.1016/S0016-7037(01)00714-1).
- Degli Alessandrini, G., Menegon, L., Malaspina, N., Dijkstra, A.H., Anderson, M.W., 2017. Creep of mafic dykes infiltrated by melt in the lower continental crust (Seiland Igneous Province, Norway). *Lithos* 274–275, 169–187. <https://doi.org/10.1016/j.lithos.2016.12.030>.
- Dick, H.J.B., Kvassnes, A.J.S., Robinson, P.T., MacLeod, C.J., Kinoshita, H., 2019a. The Atlantis Bank gabbro massif, southwest Indian ridge. *Progress in Earth and Planetary Science* 6, 64. <https://doi.org/10.1186/s40645-019-0307-9>.
- Dick, H.J.B., MacLeod, C.J., Blum, P., 2016. Expedition 360 preliminary report: southwest Indian Ridge Lower crust and Moho. In: *International Ocean Discovery Program*. <https://doi.org/10.14379/iodp.pr.360.2016>.
- Dick, H.J.B., MacLeod, C.J., Blum, P., Abe, N., Blackman, D.K., Bowles, J.A., Cheadle, M. J., Cho, K., Ciazęła, J., Deans, J.R., Edgcomb, V.P., Ferrando, C., France, L., Ghosh, B., Ildefonse, B., John, B., Kendrick, M.A., Koepke, J., Leong, J.A.M., Liu, C., Ma, Q., Morishita, T., Morris, A., Natland, J.H., Nozaka, T., Pluempner, O., Sanfilippo, A., Sylvan, J.B., Tivey, M.A., Tribuzio, R., Viegas, G., 2019b. Dynamic accretion beneath a slow-spreading ridge segment: IODP Hole 1473A and the Atlantis Bank oceanic core complex. *J. Geophys. Res.: Solid Earth* 124, 1–29. <https://doi.org/10.1029/2018JB016858>.
- Dick, H.J.B., Meyer, P.S., Bloomer, S., Kirby, S., Stakes, D., Mawer, C., 1991. Lithostratigraphic evolution of an in-situ section of oceanic layer. In: *Proceedings of the Ocean Drilling Program, 118 Scientific Results*. Ocean Drilling Program. <https://doi.org/10.2973/odp.proc.sr.118.128.1991>.
- Dick, H.J.B., Natland, J.H., Alt, J.C., Bach, W., Bideau, D., Gee, J.S., Haggas, S., Hertogen, J.G.H., Hirth, G., Holm, P.M., Ildefonse, B., Iturrino, G.J., John, B.E., Kelley, D.S., Kikawa, E., Kingdon, A., LeRoux, P.J., Maeda, J., Meyer, P.S., Miller, D. J., Naslund, H.R., Niu, Y.-L., Robinson, P.T., Snow, J., Stephen, R.A., Trimby, P.W., Worm, H.-U., Yoshinobu, A., 2000. A long in situ section of the lower ocean crust: results of ODP Leg 176 drilling at the Southwest Indian Ridge. *Earth Planet. Sci. Lett.* 179, 31–51. [https://doi.org/10.1016/S0012-821X\(00\)00102-3](https://doi.org/10.1016/S0012-821X(00)00102-3).
- Dimanov, A., Rybacki, E., Wirth, R., Dresen, G., 2007. Creep and strain-dependent microstructures of synthetic anorthite-diopside aggregates. *J. Struct. Geol.* 29, 1049–1069. <https://doi.org/10.1016/j.jsg.2007.02.010>.
- Escartin, J., Mével, C., MacLeod, C.J., McCaig, A.M., 2003. Constraints on deformation conditions and the origin of oceanic detachments: the Mid-Atlantic Ridge core complex at 15°45'N. *G-cubed* 4, 1067. <https://doi.org/10.1029/2002GC000472>.
- Faure, G., 1991. *Principles and Applications of Geochemistry*. Prentice Hall, Englewood Cliffs, NJ.
- Gardner, R.L., Piazzolo, S., Daczko, N.R., Trimby, P., 2020. Microstructures reveal multistage melt present strain localisation in mid-ocean gabbros. *Lithos* 366–367, 105572. <https://doi.org/10.1016/j.lithos.2020.105572>.
- Getsinger, A.J., Hirth, G., 2014. Amphibole fabric formation during diffusion creep and the rheology of shear zones. *Geology* 42, 535–538. <https://doi.org/10.1130/G35327.1>.
- Getsinger, A.J., Hirth, G., Stünitz, H., Goergen, E.T., 2013. Influence of water on rheology and strain localization in the lower continental crust. *G-cubed* 14, 2247–2264. <https://doi.org/10.1002/ggge.20148>.
- Green, E.C.R., White, R.W., Diener, J.F.A., Powell, R., Holland, T.J.B., Palin, R.M., 2016. Activity-composition relations for the calculation of partial melting equilibria in metabasic rocks. *J. Metamorph. Geol.* 34, 845–869. <https://doi.org/10.1111/jmg.12211>.
- Halfpenny, A., Prior, D.J., Wheeler, J., 2006. Analysis of dynamic recrystallization and nucleation in a quartzite mylonite. *Tectonophysics* 427, 3–14. <https://doi.org/10.1016/j.tecto.2006.05.016>.
- Handy, M.R., Hirth, G., Bürgmann, R., 2007. Continental fault structure and rheology from the frictional-to-viscous transition downward. In: *Handy, M., Hirth, G., Hovius, N. (Eds.), Tectonic Faults: Agents of Change on a Dynamic Earth*. Mass, Berlin: MIT Press, Cambridge, pp. 131–181 in cooperation with the Freie Universität Berlin.
- Hansen, L.N., Cheadle, M.J., John, B.E., Swapp, S.M., Dick, H.J.B., Tuelholke, B.E., Tivey, M.A., 2013. Mylonitic deformation at the Kane oceanic core complex: implications for the rheological behavior of oceanic detachment faults. *G-cubed* 14, 3085–3108. <https://doi.org/10.1002/ggge.20184>.

- Hidas, K., Tommasi, A., Garrido, C.J., Padrón-Navarta, J.A., Mainprice, D., Vauchez, A., Barou, F., Marchesi, C., 2016. Fluid-assisted strain localization in the shallow subcontinental lithospheric mantle. *Lithos* 262, 636–650. <https://doi.org/10.1016/J.LITHOS.2016.07.038>.
- Hielscher, R., Schaeben, H., 2008. A novel pole figure inversion method: specification of the MTEX algorithm. *J. Appl. Crystallogr.* 41, 1024–1037. <https://doi.org/10.1107/S0021889808030112>.
- Hirth, G., Escartin, J., Lin, J., 1998. The rheology of the lower oceanic crust: implications for lithospheric deformation at mid-ocean ridges. In: Buck, W.R., et al. (Eds.), *Faulting and Magmatism at Mid-Ocean Ridges*, Geophysical Monograph Ser, vol. 106. AGU, Washington, D.C, pp. 291–303.
- Hirth, G., Tullis, J., 1992. Dislocation creep regimes in quartz aggregates. *J. Struct. Geol.* 14, 145–159. [https://doi.org/10.1016/0191-8141\(92\)90053-Y](https://doi.org/10.1016/0191-8141(92)90053-Y).
- Holland, T., Blundy, J., 1994. Non-ideal interactions in calcic amphiboles and their bearing on amphibole-plagioclase thermometry. *Contrib. Mineral. Petrol.* 116, 433–447.
- Holland, T., Powell, R., 1998. An internally consistent thermodynamic data set for phases of petrological interest. *J. Metamorph. Geol.* 16, 309–343. <https://doi.org/10.1111/j.1525-1314.1998.00140.x>.
- Holland, T., Powell, R., 2003. Activity-composition relations for phases in petrological calculations: an asymmetric multicomponent formulation. *Contrib. Mineral. Petrol.* 145, 492–501. <https://doi.org/10.1007/s00410-003-0464-z>.
- Holland, T., Powell, R., 2011. An improved and extended internally consistent thermodynamic dataset for phases of petrological interest, involving a new equation of state for solids. *J. Metamorph. Geol.* 29, 333–383. <https://doi.org/10.1111/j.1525-1314.2010.00923.x>.
- Ildefonse, B., Blackman, D.K., John, B.E., Ohara, Y., Miller, D.J., MacLeod, C.J., 2007. Oceanic core complexes and crustal accretion at slow-spreading ridges. *Geology* 35, 623–626. <https://doi.org/10.1130/G23531A.1>.
- Ji, S., Mainprice, D., 1990. Recrystallization and fabric development in plagioclase. *J. Geol.* 98, 65–79. <https://doi.org/10.1086/g29375>.
- Kirby, S.H., Kronenberg, A.K., 1984. Deformation of clinopyroxene: evidence for a transition in flow mechanisms and semibrittle behavior. *J. Geophys. Res.* 89, 3177–3192. <https://doi.org/10.1029/JB089iB05p03177>.
- Lee, A.L., Torvela, T., Lloyd, G.E., Walker, A.M., 2018. Melt organisation and strain partitioning in the lower crust. *J. Struct. Geol.* 113, 188–199.
- MacLeod, C.J., Dick, H.J.B., Blum, P., Abe, N., Blackman, D.K., Bowles, J.A., Cheadle, M. J., Cho, K., Ciazela, J., Deans, J.R., Edgcomb, V.P., Ferrando, C., France, L., Ghosh, B., Ildefonse, B.M., Kendrick, M.A., Koepke, J.H., Leong, J.A.M., Liu, C., Ma, Q., Morishita, T., Morris, A., Natland, J.H., Nozaka, T., Pluempfer, O., Sanfilippo, A., Sylvan, J.B., Tivey, M.A., Tribuzio, R., Viegas, L.G.F., 2017. Expedition 360 methods 360, 1–51. <https://doi.org/10.14379/iodp.proc.360.102.2017>.
- MacLeod, C.J., Escartin, J., Banerji, D., Banks, G.J., Gleeson, M., Irving, D.H.B., Lilly, R. M., McCaig, A.M., Niu, Y., Allerton, S., Smith, D.K., 2002. Direct geological evidence for oceanic detachment faulting: the Mid-Atlantic Ridge. 15°45'N. *Geology* 30, 879. [https://doi.org/10.1130/0091-7613\(2002\)030<0879:DGEFOD>2.0.CO;2](https://doi.org/10.1130/0091-7613(2002)030<0879:DGEFOD>2.0.CO;2).
- MacLeod, C.J., Searle, R.C., Murton, B.J., Casey, J.F., Mallows, C., Unsworth, S.C., Achenbach, K.L., Harris, M., 2009. Life cycle of oceanic core complexes. *Earth Planet Sci. Lett.* 287, 333–344. <https://doi.org/10.1016/J.EPSL.2009.08.016>.
- Maierová, P., Lexa, O., Jerábek, P., Schulmann, K., Franěk, J., 2017. Computational study of deformation mechanisms and grain size evolution in granulites – implications for the rheology of the lower crust. *Earth Planet Sci. Lett.* 466, 91–102. <https://doi.org/10.1016/j.epsl.2017.03.010>.
- Mansard, N., Stünitz, H., Raimbourg, H., Précigout, J., 2020. The role of deformation-reaction interactions to localize strain in polymineralic rocks: insights from experimentally deformed plagioclase-pyroxene assemblages. *J. Struct. Geol.* 134, 104008. <https://doi.org/10.1016/J.JSG.2020.104008>.
- Marti, S., Stünitz, H., Heilbronner, R., Plümpfer, O., Kilian, R., 2018. Syn-kinematic hydration reactions, grain size reduction, and dissolution-precipitation creep in experimentally deformed plagioclase-pyroxene mixtures. *Solid Earth* 9, 985–1009. <https://doi.org/10.5194/se-9-985-2018>.
- Mauler, A., Bystricky, M., Kunze, K., Mackwell, S., 2000. Microstructures and lattice preferred orientations in experimentally deformed clinopyroxene aggregates. *J. Struct. Geol.* 22, 1633–1648. [https://doi.org/10.1016/S0191-8141\(00\)00073-0](https://doi.org/10.1016/S0191-8141(00)00073-0).
- Matsumoto, T., Dick, H.J.B., Scientific Party, Shipboard, 2002. Preliminary Report (ABCDE): Yokosuka/Shinkai 6500 YK01-14 Cruise Results. Yokosuka, Japan Marine Science and Technology Center.
- Mehl, L., Hirth, G., 2008. Plagioclase preferred orientation in layered mylonites: evaluation of flow laws for the lower crust. *J. Geophys. Res.: Solid Earth* 113, B05202. <https://doi.org/10.1029/2007JB005075>.
- Michael, P.J., Schilling, J.-G., 1989. Chlorine in mid-ocean ridge magmas: evidence for assimilation of seawater-influenced components. *Geochem. Cosmochim. Acta* 53, 3131–3143. [https://doi.org/10.1016/0016-7037\(89\)90094-X](https://doi.org/10.1016/0016-7037(89)90094-X).
- Miranda, E.A., 2006. Structural Development of the Atlantis Bank Oceanic Detachment Fault System, Southwest Indian Ridge. University of Wyoming. Ph.D. dissertation.
- Miranda, E.A., John, B.E., 2010. Strain localization along the Atlantis Bank oceanic detachment fault system, Southwest Indian Ridge. G-cubed 11. <https://doi.org/10.1029/2009GC002646>.
- Miranda, E.A., Klepeis, K.A., 2016. The interplay and effects of deformation and crystallized melt on the rheology of the lower continental crust, Fiordland, New Zealand. *J. Struct. Geol.* 93, 91–105. <https://doi.org/10.1016/j.jsg.2016.09.007>.
- Natland, J.H., Dick, H.J.B., 2001. Formation of the lower oceanic crust and the crystallization of gabbroic cumulates at a very slowly spreading ridge. *J. Volcanol. Geoth. Res.* 110, 191–233. [https://doi.org/10.1016/S0377-0273\(01\)00211-6](https://doi.org/10.1016/S0377-0273(01)00211-6).
- Okudaira, T., Jerabek, P., Stünitz, H., Fusses, F., 2015. High-temperature fracturing and subsequent grain-size-sensitive creep in lower crustal gabbros: evidence for coseismic loading followed by creep during decaying stress in the lower crust? *J. Geophys. Res.: Solid Earth* 120, 3119–3141. <https://doi.org/10.1002/2014JB011708>.
- Okudaira, T., Shigematsu, N., Harigane, Y., Yoshida, K., 2017. Grain size reduction due to fracturing and subsequent grain-size-sensitive creep in a lower crustal shear zone in the presence of a CO₂-bearing fluid. *J. Struct. Geol.* 95, 171–187. <https://doi.org/10.1016/j.jsg.2016.11.001>.
- Paterson, M.S., 1990. Superplasticity in geological materials, mat. Res. Soc. Symp. Proc. 196, 1341–1358.
- Pertsev, A.N., Aranovich, L.Y., Prokofiev, V.Y., Bortnikov, N.S., Cipriani, A., Simakin, S. S., Borisovskiy, S.E., 2015. Signatures of residual melts, magmatic and seawater-derived fluids in oceanic lower-crust gabbro from the Vema lithospheric section, Central Atlantic. *J. Petrol.* 56, 1069–1088. <https://doi.org/10.1093/petrology/egv028>.
- Pettigrew, T.L., Casey, J.F., Miller, D.J., 1999. The scientific party. In: *Proceedings of the Ocean Drilling Program. Ocean Drilling Program*, College Station, TX, p. 179. <https://doi.org/10.2973/odp.proc.ir.179>. Initial Reports.
- Philippot, P., van Roermund, H.L.M., 1992. Deformation processes in eclogitic rocks: evidence for the rheological delamination of the oceanic crust in deeper levels of subduction zones. *J. Struct. Geol.* 14, 1059–1077. [https://doi.org/10.1016/0191-8141\(92\)90036-V](https://doi.org/10.1016/0191-8141(92)90036-V).
- Platt, J.P., 2015. Rheology of two-phase systems: a microphysical and observational approach. *J. Struct. Geol.* 77, 213–227. <https://doi.org/10.1016/j.jsg.2015.05.003>.
- Ryan, W.B.F., Carbotte, S.M., Coplan, S., O'Hara, A., Melkonian, A., Arko, R., Weissel, R.A., Ferrini, V., Goodwillie, A., Nitche, F., Bonczkowski, J., Zemsky, R., 2009. Global multi-resolution topography (GMRT) synthesis data set. G-cubed 10, Q03014.
- Schroeder, T., John, B.E., 2004. Strain localization on an oceanic detachment fault system, Atlantis Massif, 30°N, Mid-Atlantic Ridge. G-cubed 5, 1–30. <https://doi.org/10.1029/2004GC000728>.
- Shipboard Scientific Party, 1989. Site 735, proc. Ocean drill. Program Initial Rep 118, 89–222. <https://doi.org/10.2973/odp.proc.ir.118.107.1989>.
- Shipboard Scientific Party, 1999a. Leg 179 summary. *Proc. Ocean Drill. Progr. Initial Rep.* 179, 1–26. <https://doi.org/10.2973/odp.proc.ir.179.101.1999>.
- Shipboard Scientific Party, 1999b. Leg 176 summary. *Proc. Ocean Drill. Progr. Initial Rep.* 176, 1–70. <https://doi.org/10.2973/odp.proc.ir.176.101.1999>.
- Skemer, P., Katayama, I., Jiang, Z., Karato, S.-I., 2005. The misorientation index: development of a new method for calculating the strength of lattice-preferred orientation. *Tectonophysics* 411, 157–167. <https://doi.org/10.1016/j.tecto.2005.08.023>.
- Smith, D.K., Cann, J.R., 1993. Building the crust at the mid-atlantic ridge. *Nature* 365, 707–715. <https://doi.org/10.1038/365707a0>.
- Smith, D.K., Cann, J.R., Escartin, J., 2006. Widespread active detachment faulting and core complex formation near 13° N on the Mid-Atlantic Ridge. *Nature* 442, 440–443. <https://doi.org/10.1038/nature04950>.
- Smith, D., 2014. Clinopyroxene precursors to amphibole sponge in arc crust. *Nat. Commun.* 5, 4329. <https://doi.org/10.1038/ncomms5329>.
- Soda, Y., Harigane, Y., Kajimoto, K., Okudaira, T., 2019. Crystallographic preferred orientations of plagioclase via grain boundary sliding in a lower-crustal anorthositic ultramylonite. *Int. J. Earth Sci.* 108, 2057–2069. <https://doi.org/10.1007/s00531-019-01749-z>.
- Spies, R., Dibona, R., Faccenda, M., Mattioli, M., Renzulli, A., 2017. Mylonitic gabbro nodules of Stromboli (southern Italy): microstructural evidence of high-temperature deformation of cumulates during the evolution of the magmatic crustal roots of an active volcano. In: Bianchini, G., Bodinier, J.-L., Braga, R., Wilson, M. (Eds.), *The Crust-Mantle and Lithosphere-Asthenosphere Boundaries: Insights from Xenoliths, Orogenic Deep Sections, and Geophysical Studies*, vol. 526. Geological Society of America Special Paper, pp. 89–105. [https://doi.org/10.1130/2017.2526\(05\)](https://doi.org/10.1130/2017.2526(05)).
- Stakes, D., Mével, C., Cannat, M., Chaput, T., 1991. Metamorphic stratigraphy of hole 735B. In: *Proceedings of the Ocean Drilling Program. Scientific Results*, pp. 153–180.
- Stuart, C.A., Piazzolo, S., Daczko, N.R., 2018. The recognition of former melt flux through high-strain zones. *J. Metamorph. Geol.* 36, 1049–1069. <https://doi.org/10.1111/jmg.12427>.
- Tucholke, B.E., Fujioka, K., Ishihara, T., Hirth, G., Kinoshita, M., 2001. Submersible study of an oceanic megamullion in the central North Atlantic. *J. Geophys. Res.: Solid Earth* 106, 16145–16161. <https://doi.org/10.1029/2001JB000373>.
- Tucholke, B.E., Lin, J., Kleinrock, M.C., 1998. Megamullions and mullion structure defining oceanic metamorphic core complexes on the Mid-Atlantic Ridge. *J. Geophys. Res.: Solid Earth* 103, 9857–9866. <https://doi.org/10.1029/98JB00167>.
- Van der Werf, T., Chatzaras, V., Marcel Kriegsman, L., Kronenberg, A., Tikoff, B., Drury, M.R., 2017. Constraints on the rheology of the lower crust in a strike-slip plate boundary: evidence from the San Quintin xenoliths, Baja California, Mexico. *Solid Earth* 8, 1211–1239. <https://doi.org/10.5194/se-8-1211-2017>.
- Viegas, G., Menegon, L., Archanjo, C., 2016. Brittle grain-size reduction of feldspar, phase mixing and strain localization in granulites at mid-crustal conditions (Pernambuco shear zone, NE Brazil). *Solid Earth* 7, 375–396. <https://doi.org/10.5194/se-7-375-2016>.
- Von Damm, K.L., Damm, V., L., K., 1990. Seafloor hydrothermal activity: black smoker chemistry and chimneys. *Ann. Rev. Earth Planet Sci.* 18, 173–204. <https://doi.org/10.1146/annurev.ea.18.050190.001133>.
- White, P., Holland, W., 2000. The effect of TiO₂ and Fe₂O₃ on metapelitic assemblages at greenschist and amphibolite facies conditions: mineral equilibria calculations in the system K₂O-FeO-MgO-Al₂O₃-SiO₂-H₂O-TiO₂-Fe₂O₃. *J. Metamorph. Geol.* 18, 497–511. <https://doi.org/10.1046/j.1525-1314.2000.00269.x>.

- White, R.W., Powell, R., Clarke, G.L., 2002. The interpretation of reaction textures in Fe-rich metapelitic granulites of the Musgrave Block, central Australia: constraints from mineral equilibria calculations in the system $K_2O-FeO-MgO-Al_2O_3-SiO_2-H_2O-TiO_2-Fe_2O_3$. *J. Metamorph. Geol.* 20, 41–55. <https://doi.org/10.1046/j.0263-4929.2001.00349.x>.
- White, R.W., Powell, R., Holland, T.J.B., 2008. Calculation of partial melting equilibria in the system $Na_2O-CaO-K_2O-FeO-MgO-Al_2O_3-SiO_2-H_2O$ (NCKFMASH). *J. Metamorph. Geol.* 19, 139–153. <https://doi.org/10.1046/j.0263-4929.2000.00303.x>.
- White, R.W., Powell, R., Johnson, T.E., 2014. The effect of Mn on mineral stability in metapelites revisited: new a-x relations for manganese-bearing minerals. *J. Metamorph. Geol.* 32, 809–828. <https://doi.org/10.1111/jmg.12095>.
- Whitney, D., Evans, B.W., 2010. Abbreviations for names of rock-forming minerals. *Am. Mineral.* 95, 185–187.

5.2 Manuscript #2: Interplay between crystal-plasticity, fracturing and dissolution-precipitation creep in lower-crustal ultramylonite from hole U1473A, Atlantis Bank, Southwest Indian Ridge

Rhander Taufner^{1*}, Gustavo Viegas¹, Claudia Trepmann²

¹Institute of Geosciences, University of Brasília, Brasília, Brazil

²Department of Earth and Environmental Sciences, Ludwig-Maximilians University, Munich, Germany

*Corresponding author (e-mail: rhander.altoe@gmail.com)

Abstract

Microfabrics of a gabbroic ultramylonitic shear zone from the Atlantis Bank oceanic core complex have been studied to investigate strain localization processes during exhumation of the lower oceanic crust through detachment faults. The ~0.5 cm wide ultramylonite band is hosted in a coarse-grained deformed gabbro. Microfabric analysis reveal undulatory extinction, kink bands, bent exsolution lamellae or twins and healed microfractures decorated by new grains within porphyroclasts of diopside and feldspar in the ultramylonite, as well as the host gabbro close to the border of the ultramylonite. These microstructures suggest that strain was initially accommodated by dislocation glide associated with microfracturing, i.e. high-stress crystal plasticity. Heterogenous fluid influx along microfractures is suggested to have led to localized phase transformation, as amphibole is abundant in the fine-grained matrix of the ultramylonite but not in the host gabbro. Fluid-rock interaction resulted in the development of the ultramylonite via grain-size sensitive fluid-assisted granular flow. Strain localization is concomitant to increasing fluid-rock interaction and the replacement of the former deformed anhydrous mineral assemblage into an hydrated ultramylonite composed of a plagioclase-amphibole mixture. Our study highlights the importance of fluid-assisted metamorphic reaction in decreasing the viscosity of the metastable lower oceanic crust and creating zones of extreme rheological weakening that deform by diffusion creep on the long term. Fluid infiltration plays a key role in facilitating ductile deformation and tectonic spreading through large-scale detachment faults in the hot, lower oceanic crust.

1. Introduction

The onset of grain-size sensitive (GSS) mechanisms following strain localization in shear zones is often a result of grain-size reduction with or without the presence of fluids. In the typically anhydrous and strong conditions that are dominant in the lower oceanic crust (Pollitz et al., 2001; Jackson, 2002; Freed and Bürgmann, 2004; Bürgmann and Dresen, 2008; Thatcher and Pollitz, 2008), grain size reduction via dynamic recrystallization in the dislocation creep regime is an important process controlling the rheology of deformed aggregates, which are generally composed by pyroxene-plagioclase mixtures (Raimbourg et al., 2008; Miranda and John, 2010). Grain size reduction and phase mixing often accompanies the evolution of shear zones, leading to a shift of deformation mechanisms, ultimately resulting in the activation of steady-state grain size sensitive creep, e.g., diffusion creep and grain boundary sliding (Mehl and Hirth, 2008). However, as the composition and structure of the lower crust are both vertically and horizontally heterogeneous (Dick et al., 2019b and references therein), a general assessment of the mechanical behavior of the crust is usually difficult to achieve. Thus, the investigation of grain-scale deformation mechanisms of the main rock-forming minerals from lower crustal shear zones is of great importance to better understand the rheological evolution at various depths (Schmid, 1983; Handy, 1989; Kohlstedt et al., 1995).

In fluid-bearing deforming environments, hydration reactions can substantially weaken the lower crust by activating reaction-softening mechanisms that result in diffusive mass-transfer, phase mixing and subsequent strain localization and weakening (White and Knipe, 1978; Carter et al., 1990; Klaper, 1990; Ingles et al., 1999; Stünitz and Tullis, 2001; Gueydan et al., 2003; Oliot et al., 2010; Hawemann et al., 2019). More specifically, the presence of a fluid phase along grain boundaries can enhance dissolution and precipitation processes, which are common deformation mechanisms in high-temperature deformed assemblages (e.g., Rutter, 1983; Imon et al., 2002; Menegon et al., 2008; Stokes et al., 2012; Wassmann and Stöckhert, 2013; Mukai et al., 2014; McAleer et al., 2017; Giuntoli et al., 2018). Because of these characteristics, metamorphic reactions and strain weakening may preferentially occur in wet parts of the lower crust, nucleating new phases, enhancing phase mixing and promoting grain size reduction, which can significantly decrease the strength of different sections of the lithosphere (e.g., Jamtveit et al., 2019).

The downward propagation of ruptures during earthquakes nucleated in the seismogenic layer into the deeper oceanic crust may develop brittle anisotropies that evolve into highly localized fluid pathways in the surrounding dry rock (e.g., Wolfe et al., 1995; Barclay et al., 2001; Jackson, 2002; Reyners et al., 2007). Since low lithostatic pressures favor the onset of brittle deformation even at relatively high temperatures (Mehl and Hirth, 2008), the infiltration of fluids along fractures may increase the importance of diffusive-mass transport and grain boundary sliding, therefore sustaining long-term viscous flow in lower crustal levels (Fitz Gerald and Stünitz, 1993; Precigout and Stünitz, 2016; Marti et al., 2018).

In spite of numerous studies focusing on these fluid-rock interactions (e.g., Etheridge et al., 1983; Austrheim, 1987; Díaz Aspiroz et al., 2007; Marsh et al., 2011; Goncalves et al., 2012; Getsinger et al., 2013; Jamtveit et al., 2016; Condit and Mahan, 2017), a comprehensive understanding of the competitive role between different deformation mechanisms and their relationships with hydration reactions during the geodynamic cycle remains debatable. In such scenarios, the structural investigation of localized high strain zones (i.e., ultramylonites), in which a positive feedback between fluid-present mineral reactions and phase mixing ultimately leads to strain localization at relatively low stresses or high strain rates, can help in addressing these major questions (e.g., Marti et al., 2018; Mansard et al., 2020). In the Atlantis Bank oceanic core complex (OCC), such conditions can be found in lower-crustal ultramylonites that nucleate on previously formed anisotropies along detachment fault zones (Macleod et al., 2017). Since the Atlantis Bank OCC is mostly composed of gabbroic rocks, which are highly reactive under changes in pressure, temperature and fluid conditions, their ultramylonitic shear zones represent a natural laboratory to investigate fluid-bearing strain localization processes during exhumation of the lower crust.

In this contribution, we present a detailed microfabric study of a gabbroic ultramylonitic shear zone (comprising over 90% of matrix grains; Passchier and Trouw, 2005) sampled from hole U1473A in the Atlantis Bank oceanic core complex to better understand the microstructural evolution and the role of fluid-assisted metamorphic reactions in lower-crustal oceanic detachment fault zones. We show that the onset of deformation in the gabbro occurred by dislocation glide coeval with microfracturing at high-temperature/high stress conditions, with subsequent fluid infiltration and channeling along a discrete and localized ultramylonitic shear zone. Our results

contribute to a better understanding of the mechanical controls that govern the strength of the lower oceanic crust in settings which deformation at wet conditions progressively weakens shear zones and possibly accounts for the accumulation of kilometer-scale tectonic transport along detachment faults (e.g., Cann et al., 1997; Tucholke et al., 1998; Blackman et al., 1998; Ranero and Reston, 1999; MacLeod et al., 2002).

2. Geologic setting

The Atlantis Bank oceanic core complex is a N-S, dome-shaped (25 km²) and wave-cut platform (~700 meters below sea level) located south east of Africa (Fig. 1a). It is bounded by the 7.5 Ma Atlantis II Transform fault to the west which uplifted and offset the two segments of the Southwest Indian Ridge (SWIR), drifting the Atlantis Bank to its actual location, at ~100 km south from the actual trace of the SWIR (Figs. 1a, b; Dick et al., 1991; Stakes et al., 1991; Matsumoto et al., 2002; Baines et al., 2008).

The Atlantis Bank exposes mainly lower crustal gabbroic rocks exhumed by continuous detachment faulting (review in Dick et al., 2019a). These gabbroic and peridotitic rocks recovered in site surveys and oceanic expeditions (e.g., Site 735B, Shipboard Scientific Party (1989, 1999a, 1999b); Site 1105A, Pettigrew et al. (1999); Site U1473A, Dick et al. (2019a)) show that flexural uplift and asymmetric faulting through moderate to high angle normal faults expose rocks that record high-temperature crystal plastic deformation under melt-present conditions, which are overprinted by brittle-ductile fabrics localized along zones of fluid-enhanced deformation at lower temperatures (e.g., Taufner et al., 2021, Gardner et al., 2020, Miranda and John, 2010, Ferrando et al., 2022). Hypersolidus fabrics and widespread crystal plastic deformation recorded in shear zones associated with detachment faults in the Atlantis Bank indicate that deformation and magma emplacement were contemporaneous during development of the core complex (Dick et al., 2019b; Miranda and John, 2010).

IODP Site U1473A is located at 32.42'S, 57.69'E and was drilled on top of Atlantis Bank during Expedition 360, in 2016, recovering ~800 meters of gabbro (Figs. 1b, c). Sampled rocks are mainly composed of olivine gabbro (76.5%), gabbro (14.6%) and oxide-rich gabbro (7.4%; oxide content >2%), cut by several slightly deformed to non-deformed felsic veins, microgabbros and minor diabase (Fig. 1d; complete rock units

description in Dick et al., 2019a). Melt extraction after compaction of the crystal pile led to grain size and modal mineral variation that defines the igneous layering (Ferrando et al., 2021), which is frequently obliterated by crystal-plastic deformation, leading to widespread grain-size reduction due to dynamic recrystallization (see MacLeod et al., 2017). The gabbroic rocks bearing Fe-Ti oxides are usually associated with shear zones, and the presence of oxides is attributed to the percolation of late-stage melts through an olivine gabbro framework (Dick et al., 2016).

Ultramylonitic shear zones are heterogeneously distributed throughout the hole section. They can be parallel to compositional boundaries, or crosscut a previous foliation. Ultramylonites are more common in the lower section of the hole (>500 mbsf), where they occur in discrete millimetric intervals, and are characterized by a fine grain size resulting in a mesoscopically dark layer within the coarse host rock (Fig. 1e).

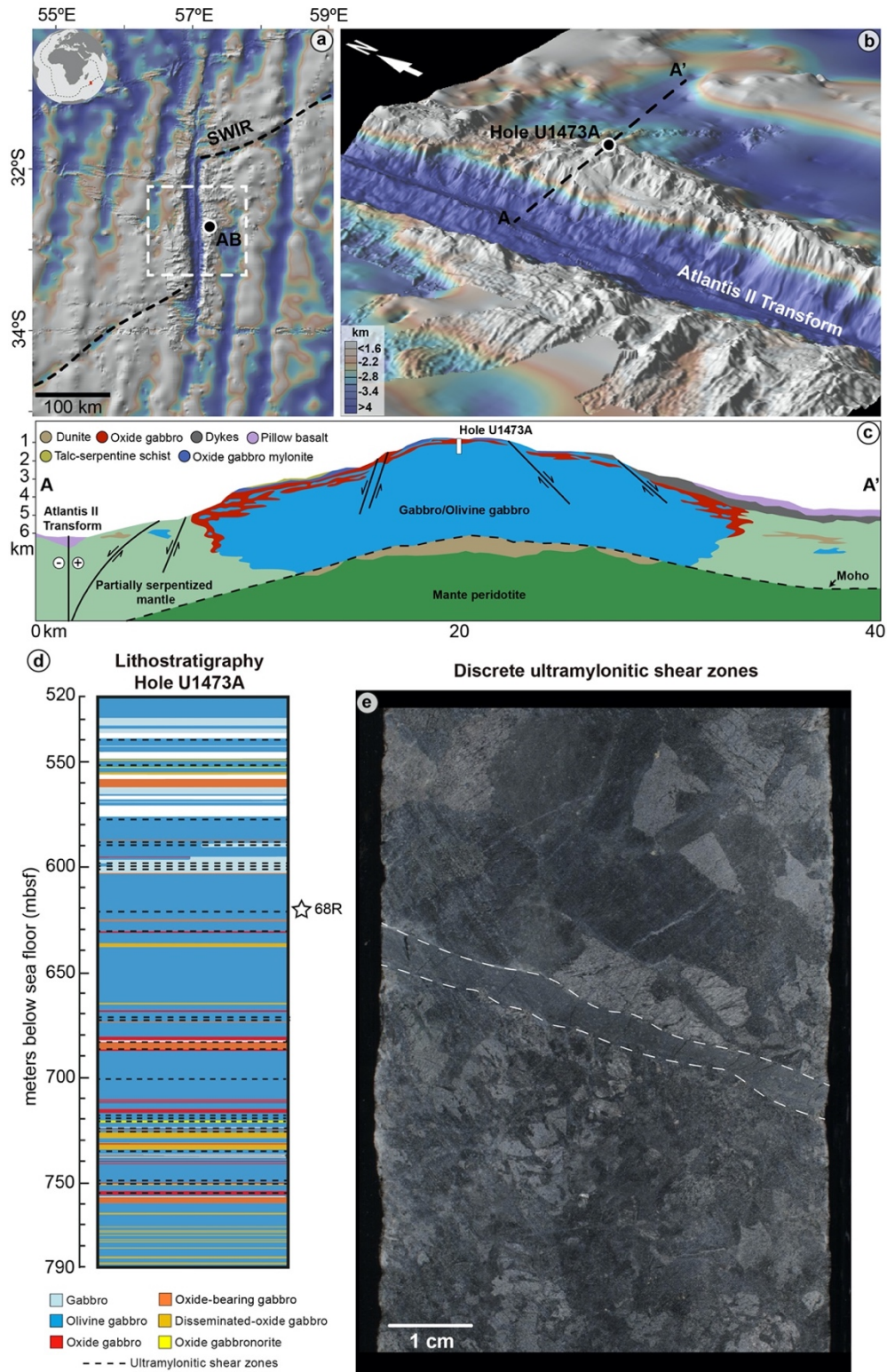


Figure 1. Geological setting of the Atlantis Bank (AB), Southwest Indian Ridge (SWIR), and shear zones sampled in this study. (a) Location of the Atlantis Bank in the Southwest Indian Ridge. (b) Location of hole U1473A at the edge of the Atlantis II Transform fault. Figures (a) and (b) made with GeoMapApp (<https://geomapapp.org>, last access January 2021; Ryan et al., 2009). (c) East-west schematic profile of Atlantis Bank based on cross-sections from Dick et al. (2019a). The morphological aspects of sea floor are derived from ODP and IODP drill cores, and the interpretation of geology at depth and the seismic-derived location of Moho are based on current knowledge (modified from Dick et al., 2019a). (d) Lower, high-temperature sector of hole U1473A showing gabbro compositions recovered in drill cores (Dick et al., 2016). Black star represents the analyzed sample location from which it was cored. Gaps in the profile relate to unrecovered intervals (Dick et al., 2016). (e) Hand sample from a representative, discrete ultramylonitic shear zone (white dashed lines) in contact with undeformed or slightly deformed olivine gabbro.

3. Methods

3.1. Sample acquisition and microstructural analysis

We analyzed an ultramylonite sample from a millimetric and discrete shear zone (sample 68R; Fig. 1e) commonly observed at the lower section of Site U1473A, which is composed of olivine gabbro deformed under high-temperature conditions before lower temperature, brittle-ductile overprinting. (Dick et al 2019a; Taufner et al., 2021). The shear zone occurs at a depth interval between 619.9 – 620.7 mbsf, and is bounded by relatively undeformed and coarse-grained olivine-gabbro (Figs. 1d, e).

For preparation of the thin section, a slab of the gabbro core was cut normal to foliation and, whenever possible, parallel to the XZ plane of the strain ellipsoid, and polished in a Buehler Minimet® 1000 grinder-polisher for 40 minutes in 1-mm diamond suspension solutions and finalized with colloidal silica solution. The deformation microstructures were analyzed under a petrographic polarized light microscope. In addition, selected backscattered electron (BSE) images were taken using a field emission scanning electron microscope (SEM, SU5000, Hitachi) equipped with NordlysNano EBSD Detector at the Department of Earth and Environmental Sciences, Ludwig-Maximilians University, Munich. An acceleration voltage of 20 kV and a working distance of 10-20 mm were applied on samples tilted at an angle of 70° from the horizontal (20° with respect to the beam).

3.2. EBSD analysis

We used EBSD-derived analyses to identify mineral phases, describe microstructures and measure the crystallographic orientation of individual phases. Grain size was calculated as the diameter of a circle of equal area and plotted as area weighted distribution. EBSD patterns were automatically measured (step size of 2µm) with the AZtec software (Oxford Technology) and noise was removed using the software CHANNEL 5 (Oxford Technology). The noise-reduced EBSD output data was processed using the MATLAB toolbox MTEX 5.5.1 (available at <https://mtex-toolbox.github.io>, last access: November 2021; Bachmann et al., 2010). Grains were detected using a threshold misorientation angle of 10° (White, 1979), and their crystallographic orientation plotted as equal area, lower hemisphere projections against the kinematic reference frame, measured in multiples of uniform distribution. The orientation distribution function (ODF) used to contour the pole figures and calculate the fabric strength was calculated using a de la Vallée Poussin kernel with

optimal halfwidth for the population of grains (one point per grain; Bachmann et al., 2011). The texture strength is defined by the J-index (J_i) and ranges from 1 (random fabric) to infinite (single crystal; Bunge, 1982).

4. Results

4.1. Sample description

The studied rock may be divided into two main domains according to grain size, mineral content and deformation structures (Fig. 2): i) a relatively coarse-grained (several tens of mm to cm in diameter) host gabbro; ii) an < 0.8 cm wide and discrete ultramylonitic shear zone characterized by a fine-grained (~6 μm) matrix in which rounded, coarser clasts (< 5 mm) are embedded.

The host gabbro is composed of plagioclase (50%), diopside (30%) and olivine (5%), with minor amounts of enstatite (10%), brown hornblende (<2%) and Fe-Ti oxides (<3%; Fig. 2). Plagioclase grains are mostly elongated with long axes of <1 cm oriented roughly 25° clockwise from the boundary of the shear zone (i.e., ultramylonite), and are internally deformed showing undulatory extinction and deformation twins (irregular and tapered twins; Fig. 2). At the boundary of plagioclase clasts, fine grains (~10-15 μm) of plagioclase are locally present. Diopside, enstatite and olivine can be fractured and show undulatory extinction. Brown amphibole is restricted to cleavage planes of diopside and enstatite.

A set of pervasive microfractures that crosscut coarse grains of plagioclase, diopside and olivine occurs directly in contact with the shear zone (Figs 2; 3a, b). Plagioclase shows a significant reduction in grain size (~11 μm) and is segregated into nearly monomineralic layers (i.e., plagioclase-rich matrix; Figs. 3c, d). Olivine grain boundaries are progressively replaced by a fine-grained mafic mixture of magnetite, enstatite and green amphibole (Figs. 3e, f). These fine-grained domains define the outer rims of the ultramylonite at the contact with the coarse host-gabbro. Fe-Ti oxide phases (ilmenite, magnetite and rutile) are common.

The thin ultramylonitic shear zone (up to ~0.8 cm wide) comprises a mafic polyphase and fine-grained matrix (~7 μm) of plagioclase, amphibole, ilmenite, magnetite and minor rutile rimming sub-spherical porphyroclasts of diopside and plagioclase (~0.4 – 5 mm in diameter) and, to a lesser extent, enstatite and rutile (Figs. 2, 4). Olivine is absent in the ultramylonite. In the polyphase matrix, the proportion of

plagioclase and amphibole is heterogeneously distributed, either forming laterally discontinuous layers with a higher proportion of plagioclase or layers with homogeneous amounts of plagioclase and amphibole (Figs. 2, 4a). This compositional banding defines an incipient foliation parallel to the boundaries of the ultramylonitic shear zone.

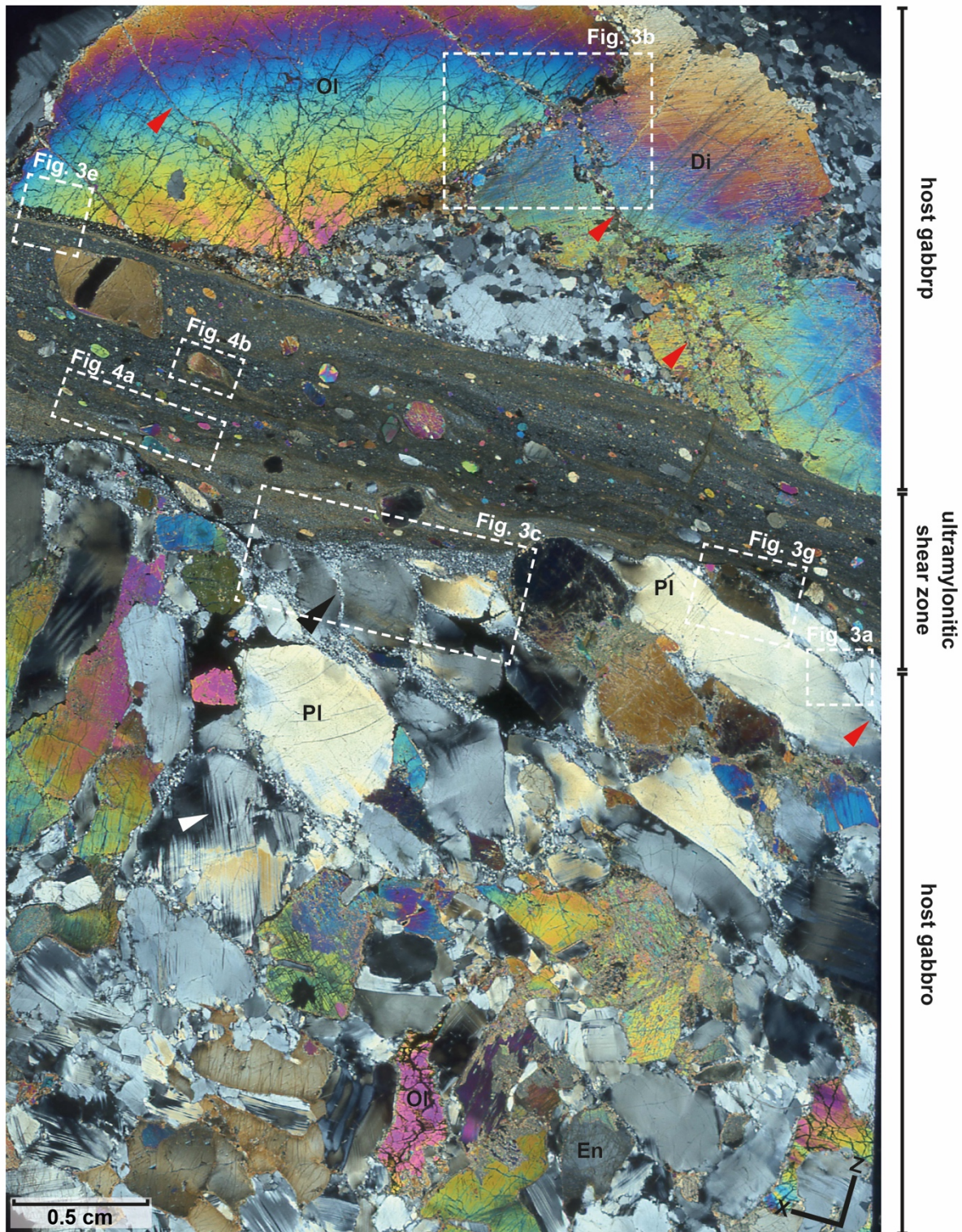


Figure 2. Thin section scan (crossed polarizers; sample 68R) showing the main microstructural domains of the ultramylonite. The host gabbro comprises deformed coarse grains of plagioclase, diopside, olivine and enstatite, which seem to be in discrete contact with a highly localized, fine-grained ultramylonitic shear zone. Locations of other figures are highlighted in dashed white box. White and red arrows indicate deformation twins in plagioclase and microfractures, respectively.

4.2. Microfabrics of the host gabbro

4.2.1. *Porphyroclasts*

Plagioclase porphyroclasts in contact with the ultramylonitic shear zone are internally deformed showing bending of the crystal lattice and low-angle grain boundaries (Figs. 3c, 4a, 5a). In addition, some grains have tapered and bent twins that do not terminate at grain boundaries (Fig. 2). Microfractures (~30-250 μm thick; Figs. 3a, 5a, b) filled with almost monomineralic fine-grained plagioclase (~3 μm -60 μm , average of ~14.9 μm ; Fig. 3h) and minor amounts of Fe-Ti oxide phases crosscut the coarse original plagioclase grains of the host gabbro. In coarse plagioclase grains, intragranular zones of fine grains with diameters ranging from 3 μm to 75 μm (~11.1 μm on average) occur, from which fractures and deformation twins emanate (Fig. 5b). Similar fine-grained plagioclase with the same size and shape (Fig. 3h) also occurs rimming the coarse plagioclase grains. The number of such fine-grains is higher close to the boundary of the shear zone, defining monomineralic plagioclase-rich layers (Figs. 2, 3c, 6a).

Coarse-grained diopside has enstatite exsolution lamellae, cleavage planes filled with amphibole, undulatory extinction, low-angle grain boundaries and new grains (Figs. 2, 3g, 7a, b). The new grains have a wide range of grain sizes (~10 μm to ~250 μm ,) and their CPO is controlled by the host: poles to (100) planes closely align normal to XY, [010] axes concentrate close to X, and poles to (001) planes are aligned near Y (Figs. 7b, c). The misorientation angle associated with low-angle grain boundaries is generally 3-5 $^\circ$, whereas the abrupt jump in misorientation angle from the coarse diopside grain to the new grains is 12-40 $^\circ$ (Fig. 7d). Microfractures seem to be related with the bending of the exsolution lamellae and cleavage planes, being oblique to the shear zone boundary (Fig. 3b). The microfractures are filled with fine grains of diopside and interstitial grains of amphibole, plagioclase, enstatite and Fe-Ti oxide phases (Fig. 8a).

Large olivine grains (diameter < 2 cm) with undulatory extinction are observed at the contact with the ultramylonite (Figs. 2, 3e). Microfractures are ubiquitous throughout the crystal, although only those fractures oriented in the same direction as in plagioclase and diopside (~20 $^\circ$ clockwise) are filled with fine grains of enstatite, amphibole and Fe-Ti oxide phases (Fig. 2, 3b). The boundary of the olivine crystal with the shear zone is irregular, with tips of the olivine crystal being dismantled and

assimilated into the shear zone (Fig. 3e). A 400 μ m thick mafic band comprising grains of magnetite, enstatite and amphibole occurs between the olivine grain and the ultramylonite (Fig. 3f).

4.2.2. Plagioclase aggregates

The fine grains of plagioclase replacing plagioclase host crystals of the gabbro have similar microstructures, whether they occur along intragranular fractures or as aggregates at the contact with the ultramylonite (i.e., plagioclase-rich layers). These grains have little internal deformation – lattice bending is observed locally with some grains reaching $\sim 6^\circ$ of misorientation at grain sizes of $\sim 11 \mu\text{m}$ to $\sim 15 \mu\text{m}$ on average - and show a weak shape preferred orientation (aspect ratio of $\sim 2 - 2.3$), with long axes oriented subparallel to the fracture direction ($\sim 25\text{-}30^\circ$ clockwise from the shear zone boundary; Figs. 5b, 6a, d). Grain boundaries are smoothly curved to straight defining triple junctions, typically decorated with Fe-Ti oxide phases that form low dihedral angles (less than $\sim 40^\circ$). Straight and continuous twins are common, locally developing bent twins. (Figs. 5a, b, 6a, d).

The CPOs of plagioclase within fractures and in the plagioclase-rich matrix have J-index ~ 6.3 and ~ 2.8 , respectively, and broadly cluster around to that of their hosts. The [100] axes are aligned at $\sim 20^\circ\text{-}30^\circ$ clockwise from the XY plane and tend to form a weak girdle parallel to the fracture direction (Figs. 5c, 6b, e). Within the microfracture, plagioclase has [010] axes and poles to (010) planes at small angles to Z, and [001] axes concentrated between Y and Z (Fig. 5c). On the other hand, plagioclase grains in the plagioclase-rich matrix have [010] axes and poles to (010) planes clustered either between XY or ZY, while poles to (001) planes are grouped at $\sim 20^\circ$ anticlockwise from Z, forming a wide girdle crosscutting the XY plane and normal to the fracture direction (Fig. 6b, e). [110] axes are more scattered between the XY plane. The misorientation angle across the coarse grains reaches values up to $\sim 6^\circ$ with abrupt jumps mostly associated with low-angle grain boundaries, whereas the jump in misorientation angle from the coarse grain to the new grains is $20^\circ\text{-}140^\circ$, which is large and abrupt (Figs. 5d, 6c, f).

4.2.3. Diopside aggregates

Fractured diopside porphyroclasts contain smaller grains along microfractures that show systematically different characteristics, which suggest that grains within

fractures include both fragments of the original host and newly-formed crystals. The fragments are distinguished from the new grains because they are generally larger (~200 μm), have cleavage planes oriented in the same direction – or slightly rotated – in relation to the coarse diopside host, with a few fragments having internal misorientation up to 10° and low-angle grain boundaries (Figs. 8a, b). Conversely, the new grains of diopside are smaller (~20 μm -170 μm , 61.5 μm on average; Fig. 3h), lack cleavage planes and exsolution lamellae and are mostly strain free – only a few grains have internal misorientations up to 6° (Fig. 8b). Also, amphibole, plagioclase and enstatite can occur within diopside microfractures. They typically form grains with low dihedral angles and thin films (<15 μm) along diopside grain boundaries (Fig. 8a). In addition, amphibole and plagioclase show embayment into diopside, and amphibole can also occur as aggregates (<80 μm) associated with Fe-Ti oxide phases. The fine grains of diopside have a strong CPO (J-index ~12.8) and mimic the orientation of the host-diopside with poles to (100) planes concentrated close or at small angles to Z; poles to (010) planes near Y, and [001] axes aligned parallel or at small angles clockwise from X (Fig. 8c).

4.2.4. Mafic layers at olivine grain boundary

In the mafic layers between the olivine grain of the host gabbro and the ultramylonite, two distinct compositional domains are observed: i) a magnetite-enstatite-rich layer and; ii) a hornblende-rich layer (Figs. 3e, 9a). Symplectitic intergrowth of magnetite and enstatite are common at the contact with the olivine crystal while pools of magnetite with low dihedral angles (<40°) are more common towards the hornblende-rich layer (Fig. 3f). Hornblende forms thin films (~3 μm) between both enstatite and enstatite-magnetite grain boundaries (Fig. 3f). Some enstatite grains have undulatory extinction, low-angle grain boundaries and grain sizes ranging from a few μm to ~300 μm with straight to sutured grain boundaries due to the presence of magnetite and hornblende (Fig. 9b). Enstatite CPO is weak (J-index ~1.4), which is characterized by maxima and submaxima of poles to (100) and (010) planes, and [001] axes; however, a faint maximum of (010) planes and [001] is observed on the XY plane and at X, respectively (Fig. 9c).

The hornblende-rich layer (40-80 μm thick) separates the magnetite-enstatite-rich layer from the ultramylonite and is mostly composed of hornblende with minor Fe-Ti oxide phases (Fig. 9a). Hornblende has a grain size from ~4 to ~21 μm , long axis

parallel to the shear zone boundary (aspect ratio ~ 2.3) with straight to curved grain boundaries and little internal deformation (Fig. 9b). In addition, it shows a clear CPO and moderate strength (J-index ~ 2.6) with poles to (100) planes near Z, forming a weak girdle normal to the XY plane (Fig. 9c). [010] and [001] axes form point maxima between Y and X, with a weak girdle on the XY plane; [001] axes have a higher intensity concentrated close to X (Fig. 9c).

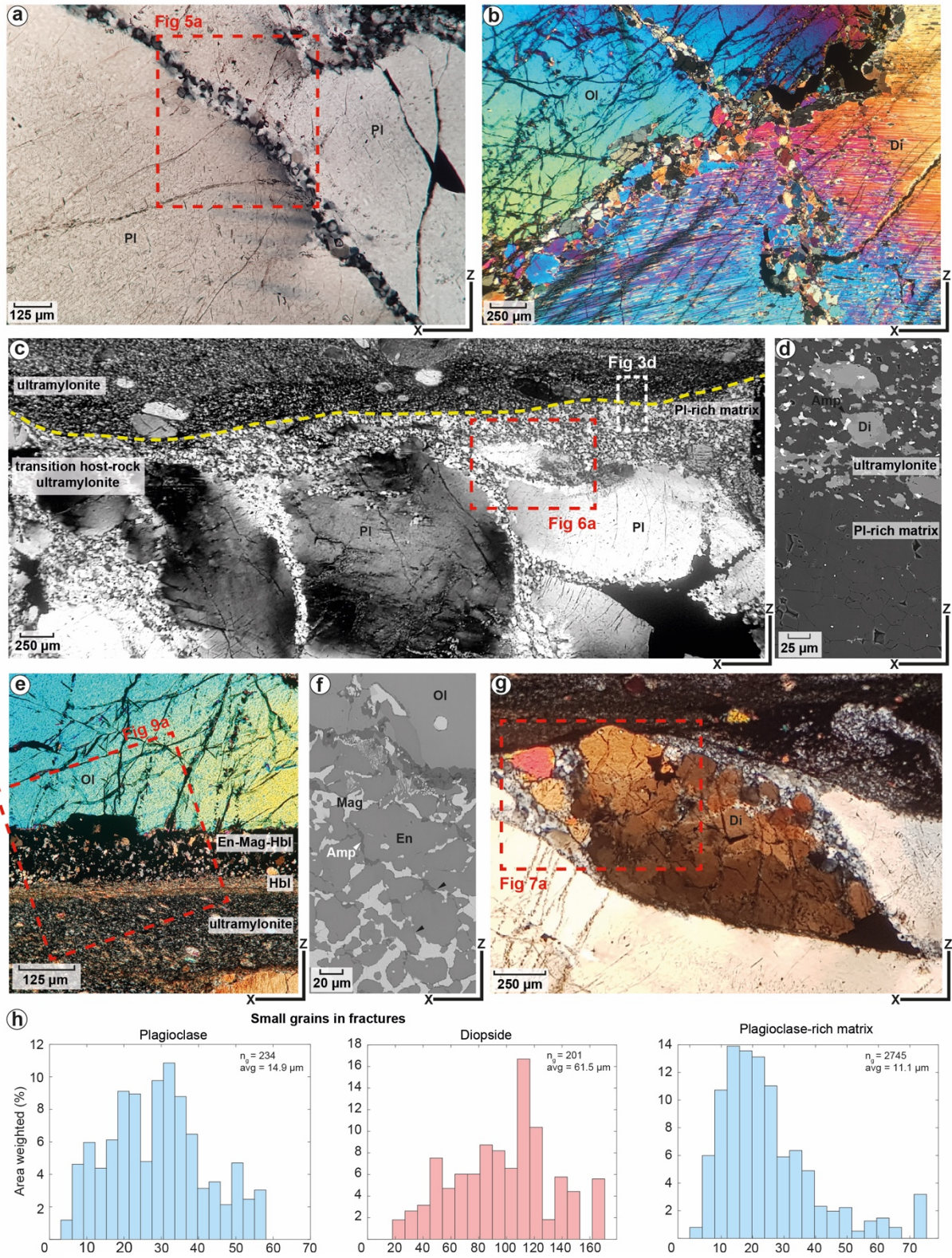


Figure 3. Microstructures (a-f) and grain-size histograms (h) from the host gabbro at the border with the ultramylonite. Red boxes indicate EBSD mapped areas. **(a, b)** Microfractures in coarse grains of plagioclase and diopside, respectively. **(c)** Fine-grained monomineralic plagioclase layer at the contact between plagioclase porphyroclast with the shear zone and along intragranular cracks. **(d)** Close-up of area marked by white dashed line in (c) showing polymineralic aggregates of the ultramylonite in contact with the monomineralic plagioclase layer. **(e)** A large grain of olivine with a layer of enstatite and magnetite (\pm amphibole), and amphibole in contact with the ultramylonite. **(f)** Close-up of the microstructures in the enstatite and magnetite layer; black and white arrows indicate low-dihedral angles of magnetite and thin films of amphibole, respectively. **(g)** Deformed coarse-grained diopside. **(h)** Grain-size histograms of plagioclase and diopside

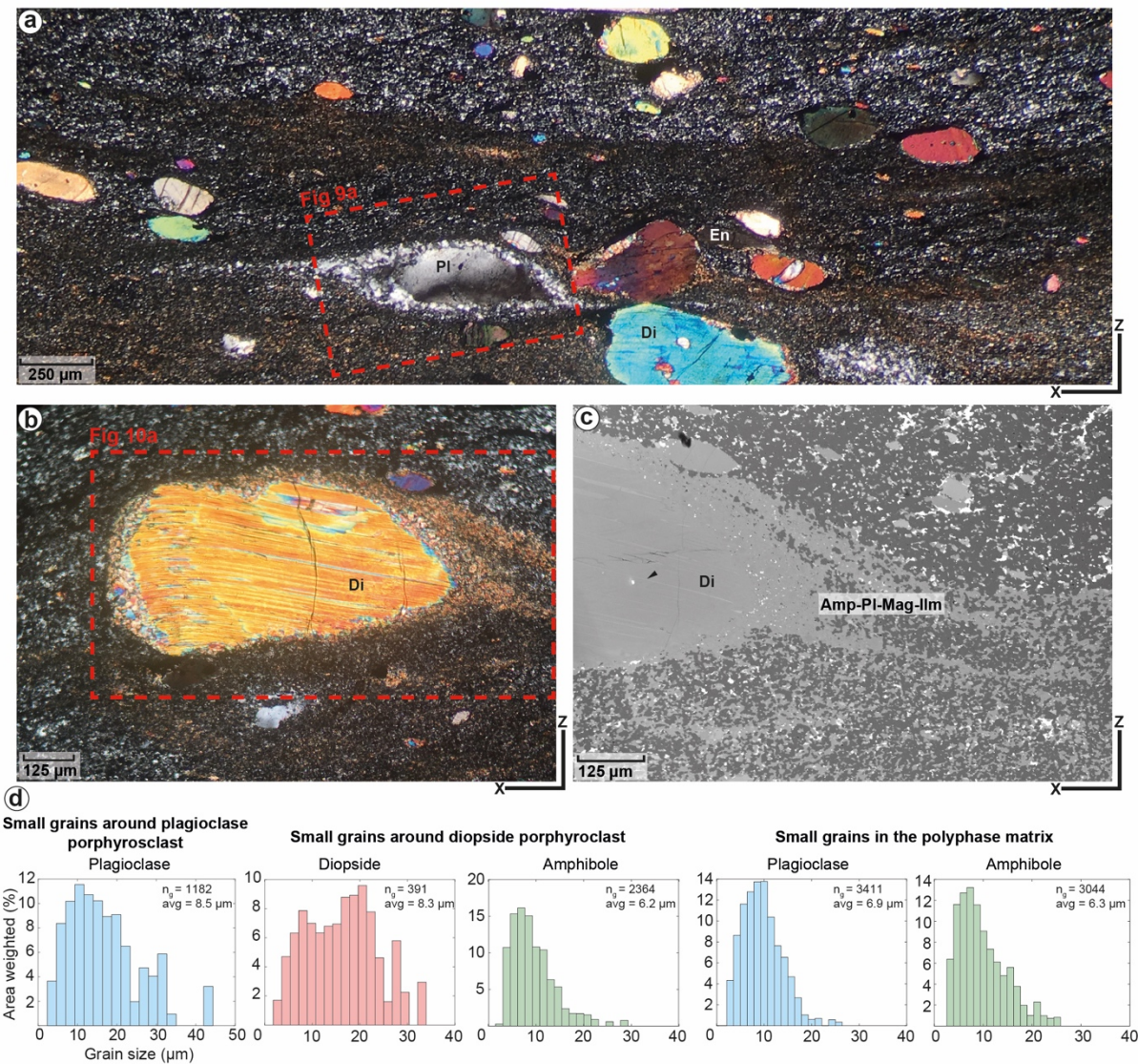


Figure 4. Microstructures (a-c) and grain-size histograms (d) from the ultramylonitic shear zone. Red boxes indicate EBSD mapped areas. (a, b) Porphyroclast (relic grain) of plagioclase and diopside, respectively, showing an asymmetric tail of new grains in a polyphase matrix of plagioclase, amphibole and Fe-oxide phases. (c) Close-up (BSE image from an area inside the red-dashed box in Fig. 4b) of the asymmetric tail from the host diopside. Note that the amphibole layer surrounding the diopside is grading into the polyphase plagioclase-rich matrix. (d) Grain-size histograms of plagioclase, diopside and amphibole rimming the hosts, and in the polyphase

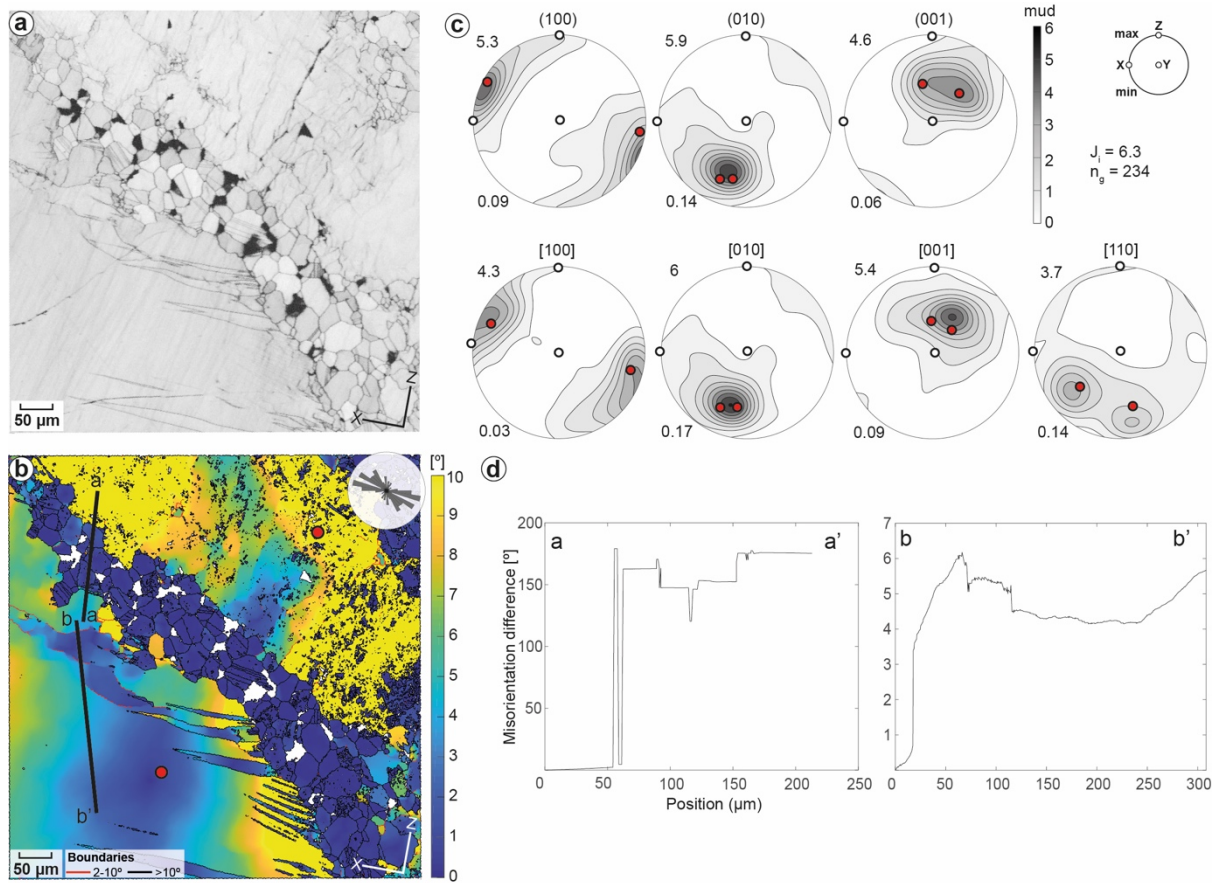


Figure 5. EBSD data of plagioclase of the host gabbro at the boundary with the ultramylonite that shows intragranular fine-grained aggregates along high-strain zones probably reflecting former microfractures. **(a, b)** Band contrast and intragrain misorientation [mis2mean] maps of plagioclase, respectively. Black (a) and white (b) areas are, respectively, non-indexed areas due to heterogeneous mechanical polishing during sample preparation. **(c)** Pole figures showing the crystallographic orientation of new grains of plagioclase within the former microfracture and in the host grain (red dots). **(d)** Misorientation angle profiles from profile lines shown in map (b).

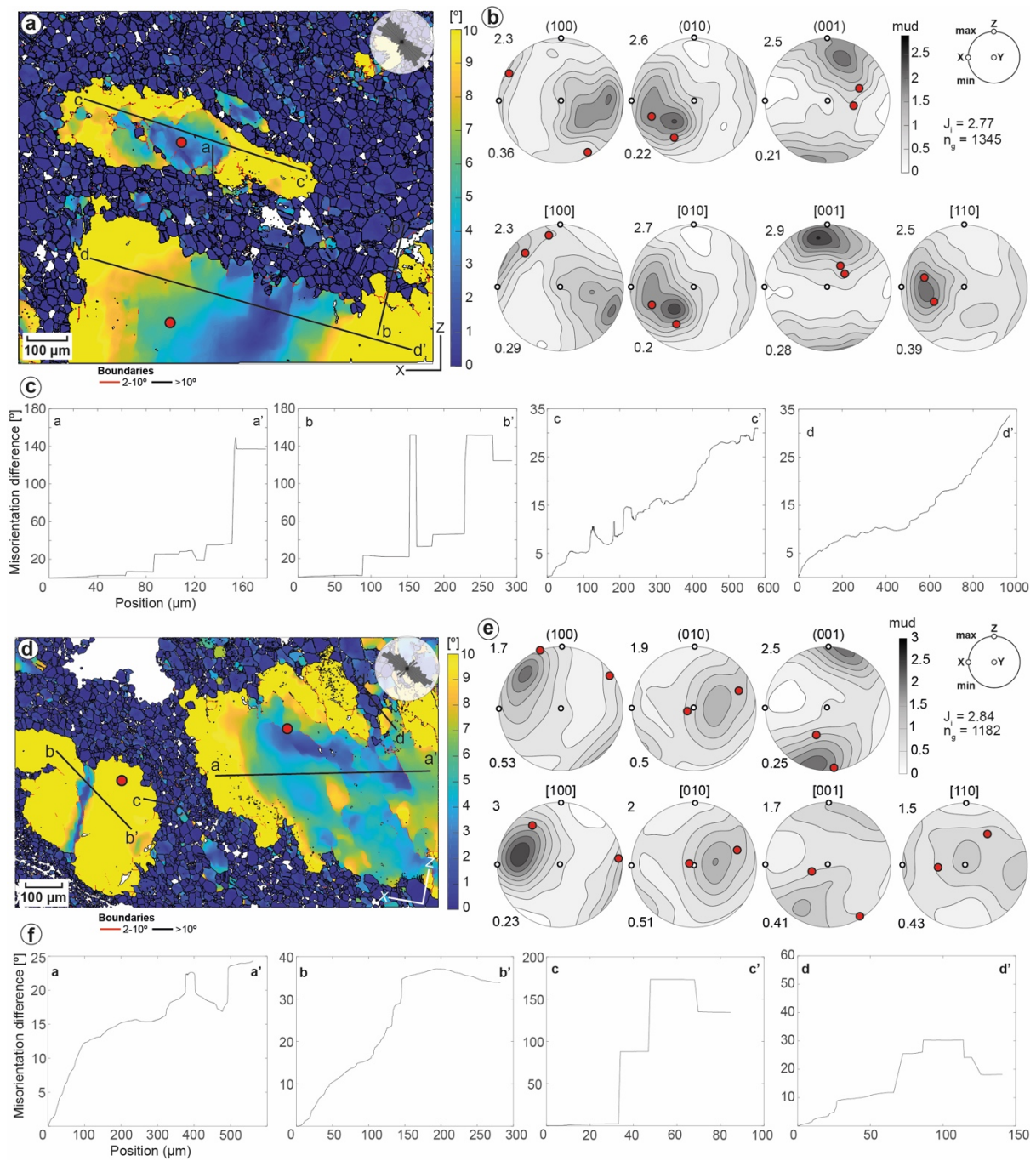


Figure 6. EBSD data of plagioclase from the host gabbro at the contact with the ultramylonite. **(a, d)** Intragrain misorientation [mis2mean] maps. **(b, e)** Pole figures showing the crystallographic orientation of new grains of plagioclase in the plagioclase-rich matrix. Red dots represent the orientation of the hosts. **(c, f)** Misorientation angle profiles from profile lines shown in maps (a, d).

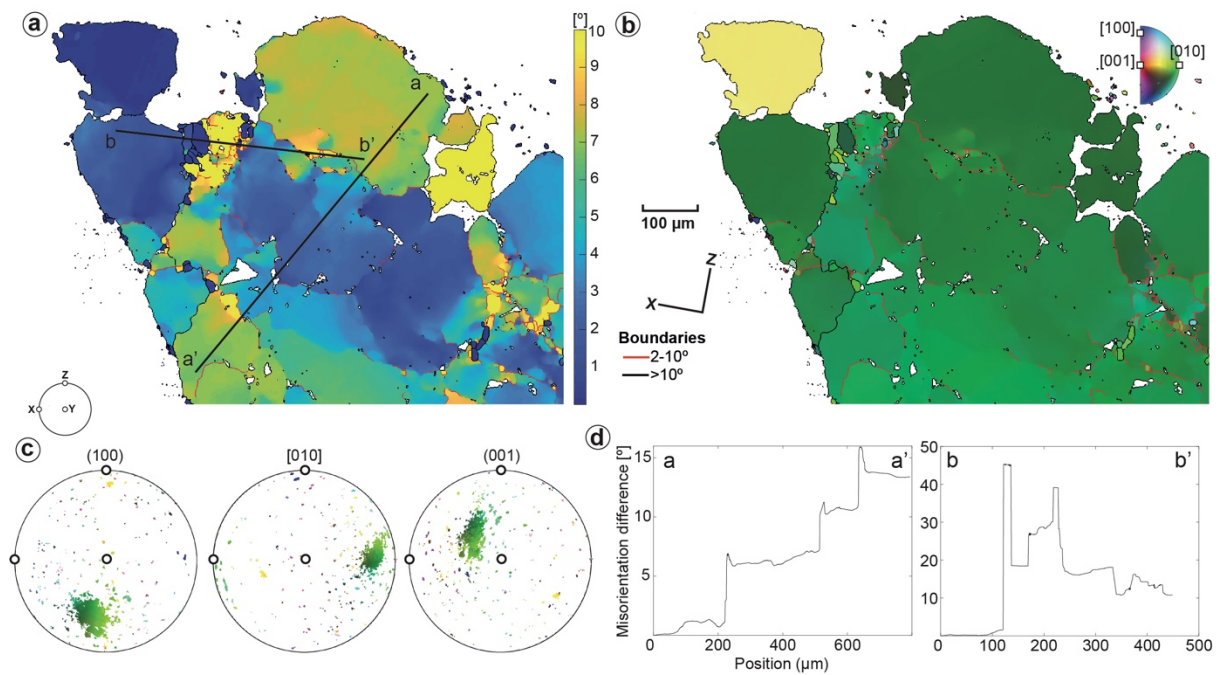


Figure 7. EBSD data of diopside from the host gabbro at the boundary with the ultramylonite. **(a, b)** Maps of intragrain misorientation [mis2mean] and color coding after inverse pole figure ($\parallel X$), respectively. **(c)** Pole figures showing the orientation of new grains and host; color coding corresponds to map in (b). **(d)** Misorientation angle profiles from profile lines shown in map (a).

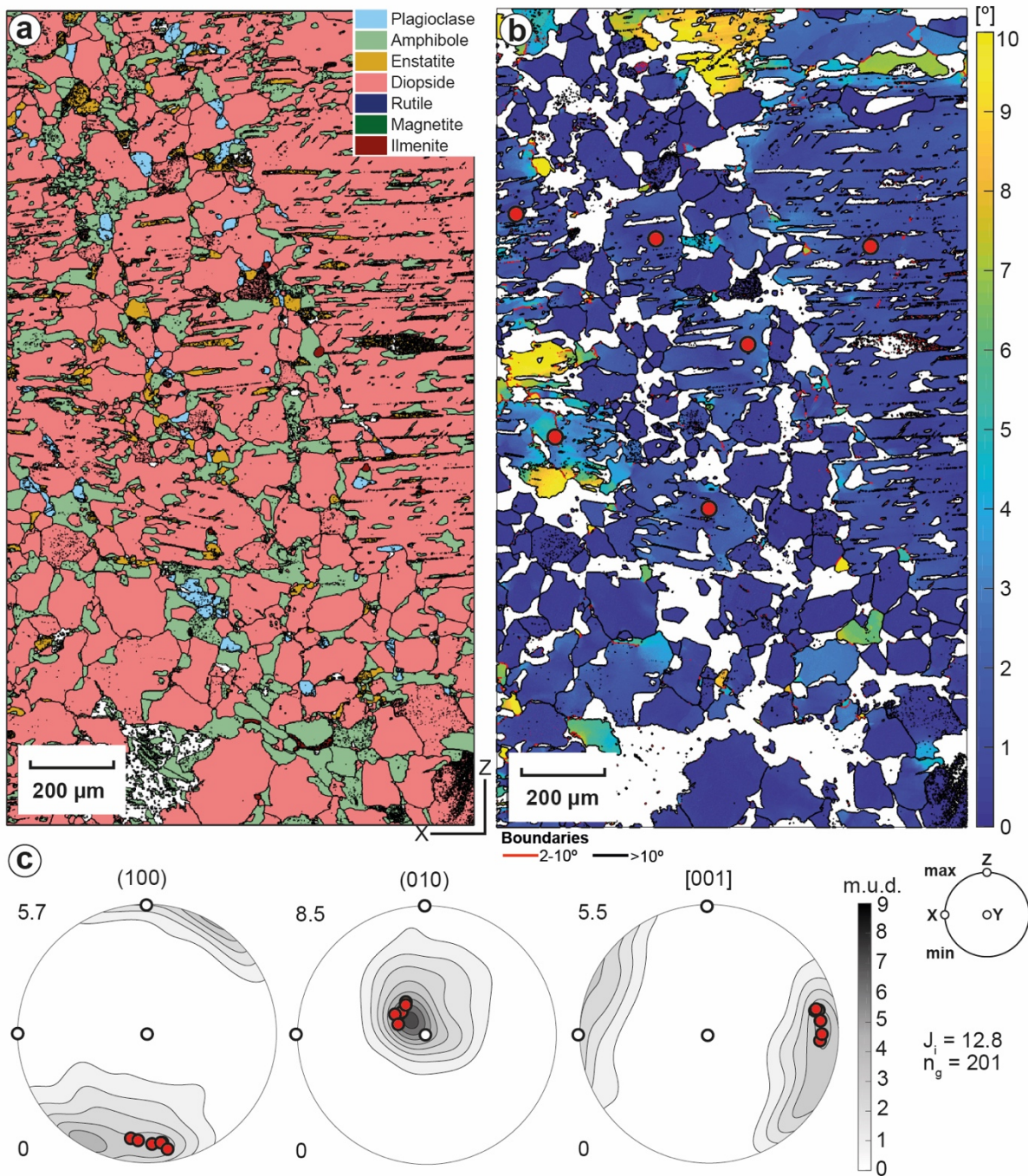


Figure 8. EBSD data of diopside porphyroclast in the host gabbro at the contact with the ultramylonite that contains polyphase aggregates of plagioclase, amphibole and diopside along former microfractures. **(a, b)** Maps of phase and intragrain misorientation [mis2mean] of diopside, respectively. Fragments of the host in the microfracture and the host are identified by the red dots. **(c)** Pole figures showing the crystallographic orientation of new grains of diopside within the microfracture. Red dots represent the orientation of the host and fragments in the microfracture.

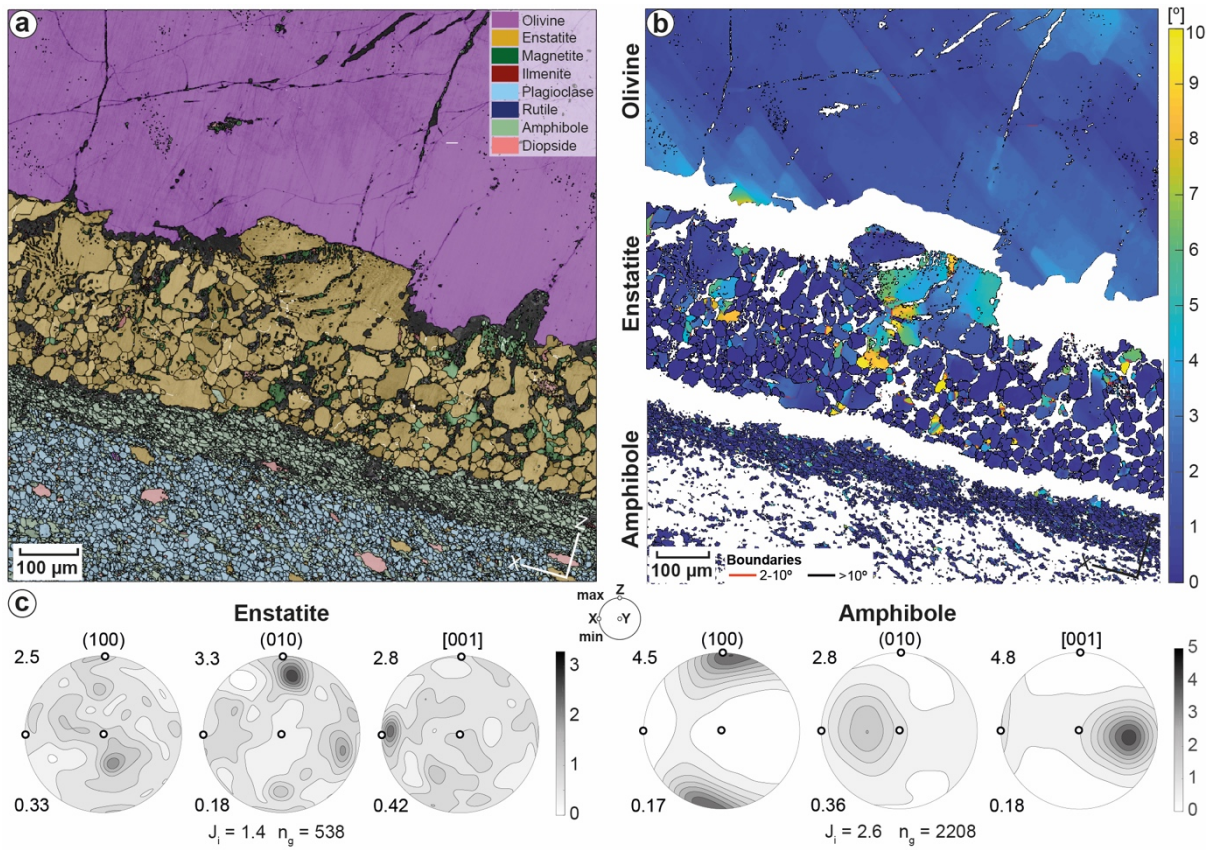


Figure 9. EBSD data of olivine from the host gabbro at the contact with the ultramylonite. **(a, b)** Maps of phase and intragrain misorientation [mis2mean], respectively, highlighting olivine, enstatite and amphibole (hornblende). **(c)** Pole figures showing the crystallographic orientation of enstatite and amphibole in the layer of magnetite-enstatite and amphibole, respectively.

4.3. Microfabrics of the ultramylonite

4.3.1. Porphyroclasts

The ultramylonitic shear zone is characterized by the alignment of mm-scale elongated porphyroclasts of plagioclase and diopside – with minor amounts of enstatite and locally rutile - embedded in a polyphasic matrix of amphibole and plagioclase with varying amounts of Fe-Ti oxide phases and apatite (Fig. 2). Olivine does not occur in the ultramylonite. Porphyroclasts are elongated more or less parallel to the shear zone boundary, typically associated with asymmetric tails of fine grains of plagioclase -rimming plagioclase porphyroclasts -, and diopside and amphibole -rimming diopside porphyroclasts (Fig. 4).

Plagioclase porphyroclasts have irregular boundaries and show undulatory extinction and low-angle grain boundaries concentrated at grain edges (Figs. 4a, 10a, b). A few tapered twins are observed close to the grain edge; however, the grains are mostly untwinned (Figs. 10a, b). Fine grains of plagioclase (~3µm to 45µm, average ~8.5µm; Fig. 4d) occur rimming the porphyroclasts, locally forming monomineralic asymmetric tails that disappear away from the host and end up forming a matrix of plagioclase, amphibole and Fe-Ti oxides (Figs. 4a, 10a).

Diopside porphyroclasts show undulatory extinction and kink bands reflected by bent cleavage planes and enstatite exsolution lamellae, where enstatite can locally be replaced by amphibole (Figs. 4b, c, 11a, b). The cleavage planes are up to ~20µm thick and usually parallel to the long axes of the porphyroclasts, i.e., parallel to the mylonitic foliation, resulting in highly elongated grains with their long axes reaching up to ~300µm. Low-angle grain boundaries are observed parallel to the cleavage planes and exsolution lamellae (Fig. 11b). In the cleavage planes, amphibole is internally deformed, locally developing rounded and small grains (~10µm; Fig. 12a, b). Amphibole cleavage planes have a clear crystallographic relationship with the host diopside: poles to (100) planes concentrate close to Z, [010] axes align near Y, and [001] axes are parallel to X (Fig. 12c). Rimming the host diopside, fine grains of diopside (~3µm-75µm) are mixed with amphibole, locally forming asymmetric tails (Figs. 4b, c, 11a) which disappear with increasing distance from the host, resulting in a mixture of plagioclase, amphibole and Fe-oxides.

Small fragments of diopside, enstatite and rutile (up to $\sim 200\mu\text{m}$) are preserved in the matrix of the ultramylonitic shear zone. They are usually strain free and have irregular boundaries. Diopside and enstatite are flattened with their long axes parallel to the mylonitic foliation and are commonly associated with amphibole and, to a minor extent, Fe-Ti oxide phases.

4.3.2. *Fine grains rimming the porphyroclasts*

4.3.2.1. Plagioclase

The fine grains of plagioclase ($\sim 3\mu\text{m}$ - $45\mu\text{m}$, $8.5\mu\text{m}$ on average; Fig. 4d) are mostly strain free, have straight to smoothly curved grain boundaries with triple and locally four grain junctions, and straight twins (Figs. 4a, 10a, b). Low-angle grain boundaries occur locally and seem to be present in grains larger than $\sim 20\mu\text{m}$. Away from the host, plagioclase is mixed with amphibole and Fe-Ti oxide phases forming the polyphase matrix (Figs. 4a, 10a). The CPO of the new grains is moderate (J-index ~ 2.85) and they mimic the orientation of the host plagioclase (Fig. 10c). Poles to (100) planes and [100] axes have point maxima close to X or at an angle between X and Y, respectively. (010) planes align on the XY plane while [001] axes are distributed oblique to the XY and ZY plane. [110] axes are randomly distributed with a tendency to form point submaxima (Fig. 10c). The jump in misorientation angle across plagioclase porphyroclast is generally large and gradual (up to 45°) while the subgrains have abrupt jumps of ~ 3 - 7° (Fig. 10d). From the host to the fine grains, the misorientation angle is ~ 20 - 150° , which is large and abrupt; the high angles likely represent the twin boundaries.

4.3.2.2. Diopside

The fine diopside grains on either side of the host may be divided into two subsets based on differently oriented CPOs, grain size and grain shape (Figs. 11a, b). On the left part of the host diopside, a highly misoriented kink band ($>10^\circ$) is observed from where fine grains of diopside (subset₁) occur (Fig. 11b). These new diopside grains have grain sizes spanning from $\sim 10\mu\text{m}$ to $75\mu\text{m}$, elongated shape accompanying the orientation of the cleavage planes at the edge of the host, and are mostly strain free, although a few grains show undulatory extinction and low-angle grain boundaries (Fig. 11b). Grain boundaries are straight to curved due to fine-

grained amphibole filling interstices between diopside grains. The misorientation map shows high angles (120°-150°) of misorientation between the host diopside and the adjacent new diopside grains immediately in contact with the host, which are associated with misorientation axis between [001] and [100] axes (Fig. 11c). The CPO of diopside in subset₁ is different than that of the host, showing poles to (100) planes between X and Y, poles to (010) planes scattered, and a clustering of [001] axes at small angles to Z (Fig. 11d).

On the right side of the investigated diopside porphyroclast, fine diopside grains detach from the host forming a sigmoid tail mixed with amphibole (subset₂; Figs. 4b, c, 11a). Away from the host, diopside mix with amphibole and plagioclase. Diopside grains in subset₂ have grain size spanning from ~3µm-35µm (average ~8.3µm, Fig. 4d), are mostly strain free, and often show irregular grain boundaries due to embayment of amphibole into them (Figs. 11a, b). Their CPO is rather weak (J-index ~1.3), which is characterized by point submaxima of poles to (100) planes, and a faint tendency for alignment of [010] axes close to Y and of [001] axes near X (Fig. 11d). The misorientation profile shows an overall gradual increase in misorientation angle within the host with jumps of ~3° associated with low-angle grain boundaries, while the misorientation angle between host and new grains is 20°-70°, which is large and abrupt (Fig. 11e).

4.3.2.3. Amphibole

Amphibole develops layers of almost completely strain-free small aggregates (~3-30µm, ~6.2µm on average; Fig. 4d) mixed with new diopside grains (subset₂) rimming the host diopside forming the asymmetric tail. The small grains of amphibole have long axes (aspect ratio ~1.9) oriented at ~20° clockwise from the foliation (Fig. 12a). Close to the host, the layers of amphibole are slightly deflected and become more horizontal with increasing distance from the porphyroclast, forming a polyphase mixture of amphibole, plagioclase and minor Fe-Ti oxides - which defines the polyphase matrix of the ultramylonite (Fig. 4c). Amphibole CPO is strong (J-index ~ 4.7) and follows the shape of the long axes of the grains: a maximum of poles to (100) planes at ~20° clockwise from Z, poles to (010) planes close to Y, and a clustering of [001] axes at ~20° from X, in the direction of the long axes (Fig. 12d). No

crystallographic relationship is observed between diopside grains in subset₂ and amphibole.

4.3.3. ***Polyphase matrix***

Plagioclase and amphibole have grain sizes ranging from ~3 μ m-25 μ m, averaging 6.9 μ m and 6.3 μ m, respectively (Fig. 4d). Phase boundaries are mostly curved with frequent four grain junctions, and the majority of the grains lack systematic internal deformation (Figs. 13a, b, c). Fine-grained Fe-Ti oxide phases (magnetite, ilmenite and minor rutile; up to ~15 μ m in size) occur intermixed with plagioclase and amphibole (Fig. 13a). Plagioclase is preferentially oriented (aspect ratio ~1.6) at small angles from the foliation with some scattering of the long axes at small angles from the foliation, while amphibole has a clear shape preferred orientation (aspect ratio ~1.9) at a small angle from the foliation (Figs. 13b, c). The crystallographic orientation of plagioclase is random and weak (J-index ~1.21; Fig. 13). Amphibole has a moderate (J-index ~2.91) and clear CPO, with poles to (100) planes close to Z, poles to (010) planes between X and Y, and distribution of the [001] axes at small angles between X and Y, with a tendency to cluster closer to X (Fig. 13d).

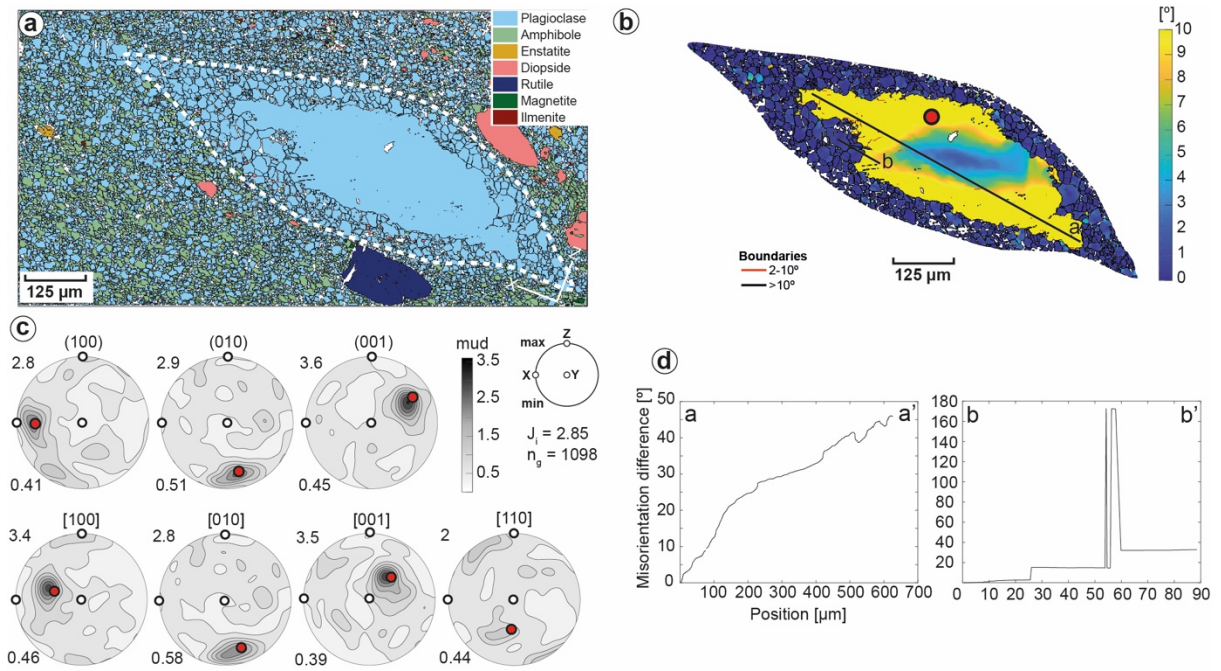


Figure 10. EBSD data of plagioclase porphyroclast from the ultramylonitic shear zone. **(a, b)** Maps of phase and intragrain misorientation [mis2mean], respectively. **(c)** Pole figures showing the ODF of new grains rimming plagioclase porphyroclast. Red dots represent the orientation of the host. **(d)** Misorientation angle profiles from profile lines shown in map (b).

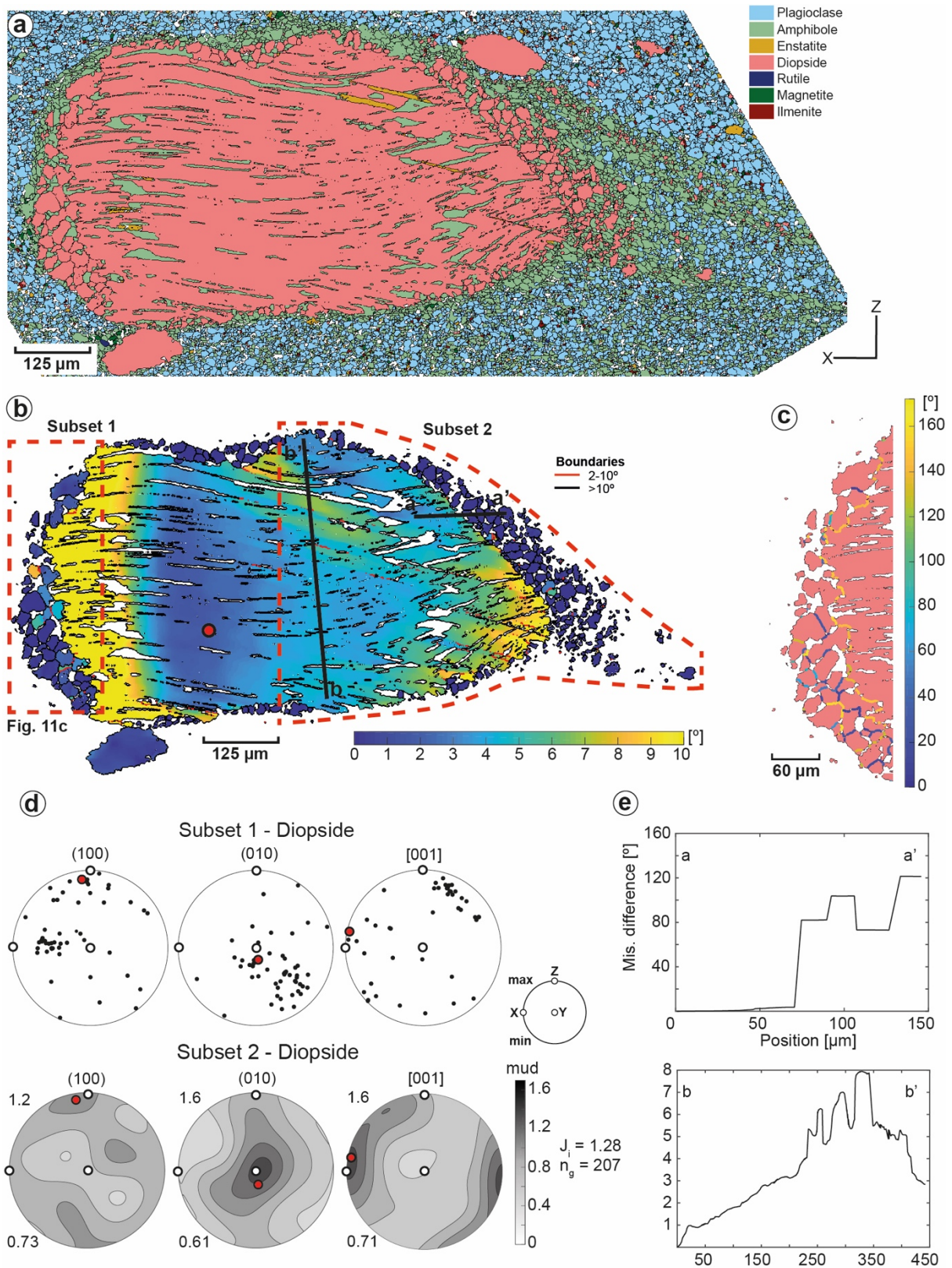


Figure 11. EBSD data of diopside porphyroclast from the ultramylonitic shear zone. **(a, b)** Maps of phase and intragrain misorientation [mis2mean], respectively. **(c)** Map of misorientation angle from subset₁ in (b). **(d)** Pole figures showing the crystallographic orientation and ODF of new grains in subset₁ and subset₂, respectively. Red dots represent the orientation of the host. **(e)** Misorientation angle profiles from profile lines shown in map (b).

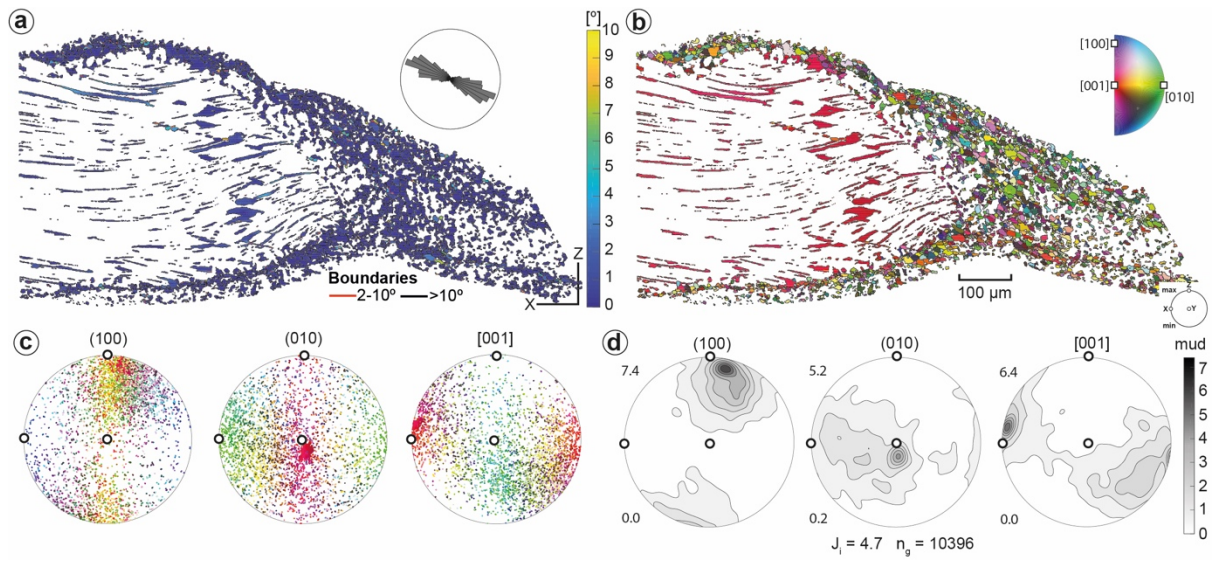


Figure 12. EBSD data of amphibole associated with diopside porphyroclast from the ultramylonitic shear zone. **(a, b)** Maps of intragrain misorientation [mis2mean] and color coding after inverse pole figure ($\parallel X$), respectively. Upper-right diagram in (a) shows shape-preferred orientation of amphibole. **(c)** Pole figures showing the orientation of amphibole; color coding corresponds to map in (b). **(d)** Pole figures showing the CPO of amphibole rimming diopside porphyroclast and

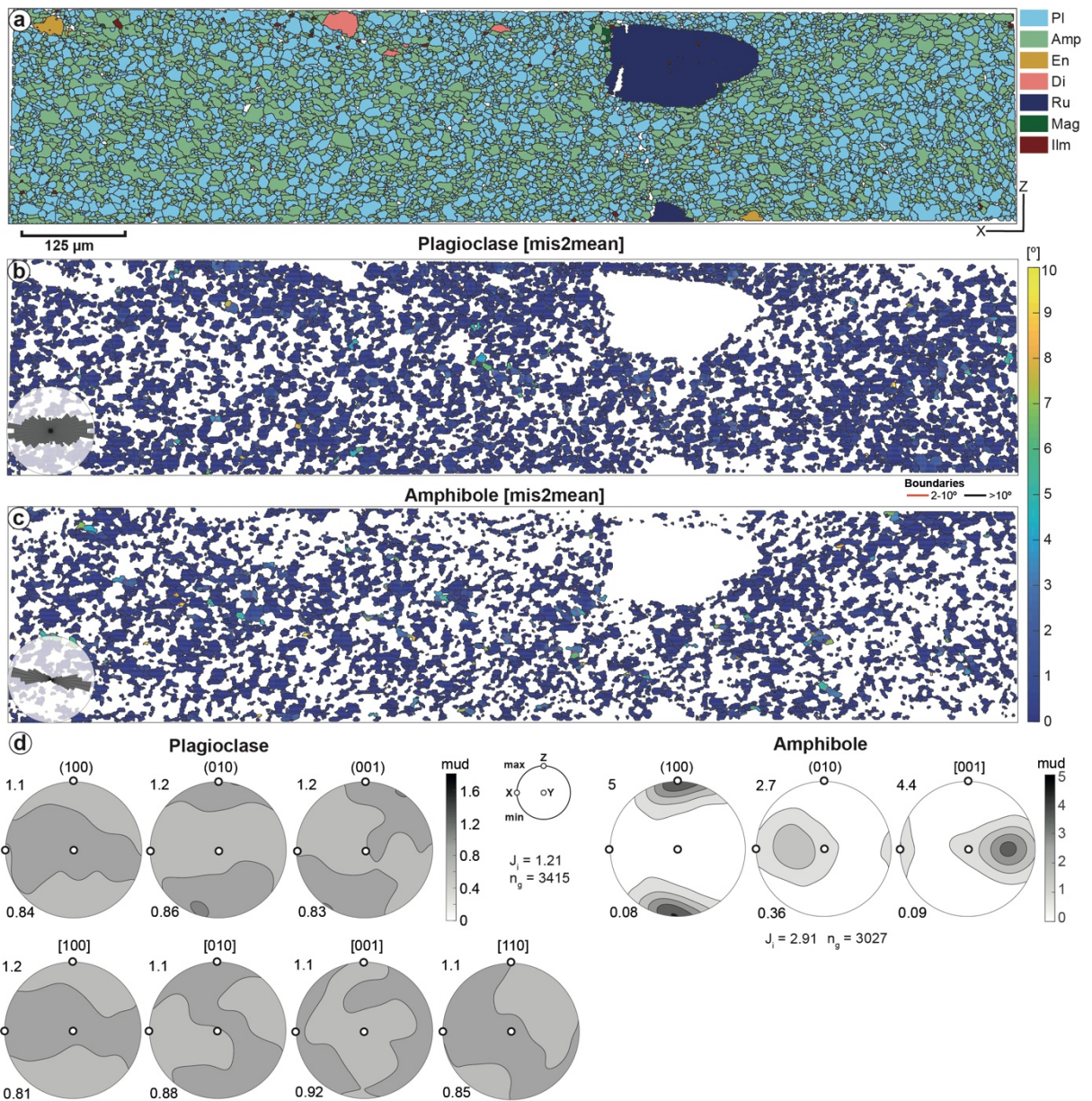


Figure 13. EBSD data of plagioclase and amphibole in the matrix of the ultramylonitic shear zone. **(a, b, c)** Maps of phase and intragrain misorientation [mis2mean] for plagioclase and amphibole, respectively. Lower-left diagrams show shape-preferred orientation of plagioclase and amphibole long axes. **(d)** Pole figures showing the CPO of plagioclase and amphibole.

5. Discussion

5.1. Deformation mechanisms in the host gabbro at the border with the ultramylonite

Diopside grains have bent cleavages, kink bands, undulatory extinction representing internal misorientation, and low-angle grain boundaries associated with few new grains (Figs. 2b, 3 b, g, 7, 8), which suggest coupled fracturing and dislocation glide with restricted dislocation climb. Dynamic recrystallization of diopside (dislocation glide and climb) is mostly observed in nature and experiments to occur at high stress and temperature conditions higher than 500 °C with dislocation glide at the [001] or [010] directions (e.g., Ingrin et al., 1991; Raterron et al., 1994; Piepenbreier and Stöckhert, 2001; Dimanov and Dresen, 2005; Orzol et al., 2003; Zhang et al., 2006; Raimbrough et al., 2008; Moghadam et al., 2010). However, subgrains and recrystallized grains in diopside porphyroclasts are scarce, suggesting that dynamic recrystallization was not the dominating process during deformation. Instead, dislocation glide, kinking and microfracturing are the main deformation mechanisms recorded by diopside porphyroclasts, indicating low-temperature plasticity or high-stress crystal plasticity, where the stress-temperature conditions during deformation restrict the activity of dislocation climb, as commonly observed in pyroxene aggregates deformed in nature and laboratory (e.g., Green and Radcliffe, 1972; Skrotzki et al., 1990; Skemer and Karato, 2008; Moghadam et al., 2010).

Fragments of the host diopside with exsolution lamellae, and new grains without exsolution lamellae along former microfractures associated with amphibole suggest deformation by cataclasis and subsequent mineral reactions. Grain size reduction by cataclasis has been invoked to explain large grain-size ranges observed in deformed rocks (e.g., Sammis et al., 1986; Keulen et al., 2007), unless nucleation and growth takes place after grain comminution (e.g., Okudaira et al., 2015, Viegas et al., 2016), which obliterates the former brittle microstructures of the grains (e.g., Bos and Spiers, 2001). The broad grain-size range of diopside along former fractures cutting diopside porphyroclasts, lack of widespread intracrystalline deformation microstructures and cleavage planes in the secondary diopside grains (Figs. 8a, b), and a host-control crystallographic relationship (Fig. 8c) suggest that the secondary grains formed due to nucleation and growth from fractured fragments (Fig. 8b, c; e.g., Stünitz et al., 2003; Trepmann et al., 2007; Menegon et al., 2013). The fact that

diopside fragments in the microfractures are not rotated with respect to the host crystal - as indicated by similar orientation of cleavage planes in diopside fragments and in the host (Fig. 8a) -, imply minor shear offset and may explain the host-control CPO of the new diopside grains, as epitaxial growth is not observed (e.g., Menegon et al., 2008). Similar microstructures are observed in experimentally fractured rocks deformed by dynamic fracturing under high-strain rate conditions (e.g., Aben et al., 2016). The presence of interstitial amphibole that often truncates diopside grains, along with plagioclase and Fe-Ti oxides (Fig. 8), suggests that microfracturing was followed or accompanied by infiltration of fluids that assisted in dissolution-precipitation processes (Putnis and Austrheim, 2010).

Plagioclase porphyroclasts show elongated grains, undulose extinction, low-angle grain boundaries, mechanical twins, and little evidence of subgrains (Figs. 2, 3c, 5, 6a, d.), also suggesting deformation in the low-temperature or high-stress plasticity regime during dislocation glide. As dislocation climb is ineffective at high-stress conditions, build-up of dislocations can lead to strain hardening and nucleation of microfractures (e.g., Drury, 1993; White, 1996). Indeed, new grains localized along former microfractures and at the border with the ultramylonite are thus restricted to zones of local high strain (Figs. 3c, 6). These new grains are often strain free, have straight twins, narrow grain size range, and a SPO oblique to the shear zone (i.e., parallel to the microfractures and long axis of the porphyroclasts). In addition, both new plagioclase grains in the plagioclase-rich layer at the border of the ultramylonite and in the microfractures have similar crystallographic orientation to that of their hosts, with alignment of poles to (001) and (010) planes close to Z and [100] axes near X, respectively (Figs. 5c, 6b, e). If this CPO was due to dislocation creep, it would point to activation of the (001)[100] and (010)[100] glide systems associated with dislocation climb and recovery (Cannat, 1991; Mehl and Hirth, 2008; Allard et al., 2021; Taufner et al., 2021). However, we do not observe subgrains in plagioclase porphyroclasts that suggest progressive rotation of subgrains in the dislocation creep regime. Furthermore, misorientation profiles lack a progressive rotation of new grains away from the orientation of their host porphyroclasts (Figs. 5d, 6c, f). Therefore, although an influence of dislocation glide on the deformation of plagioclase is likely, the observed CPO is interpreted to be inherited from the host crystal and cannot be taken as an indicative of a glide system. Since effective dynamic recovery of feldspar is

generally difficult (e.g., Svahnberg and Piazzolo, 2010; Hentschel et al., 2019 and references therein), we interpret that grain size reduction of plagioclase is induced by nucleation and subsequent growth in which new, relatively strain-free grains grow at the expense of highly strained grains by strain-induced grain boundary migration (e.g., Tullis and Yund, 1987; Trepmann et al., 2017; Hentschel et al., 2019), inheriting the crystallographic orientation of their hosts. Such process of grain size reduction in feldspar has also been observed in both experimentally (Stünitz et al., 2003) and naturally deformed high temperature rocks (e.g., Menegon et al., 2013; Okudaira et al., 2015). As evidence of fluids are present in the host rock in contact to the shear zone, strain-induced grain boundary migration may be locally enhanced by a driving chemical potential (Stünitz, 1998).

Olivine porphyroclasts show undulatory extinction and intragranular microfractures, but no evidence of dynamic recrystallization (Figs. 2, 3e). In the enstatite-rich layer associated with olivine, symplectite textures of magnetite with enstatite, a weak enstatite CPO, and embayment of enstatite into the olivine porphyroclast (Figs. 3f, 9) suggest diffusive transfer reactions with olivine (Holness et al., 2011) in the presence of a hydrous melt phase (Stuart et al., 2016; Gardner et al., 2020). Evidence of the former presence of melt is seen as thin films of amphibole and magnetite along grain boundaries, low dihedral angles and embayments (Fig. 3f; Stuart et al., 2018; Lee et al., 2018). Magnetite and enstatite are found in the microfractures crosscutting olivine porphyroclasts, which may have formed by similar diffusion-assisted exchange reactions. The absence of low temperature hydrous minerals, such as serpentine, suggest that diffusion reactions took place under high temperature conditions.

Overall, in the host gabbro, microfractures, low-angle grain boundaries and internal misorientations in diopside, plagioclase and olivine are restricted to the border of the ultramylonite (Figs. 2, 3, 5-8), which implies that the recorded dislocation-glide controlled deformation associated with fracturing, i.e. high-stress crystal plasticity, is related to the formation of the ultramylonite.

5.2. Deformation mechanisms in the ultramylonite: porphyroclasts versus matrix

Plagioclase and diopside porphyroclasts in the ultramylonite represent preserved primary grains from the host gabbro. As in the host rock, plagioclase

porphyroclasts show evidence of crystal plastic deformation, such as undulatory extinction, bent grains, mechanical twins, low-angle grain boundaries and progressive internal misorientation within porphyroclasts (Figs. 10 a, b, d). The secondary plagioclase grains rimming the porphyroclasts are almost strain free and show a crystallographic orientation controlled by the host crystal. Thus, the CPO cannot be taken as indication of a glide system, as discussed for the host plagioclase. As the microstructures of new plagioclase grains associated with porphyroclasts in the ultramylonite are quite similar to those in the host rock (Figs. 6, 10), we interpret that they have formed by similar processes (strain-induced replacement of plagioclase porphyroclasts).

Likewise, diopside porphyroclasts in the ultramylonite display similar microstructures as the deformed crystals in the host gabbro at the contact with the ultramylonite zone, including bent cleavages, internal misorientation (undulatory extinction and low angle grain boundaries) and kink bands. New grains in subset₁ show evidence of formation along former fractures and along kink bands (Fig. 11), i.e., localized to zones of increased strain. As the CPO of diopside in subset₁ is not host-controlled, and does not correlate with any known glide system for diopside (Fig. 11d), we propose that local higher strain associated to bending and kink bands favored the nucleation and growth of new grains in subset₁.

In contrast, the fine grains of diopside in subset₂ are mostly strain free, lack a clear CPO and have irregular grain boundaries (Figs. 11a, b). Furthermore, they grade into polyphase aggregates with distance to the boundary of the host porphyroclasts. We interpret these grains in subset₂ either to have formed by dissolution-precipitation creep and/or to have been sheared and rotated during creep within the ultramylonite matrix. Either way, the polyphase matrix with increasing amphibole content suggests that dissolution-precipitation creep accommodates the reaction to form the secondary diopside grains in subset₂, likely as a response to a chemical driving potential in the presence of a fluid phase (e.g., Marti et al. 2017; Mansard et al. 2020; Stünitz et al. 2020).

Additionally, the amphibole rimming diopside porphyroclasts forming asymmetric tails along the clasts indicates precipitation and metamorphic reactions during deformation (Figs. 4c, 11a, 12a, b). Embayment and overgrowth (i.e., truncation) of amphibole into diopside (subset₂), and progressive decrease of diopside – and

increase of amphibole - in the asymmetric tails away from the diopside host (Fig. 11a) evidence the positive feedback between strain and fluid-rock interaction, leading to the consumption of diopside and precipitation of amphibole (e.g., Berger and Stünitz 1996; Getsinger and Hirth 2014; Giuntoli et al. 2018; Marti et al., 2018; Mansard et al. 2020). The precipitation of strain-free amphibole is accompanied by a strong CPO and SPO, with their (100) planes parallel to the foliation (i.e., XY plane), and [001] axes near the stretching direction (X), matching with the long axes of the grains (Fig. 12). This correlation between shape and crystallographic preferred orientation of amphibole reflects the growth at non-isostatic stress conditions (e.g., Berger and Stünitz, 1996; Getsinger and Hirth, 2014; Okudaira et al., 2015; Van der Werf et al., 2017; Giuntoli et al., 2018), as the [001] axis is the fastest growth direction in amphibole (Getsinger and Hirth, 2014). Similar amphibole microfabrics are observed in the amphibole-rich layer associated with progressive replacement of enstatite and magnetite after olivine at the boundary of the shear zone (Fig. 9), and we interpret them as having formed by the same process, which may explain the absence of olivine remnants in the ultramylonite. Thus, these microstructures indicate that diffusive mass transport plays a crucial role during reaction, promoting grain size reduction and phase mixing.

Away from plagioclase and diopside porphyroclasts, the secondary grains of plagioclase, amphibole and Fe-Ti oxides form the polyphase matrix (Figs. 4; 13). The crystallographic orientations of plagioclase in the polyphase matrix are almost random, while amphibole shows an associated SPO and CPO with (100) planes parallel to the foliation and [001] axes near the X direction (Fig. 13), according to its high shape anisotropy. As intracrystalline plasticity is generally absent in both plagioclase and amphibole, we interpret that these microstructures indicate dissolution-precipitation creep, probably associated with grain boundary sliding and rigid body rotation (e.g., Berger and Stünitz, 1996; Kanagawa et al., 2008). The high amount of phase boundaries inhibits grain growth, such that the small grain-size is preserved in the polyphase matrix (e.g., Kruse and Stünitz, 1999; Herwegh and Berger, 2004; Kilian et al., 2011; Mansard et al., 2018) and promotes diffusion creep and grain boundary sliding as the dominant steady-state deformation mechanisms (e.g., Füsseis et al., 2009; Menegon et al., 2015; Platt, 2015; Lopez-Sanchez and Llana-Fúnez, 2018).

5.3. Deformation conditions indicated by deformation mechanisms

Recent results on thermodynamic modelling in gabbro mylonites from the lower portion of hole U1473A have shown that deformation occurred under granulite facies conditions at ~835°C-890°C (Taufner et al., 2021). This observation is also proposed by Allard et al. (2021) based on the CPO of deformed plagioclase aggregates from high temperature shear zones from hole U1473A, suggesting that deformation took place under a temperature range of ~650°C-1000°C. Similar temperature conditions have been found in gabbro mylonites from hole 735B, with widespread evidence of dynamic recrystallization of plagioclase (Mehl and Hirth, 2008; Miranda and John, 2010).

Plagioclase and diopside porphyroclasts, both in the host rock and in the ultramylonite analyzed in this study, indicate deformation mainly by glide-controlled creep associated with microfracturing, i.e. high-stress crystal plasticity prior to infiltration of fluids and development of hydrothermal reactions. Transient changes in pore-fluid pressure during uplift of the crust may have played a role in promoting microfracturing (e.g., Spiess et al., 2017; Locatelli et al., 2018; Dick et al., 2019b). As segregation of Fe-Ti oxides occur as late-stage melts in many high temperature deformed assemblages in the Atlantis Bank, (MacLeod et al., 2017; Dick et al., 2019b; Taufner et al., 2021), and are present in the shear zone and in adjacent microfractures, they may be interpreted as indicative of the former presence of melt (Fig. 8a, e.g., Lee et al., 2018), which would be preferentially localized in the ultramylonite.

In the fine-grained shear zones from the Atlantis Bank, brittle deformation followed by infiltration of aqueous fluids and amphibole-forming hydration reactions are suggested to occur between ~600-820°C, near the viscous-brittle transition (Miranda and John, 2010; Taufner et al., 2021). This is in agreement with dissolution of diopside and precipitation of amphibole within microfractures in both the host rock and ultramylonite, as a response to fluid-rock interaction (Figs. 11, 12). Such patterns suggest that these structures constituted localized pathways for fluid flow, and facilitated fluid-bearing metamorphic growth. As mafic assemblages are highly sensitive to changes in pressure, temperature and fluid composition, dissolution-precipitation creep facilitating reactions likely accommodates most of the strain. In addition, the absence of serpentine also indicates temperatures >600°C during deformation (e.g., Hermann et al., 2000; Scambelluri et al., 2004), in agreement with

the lack of low temperature mineral assemblages commonly found in mafic tectonites in the middle-lower oceanic crust (e.g., chlorite, epidote and serpentine; Miranda and John, 2010).

Thus, based on the microstructures and inferred deformation mechanisms recorded in our sample, we suggest that the host rock initially deformed under conditions $>600^{\circ}\text{C}$ (e.g., Taufner et al., 2021) at transient high stresses that led to high-stress crystal plasticity combined with dislocation glide and associated fracturing. Subsequent localized fluid flow along highly damaged zones caused hydration reactions and resulted in strain localization and formation of the ultramylonite.

5.4. Implications on the deformation history

The tectonic setting of the investigated ultramylonitic shear zone at the Atlantis Bank oceanic core complex, bounded by the 7.5 Ma Atlantis II Transform fault, suggests that coupled strain localization and fluid-rock interactions occurred under transient stress- and strain rates, which may be possibly associated with the seismic cycle. The dominating process of grain size reduction of feldspar and pyroxene in the host rock is interpreted to be dislocation glide and cataclasis (i.e. high-stress crystal-plasticity) followed by strain-induced replacement (Fig. 14), (e.g., Hentschel et al. 2019). Dislocation glide of diopside at the given conditions requires high stresses (e.g., Moghadam et al. 2010). Transient high-stress crystal-plasticity in a crustal layer undergoing creep on a long term can be explained by seismic rupturing in the overlying seismogenic layer (e.g., Ellis and Stöckhert, 2004; Chatzaras et al., 2020). On the other hand, while transient fracturing in a crustal layer undergoing creep on a long term might also be explained by decreasing temperatures (Miranda and John, 2010) or an increase in pore-fluid pressure (Dick et al., 2019a), both possibilities do not fully account for the evidence of high stress crystal-plasticity localized in the ultramylonite and the host rock at the boundary with the shear zone. Furthermore, the absence of low temperature mineral assemblages in the shear zone suggests that temperature was not a major factor controlling the microstructural evolution of the ultramylonite.

Microfracturing likely created the anisotropy and permeability that allowed for the influx of aqueous fluids into the shear zone (e.g., Guermani and Pennacchioni, 1998; Küster and Stöckhert, 1999; Trepmann and Stöckhert, 2002; Mancktelow and Pennacchioni, 2005; Pennacchioni and Mancktelow, 2007), leading to metastability and hydration of the otherwise dry mafic assemblage, and the onset of fluid-rock

interactions. Fracturing has been proposed as an important process acting as a mechanical precursor of ductile shear zones because it reduces the strength of the rock and acts as a fast pathway for fluid percolation, favoring fluid-rock interaction and phase mixing (e.g., Segall and Simpson, 1986; Austrheim, 1987; Mancktelow and Pennacchioni, 2005; Pennacchioni and Mancktelow, 2007; Füsseis et al., 2009; Goncalves et al., 2016; Pennacchioni and Mancktelow, 2018; Papeschi and Musumeci, 2019). Fluid channeling in the shear zone evidences the role of fluids as weakening agents as the original dry mafic assemblage is almost completely replaced by a highly localized amphibole-rich rock (Fig. 2). In the shear zone, the deformed host gabbro is mostly replaced by a hydrated mineral assemblage comprising amphibole and secondary plagioclase, through the replacement of diopside, enstatite and magnetite, and strain-induced replacement of plagioclase, evidencing the positive feedback between brittle and viscous deformation in the presence of hydrous mineral reactions at high temperature conditions (e.g., Marti et al., 2017, 2018).

The importance of fluid-rock reactions for promoting local weakening processes and strain localization have been recently documented in lower crustal gabbro mylonites from Hole U1473A (Taufner et al., 2021) and 735B (Gardner et al., 2020) in the Atlantis Bank. Mehl and Hirth (2008) and Miranda (2006) postulate that strain localization and exhumation of the Atlantis Bank are accompanied by a shift from grain-size-insensitive (GSI) to grain-size-sensitive (GSS) mechanisms at strain rates of $\sim 10^{-12}$ to 10^{-11} s⁻¹ (Mehl and Hirth, 2008; Miranda, 2006). However, they do not observe widespread evidence of hydration in their samples, and suggest that the shift to GSS creep occurred in relatively 'dry' conditions. On the other hand, Taufner et al. (2021) and Gardner et al. (2020) show that this weakening also takes place in the presence of fluids, nucleating fine-grained reaction products, enhancing diffusion creep, and further promoting strain localization. Microstructural data in the ultramylonite analyzed in this study support the latter observations and provide additional evidence that strain localization in high temperature ultramylonitic shear zones from Atlantis Bank is largely controlled by hydration reactions.

Fluid channeling in lower crustal shear zones along former microfractures decreases the viscosity of the crust by enhancing synkinematic mineral reactions during dissolution-precipitation creep, favoring steady-state flow, and creating localized zones of extreme rheological weakening that deform at far lower stresses (or

higher strain rates) than the surrounding rocks (i.e., ultramylonites, Fig. 14; Marti et al., 2018). Hence, the percolation of water during high temperature deformation along lower crustal shear zones in the oceanic crust exerts an important control in the mode that strain localizes (Mevel and Cannat, 1991). As the ultramylonite is mechanically weaker (compared to the host rock) during creep, most of the strain tends to be accommodated in the shear zone where fluid-present, grain size sensitive mechanisms facilitated strain localization and prevented and/or retarded shear zone widening (Finch et al., 2016; Oliot et al., 2014). These processes have significant implications for the strength of the lithosphere during detachment faulting and tectonic spreading, leading to hydration, weakening and exhumation of initially 'dry', metastable and stressed granulitic lower crust at mid-ocean ridges.

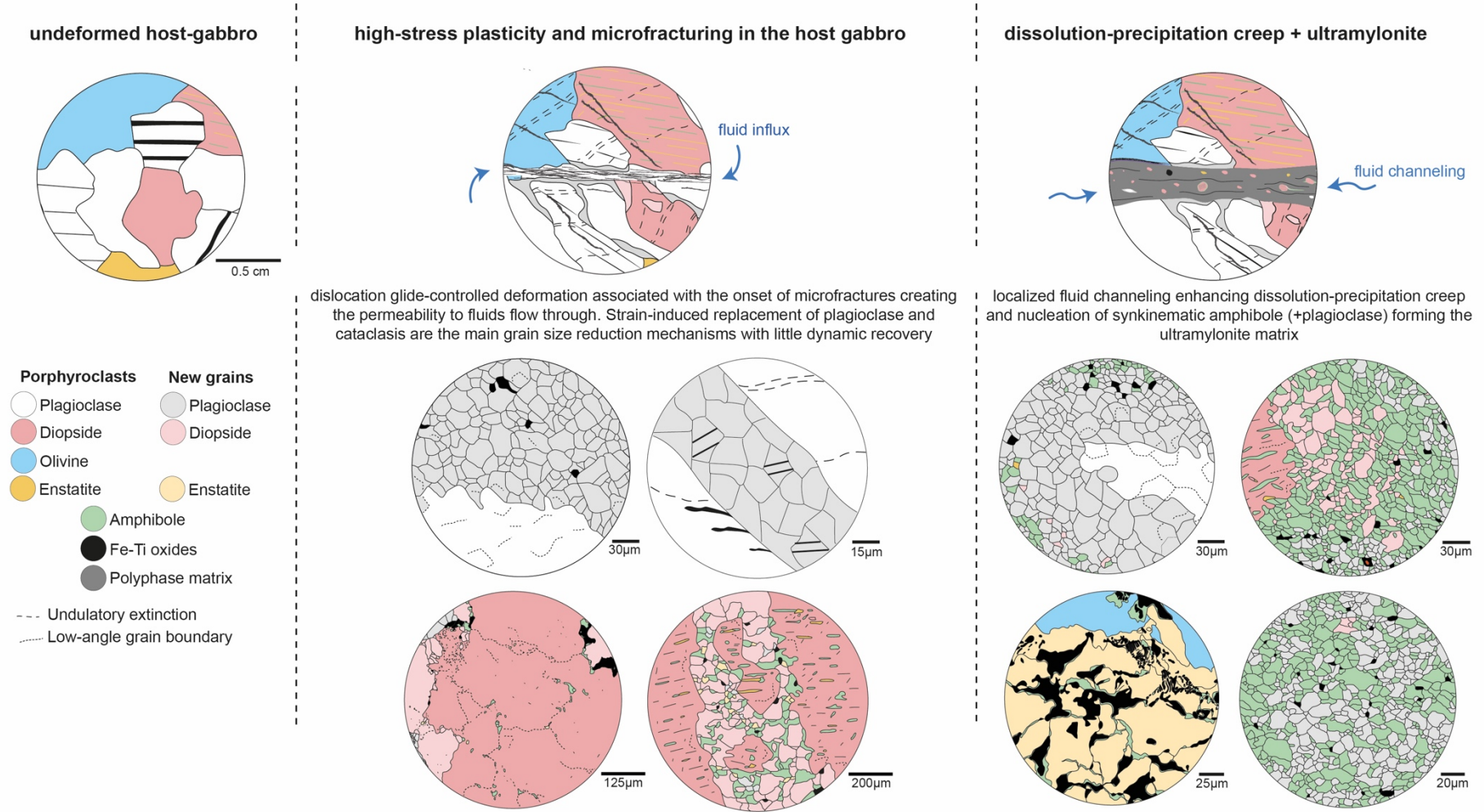


Figure 14. Schematic illustration of the microstructural processes from an initially undeformed and 'dry' host-gabbro to a highly localized and 'wet' ultramylonitic shear zone (see text for discussion).

6. Conclusions

Our microfabric analysis in a lower crustal shear zone from the Atlantis Bank oceanic core complex shows the interplay between crystal-plasticity, brittle deformation and fluid flow leading to a highly localized fluid-bearing ultramylonite during exhumation of the lower crust. The deformation microstructures of the porphyroclasts in the ultramylonite correspond to those in the host gabbro at the contact with the ultramylonite zone. At a distance from the ultramylonite zone, these deformation microstructures become less prevalent in the host rock. Therefore, they are interpreted to represent the nucleation of the ultramylonite zone, while the matrix of the ultramylonite represents subsequent strain localization. Deformation in the host rock, including the porphyroclasts in the ultramylonite, records dislocation glide-controlled creep in a high-stress, crystal-plastic regime with initial grain size reduction being triggered by strain-induced replacement and fracturing, forming fluid pathways favoring fluid-rock interaction and mineral reaction in the metastable 'dry' gabbro. Such patterns ultimately led to the development of the fine-grained, polyphase ultramylonite matrix. The fine grain size and phase mixing in the matrix favor deformation in the diffusional creep regime associated with grain boundary sliding, leading to strain localization within the ultramylonite zone and thus preventing further strain accumulating in the host rock. Deformation then shifted from grain size insensitive to grain size sensitive creep in the ultramylonite. This also led to the localized presence of fluids that are restricted to the ultramylonite layer, recorded by the minor presence of amphibole in fractured host crystals (Figs. 4c, 8), enstatite, Fe-Ti oxides and amphibole (Figs. 3e, f, 9) at the boundary with the ultramylonite, and the widespread distributed occurrence of amphibole in the ultramylonite matrix (Figs. 10a, 11b, 12, 13a)

Microfractures seem to play an important role in creating pathways for pervasive fluid-rock interaction in shear zones at high-grade conditions, ultimately leading to strain localization in fine-grained ultramylonites in which fluids are channelized. Hence, the rheology of the lower oceanic crust at mid ocean ridges is strongly controlled by the presence of fluids that enhance mineral replacement and phase mixing. This positive feedback between brittle deformation, fluid influx and newly precipitated hydrated reactant products weakens the lower crust, facilitating tectonic spreading along crustal-scale detachment faults and exhumation of oceanic core complexes.

7. References

- Aben, F.M., Doan, M.-L., Mitchell, T.M., Toussaint, R., Reuschlé, T., Fondriest, M., Gratier, J.-P., Renard, F., 2016. Dynamic fracturing by successive coseismic loadings leads to pulverization in active fault zones. *Journal of Geophysical Research: Solid Earth* 121, 2338–2360. <https://doi.org/10.1002/2015JB012542>
- Allard, M., Ildefonse, B., Oliot, É., Barou, F., 2021. Plastic Deformation of Plagioclase in Oceanic Gabbro Accreted at a Slow-Spreading Ridge (Hole U1473A, Atlantis Bank, Southwest Indian Ridge). *Journal of Geophysical Research: Solid Earth* 126, e2021JB021964. <https://doi.org/10.1029/2021JB021964>
- Austrheim, H., 1987. Eclogitization of lower crustal granulites by fluid migration through shear zones. *Earth and Planetary Science Letters* 81, 221–232. [https://doi.org/10.1016/0012-821X\(87\)90158-0](https://doi.org/10.1016/0012-821X(87)90158-0)
- Bachmann, F., Hielscher, R., Schaeben, H., 2011. Grain detection from 2d and 3d EBSD data-Specification of the MTEX algorithm. *Ultramicroscopy* 111, 1720–1733. <https://doi.org/10.1016/j.ultramic.2011.08.002>
- Bachmann, F., Hielscher, R., Schaeben, H., 2010. Texture Analysis with MTEX – Free and Open Source Software Toolbox. *Solid State Phenomena* 160, 63–68. <https://doi.org/10.4028/www.scientific.net/ssp.160.63>
- Baines, A.G., Cheadle, M.J., John, B.E., Schwartz, J.J., 2008. The rate of oceanic detachment faulting at Atlantis Bank, SW Indian Ridge. *Earth and Planetary Science Letters* 273, 105–114. <https://doi.org/10.1016/J.EPSL.2008.06.013>
- Barclay, A.H., Toomey, D.R., Solomon, S.C., 2001. Microearthquake characteristics and crustal V_P / V_S structure at the Mid-Atlantic Ridge, 35°N. *Journal of Geophysical Research: Solid Earth* 106, 2017–2034. <https://doi.org/10.1029/2000JB900371>
- Berger, A., Stünitz, H., 1996. Deformation mechanisms and reaction of hornblende: examples from the Bergell tonalite (Central Alps). *Tectonophysics* 257, 149–174. [https://doi.org/10.1016/0040-1951\(95\)00125-5](https://doi.org/10.1016/0040-1951(95)00125-5)
- Blackman, D.K., Cann, J.R., Janssen, B., Smith, D.K., 1998. Origin of extensional core complexes: Evidence from the Mid-Atlantic Ridge at Atlantis Fracture Zone. *Journal of Geophysical Research: Solid Earth* 103, 21315–21333.

<https://doi.org/10.1029/98JB01756>

Bos, B., Spiers, C., 2001. Experimental investigation into the microstructural and mechanical evolution of phyllosilicate-bearing fault rock under conditions favouring pressure solution. *Journal of Structural Geology* 23, 1187–1202. [https://doi.org/10.1016/S0191-8141\(00\)00184-X](https://doi.org/10.1016/S0191-8141(00)00184-X)

Bunge, H.-J. 1982. *Texture analysis in materials science: mathematical methods*. Butterworths, London.

Bürgmann, R., Dresen, G., 2008. Rheology of the Lower Crust and Upper Mantle: Evidence from Rock Mechanics, Geodesy, and Field Observations. *Annual Review of Earth and Planetary Sciences* 36, 531–567. <https://doi.org/10.1146/annurev.earth.36.031207.124326>

Cann, J.R., Blackman, D.K., Smith, D.K., McAllister, E., Janssen, B., Mello, S., Avgerinos, E., Pascoe, A.R., Escartin, J., 1997. Corrugated slip surfaces formed at ridge–transform intersections on the Mid-Atlantic Ridge. *Nature* 385, 329–332. <https://doi.org/10.1038/385329a0>

Cannat, M., Mével, C., Stakes, D., 1991. Normal Ductile Shear Zones at an Oceanic Spreading Ridge: Tectonic Evolution of Site 735 Gabbros (Southwest Indian Ocean). *Proceedings of the Ocean Drilling Program, 118 Scientific Results* 118, 415–429. <https://doi.org/10.2973/odp.proc.sr.118.157.1991>

Carter, N.L., Kronenberg, A.K., Ross, J. V., Wiltschko, D. V., 1990. Control of fluids on deformation of rocks. *Geological Society, London, Special Publications* 54, 1–13. <https://doi.org/10.1144/GSL.SP.1990.054.01.01>

Chatzaras, V., Tikoff, B., Kruckenberg, S.C., Titus, S.J., Teyssier, C., Drury, M.R., 2020. Stress variations in space and time within the mantle section of an oceanic transform zone: Evidence for the seismic cycle. *Geology* 48, 569–573. <https://doi.org/10.1130/G47137.1>

Condit, C.B., Mahan, K.H., 2018. Fracturing, fluid flow and shear zone development: Relationships between chemical and mechanical processes in Proterozoic mafic dykes from southwestern Montana, USA. *Journal of Metamorphic Geology* 36, 195–223. <https://doi.org/10.1111/jmg.12289>

Díaz Aspiroz, M., Lloyd, G.E., Fernández, C., 2007. Development of lattice preferred

- orientation in clinoamphiboles deformed under low-pressure metamorphic conditions. A SEM/EBSD study of metabasites from the Aracena metamorphic belt (SW Spain). *Journal of Structural Geology* 29, 629–645. <https://doi.org/10.1016/J.JSG.2006.10.010>
- Dick, H.J.B., Kvassnes, A.J.S., Robinson, P.T., MacLeod, C.J., Kinoshita, H., 2019a. The Atlantis Bank gabbro massif, southwest Indian ridge. *Progress in Earth and Planetary Science* 6, 64. <https://doi.org/10.1186/s40645-019-0307-9>.
- Dick, H.J.B., Macleod, C.J., Blum, P., 2016. Expedition 360 Preliminary Report: Southwest Indian Ridge lower crust and Moho. International Ocean Discovery Program. <https://doi.org/10.14379/iodp.pr.360.2016>
- Dick, H.J.B., MacLeod, C.J., Blum, P., Abe, N., Blackman, D.K., Bowles, J.A., Cheadle, M.J., Cho, K., Ciałęła, J., Deans, J.R., Edgcomb, V.P., Ferrando, C., France, L., Ghosh, B., Ildefonse, B., John, B., Kendrick, M.A., Koepke, J., Leong, J.A.M., Liu, C., Ma, Q., Morishita, T., Morris, A., Natland, J.H., Nozaka, T., Pluemper, O., Sanfilippo, A., Sylvan, J.B., Tivey, M.A., Tribuzio, R., Viegas, G., 2019b. Dynamic Accretion Beneath a Slow-Spreading Ridge Segment: IODP Hole 1473A and the Atlantis Bank Oceanic Core Complex. *Journal of Geophysical Research: Solid Earth* a, 1–29. <https://doi.org/10.1029/2018JB016858>
- Dick, H.J.B., Meyer, P.S., Bloomer, S., Kirby, S., Stakes, D., Mawer, C., 1991. Lithostratigraphic Evolution of an In-Situ Section of Oceanic Layer 3. *Proceedings of the Ocean Drilling Program, 118 Scientific Results*. Ocean Drilling Program. <https://doi.org/10.2973/odp.proc.sr.118.128.1991>
- Dimanov, A., Dresen, G., 2005. Rheology of synthetic anorthite-diopside aggregates: Implications for ductile shear zones. *Journal of Geophysical Research* 110, B07203. <https://doi.org/10.1029/2004JB003431>
- Drury, M. 1993. Defects and Processes in the Solid State: Geoscience Applications The McLaren Volume, Chap. Deformation lamellae in metals and minerals, 195–212.
- Ellis, S., Stöckhert, B., 2004. Elevated stresses and creep rates beneath the brittle-ductile transition caused by seismic faulting in the upper crust. *J. Geophys. Res.* 109, B05407. <https://doi.org/10.1029/2003JB002744>.

- Etheridge, M.A., Wall, V.J., Vernon, R.H., 1983. The role of the fluid phase during regional metamorphism and deformation. *Journal of Metamorphic Geology* 1, 205–226. <https://doi.org/10.1111/j.1525-1314.1983.tb00272.x>
- Ferrando, C., France, L., Basch, V., Sanfilippo, A., Tribuzio, R., Boulanger, M., 2021. Grain Size Variations Record Segregation of Residual Melts in Slow-Spreading Oceanic Crust (Atlantis Bank, 57°E Southwest Indian Ridge). *Journal of Geophysical Research: Solid Earth* 126, e2020JB020997. <https://doi.org/10.1029/2020JB020997>
- Ferrando, C., Tribuzio, R., Lissenberg, C.J., France, L., MacLeod, C.J., Basch, V., Villeneuve, J., Deloule, E., Sanfilippo, A., 2022. Brown Amphibole as Tracer of Tectono-Magmatic Evolution of the Atlantis Bank Oceanic Core Complex (IODP Hole U1473A). *Journal of Petrology* 63, egac089. <https://doi.org/10.1093/petrology/egac089>
- Finch, M.A., Weinberg, R.F., Hunter, N.J.R., 2016. Water loss and the origin of thick ultramylonites. *Geology* 44, 599–602. <http://dx.doi.org/10.1130/G37972.1>
- Fitz Gerald, J.D., Stünitz, H., 1993. Deformation of granitoids at low metamorphic grade. I: Reactions and grain size reduction. *Tectonophysics* 221, 269–297. [https://doi.org/10.1016/0040-1951\(93\)90163-E](https://doi.org/10.1016/0040-1951(93)90163-E)
- Freed, A.M., Bürgmann, R., 2004. Evidence of power-law flow in the Mojave desert mantle. *Nature* 430, 548–551. <https://doi.org/10.1038/nature02784>
- Fusseis, F., Regenauer-Lieb, K., Liu, J., Hough, R.M., De Carlo, F., 2009. Creep cavitation can establish a dynamic granular fluid pump in ductile shear zones. *Nature* 459, 974–977. <https://doi.org/10.1038/nature08051>
- Gardner, R.L., Piazzolo, S., Daczko, N.R., Trimby, P., 2020. Microstructures reveal multistage melt present strain localisation in mid-ocean gabbros. *Lithos* 366–367, 105572. <https://doi.org/10.1016/j.lithos.2020.105572>
- Getsinger, A.J., Hirth, G., 2014. Amphibole fabric formation during diffusion creep and the rheology of shear zones. *Geology* 42, 535–538. <https://doi.org/10.1130/G35327.1>
- Getsinger, A.J., Hirth, G., Stünitz, H., Goergen, E.T., 2013. Influence of water on rheology and strain localization in the lower continental crust. *Geochemistry,*

- Geophysics, Geosystems 14, 2247–2264. <https://doi.org/10.1002/ggge.20148>
- Giuntoli, F., Menegon, L., Warren, C.J., 2018. Replacement reactions and deformation by dissolution and precipitation processes in amphibolites. In: Brown, M. (Ed.), *Journal of Metamorphic Geology* 36, 1263–1286. <https://doi.org/10.1111/jmg.12445>
- Goncalves, P., Oliot, E., Marquer, D., Connolly, J.A.D., 2012. Role of chemical processes on shear zone formation: an example from the Grimsel metagranodiorite (Aar massif, Central Alps). *Journal of Metamorphic Geology* 30, 703–722. <https://doi.org/10.1111/j.1525-1314.2012.00991.x>
- Goncalves, P., Poilvet, J.-C., Oliot, E., Trap, P., Marquer, D., 2016. How does shear zone nucleate? An example from the Suretta nappe (Swiss Eastern Alps). *Journal of Structural Geology* 86, 166–180. <https://doi.org/10.1016/j.jsg.2016.02.015>
- Green, H., Radcliffe, S., 1972. Deformation processes in the upper mantle. *Geoph. Mono Series* 16, 139–156.
- Guermani, A., Pennacchioni, G., 1998. Brittle precursors of plastic deformation in a granite: an example from the Mont Blanc massif (Helvetic, western Alps). *Journal of Structural Geology* 20, 135–148. [https://doi.org/10.1016/S0191-8141\(97\)00080-1](https://doi.org/10.1016/S0191-8141(97)00080-1)
- Gueydan, F., Leroy, Y.M., Jolivet, L., Agard, P., 2003. Analysis of continental midcrustal strain localization induced by microfracturing and reaction-softening. *Journal of Geophysical Research: Solid Earth* 108. <https://doi.org/10.1029/2001JB000611>
- Handy, M.R., 1989. Deformation regimes and the rheological evolution of fault zones in the lithosphere: the effects of pressure, temperature, grain size and time. *Tectonophysics* 163, 119–152. [https://doi.org/10.1016/0040-1951\(89\)90122-4](https://doi.org/10.1016/0040-1951(89)90122-4)
- Hawemann, F., Mancktelow, N.S., Pennacchioni, G., Wex, S., Camacho, A., 2019. Weak and Slow, Strong and Fast: How Shear Zones Evolve in a Dry Continental Crust (Musgrave Ranges, Central Australia). *Journal of Geophysical Research: Solid Earth* 124, 219–240. <https://doi.org/10.1029/2018JB016559>
- Hentschel, F., Trepmann, C. A., Janots, E. 2019. Deformation of feldspar at greenschist facies conditions – the record of mylonitic pegmatites from the

- Pfunderer Mountains, Eastern Alps, *Solid Earth*, 10, 95–116, <https://doi.org/10.5194/se-10-95-2019>
- Hermann, J., Müntener, O., Scambelluri, M., 2000. The importance of serpentinite mylonites for subduction and exhumation of oceanic crust. *Tectonophysics* 327, 225–238. [https://doi.org/10.1016/S0040-1951\(00\)00171-2](https://doi.org/10.1016/S0040-1951(00)00171-2)
- Herwegh, M., Berger, A., 2004. Deformation mechanisms in second-phase affected microstructures and their energy balance. *Journal of structural geology*, 26(8), 1483–1498.
- Holness, M.B., Cesare, B., Sawyer, E.W., 2011. Melted Rocks under the Microscope: Microstructures and Their Interpretation. *Elements* 7, 247–252. <https://doi.org/10.2113/gselements.7.4.247>
- Imon, R., Okudaira, T., Fujimoto, A., 2002. Dissolution and precipitation processes in deformed amphibolites: an example from the ductile shear zone of the Ryoke metamorphic belt, SW Japan. *Journal of Metamorphic Geology* 20, 297–308. <https://doi.org/10.1046/j.1525-1314.2002.00367.x>
- Ingles, J., Lamouroux, C., Soula, J.-C., Guerrero, N., Debat, P., 1999. Nucleation of ductile shear zones in a granodiorite under greenschist facies conditions, Néouvielle massif, Pyrenees, France. *Journal of Structural Geology* 21, 555–576. [https://doi.org/10.1016/S0191-8141\(99\)00042-5](https://doi.org/10.1016/S0191-8141(99)00042-5)
- Ingrin, J., Doukhan, N., Doukhan, J.C., 1991. High-temperature deformation of diopside single crystal: 2. Transmission electron microscopy investigation of the defect microstructures. *Journal of Geophysical Research: Solid Earth* 96, 14287–14297. <https://doi.org/10.1029/91JB01233>
- Jackson, J., 2002. Strength of the continental lithosphere: Time to abandon the jelly sandwich? *GSA Today* 12, 4. [https://doi.org/10.1130/1052-5173\(2002\)012<0004:SOTCLT>2.0.CO;2](https://doi.org/10.1130/1052-5173(2002)012<0004:SOTCLT>2.0.CO;2)
- Jamtveit, B., Austrheim, H., Putnis, A., 2016. Disequilibrium metamorphism of stressed lithosphere. *Earth-Science Reviews* 154, 1–13. <https://doi.org/10.1016/J.EARSCIREV.2015.12.002>
- Jamtveit, B., Petley-Ragan, A., Incel, S., Dunkel, K.G., Aupart, C., Austrheim, H., Corfu, F., Menegon, L., Renard, F., 2019. The Effects of Earthquakes and Fluids

- on the Metamorphism of the Lower Continental Crust. *Journal of Geophysical Research: Solid Earth* 124, 7725–7755. <https://doi.org/10.1029/2018JB016461>
- Kanagawa, K., Shimano, H., Hiroi, Y., 2008. Mylonitic deformation of gabbro in the lower crust: A case study from the Pankenushi gabbro in the Hidaka metamorphic belt of central Hokkaido, Japan. *Journal of Structural Geology* 30, 1150–1166. <https://doi.org/10.1016/J.JSG.2008.05.007>
- Keulen, N., Heilbronner, R., Stünitz, H., Boullier, A.-M., Ito, H., 2007. Grain size distributions of fault rocks: A comparison between experimentally and naturally deformed granitoids. *Journal of Structural Geology* 29, 1282–1300. <https://doi.org/10.1016/J.JSG.2007.04.003>
- Kilian, R., Heilbronner, R., Stünitz, H., 2011. Quartz microstructures and crystallographic preferred orientation: Which shear sense do they indicate? *Journal of Structural Geology* 33, 1446–1466. <https://doi.org/10.1016/J.JSG.2011.08.005>
- Klaper, E.M., 1990. Reaction-enhanced formation of eclogite-facies shear zones in granulite-facies anorthosites. Geological Society, London, Special Publications 54, 167–173. <https://doi.org/10.1144/GSL.SP.1990.054.01.16>
- Kohlstedt, D.L., Evans, B., Mackwell, S.J., 1995. Strength of the lithosphere: Constraints imposed by laboratory experiments. *Journal of Geophysical Research: Solid Earth* 100, 17587–17602. <https://doi.org/10.1029/95JB01460>
- Kruse, R., Stünitz, H., 1999. Deformation mechanisms and phase distribution in mafic high-temperature mylonites from the Jotun Nappe, southern Norway. *Tectonophysics* 303, 223–249. [https://doi.org/10.1016/S0040-1951\(98\)00255-8](https://doi.org/10.1016/S0040-1951(98)00255-8)
- Küster, M., Stöckhert, B., 1999. High differential stress and sub-lithostatic pore fluid pressure in the ductile regime: microstructural evidence for short-term post-seismic creep in the Sesia Zone, Western Alps. *Tectonophysics* 303, 263–277
- Lee, A.L., Torvela, T., Lloyd, G.E., Walker, A.M., 2018. Melt organisation and strain partitioning in the lower crust. *Journal of Structural Geology* 113, 188–199. <https://doi.org/10.1016/J.JSG.2018.05.016>
- Locatelli, M., Verlaquet, A., Agard, P., Federico, L., Angiboust, S., 2018. Intermediate-depth brecciation along the subduction plate interface (Monviso eclogite, W.

- Alps). *Lithos* 320–321, 378–402. <https://doi.org/10.1016/J.LITHOS.2018.09.028>
- Lopez-Sanchez, M.A., Llana-Fúnez, S., 2018. A cavitation-seal mechanism for ultramylonite formation in quartzofeldspathic rocks within the semi-brittle field (Vivero fault, NW Spain). *Tectonophysics* 745, 132–153. <https://doi.org/10.1016/J.TECTO.2018.07.026>
- Macleod, C.J., Blum, P., Abe, N., Blackman, D.K., Bowles, J.A., Cheadle, M.J., Cho, K., Deans, J.R., Edgcomb, V.P., Ferrando, C., France, L., Ghosh, B., Ildefonse, B.M., Kendrick, M.A., Koepke, J.H., Liu, C., Morishita, T., Morris, A., Natland, J.H., Nozaka, T., Pluemper, O., Sanfilippo, A., Sylvan, J.B., Tivey, M.A., Tribuzio, R., Ridge, S.I., Bank, A., 2017. Site U1473. *Proceedings of the International Ocean Discovery Program*, 360. <https://doi.org/10.14379/iodp.proc.360.103.2017>
- MacLeod, C.J., Escartín, J., Banerji, D., Banks, G.J., Gleeson, M., Irving, D.H.B., Lilly, R. M., McCaig, A.M., Niu, Y., Allerton, S., Smith, D.K., 2002. Direct geological evidence for oceanic detachment faulting: the Mid-Atlantic Ridge. 15°45'N. *Geology* 30, 879. [https://doi.org/10.1130/0091-7613\(2002\)030<0879:DGEFOD>2.0.CO;2](https://doi.org/10.1130/0091-7613(2002)030<0879:DGEFOD>2.0.CO;2).
- Mancktelow, N.S., Pennacchioni, G., 2005. The control of precursor brittle fracture and fluid–rock interaction on the development of single and paired ductile shear zones. *Journal of Structural Geology* 27, 645–661. <https://doi.org/10.1016/J.JSG.2004.12.001>
- Mansard, N., Raimbourg, H., Augier, R., Précigout, J., Le Breton, N., 2018. Large-scale strain localization induced by phase nucleation in mid-crustal granitoids of the south Armorican massif. *Tectonophysics* 745, 46–65. <https://doi.org/10.1016/j.tecto.2018.07.022>
- Mansard, N., Stünitz, H., Raimbourg, H., Précigout, J., 2020. The role of deformation-reaction interactions to localize strain in polymineralic rocks: Insights from experimentally deformed plagioclase-pyroxene assemblages. *Journal of Structural Geology* 134. <https://doi.org/10.1016/j.jsg.2020.104008>
- Marsh, J.H., Gerbi, C.C., Culshaw, N.G., Potter, J., Longstaffe, F.J., Johnson, S.E., 2011. Initiation and development of the Twelve Mile Bay shear zone: the low viscosity sole of a granulite nappe. *Journal of Metamorphic Geology* 29, 167–191. <https://doi.org/10.1111/j.1525-1314.2010.00913.x>

- Marti, S., Stünitz, H., Heilbronner, R., Plümper, O., Drury, M., 2017. Experimental investigation of the brittle-viscous transition in mafic rocks – Interplay between fracturing, reaction, and viscous deformation. *Journal of Structural Geology* 105, 62–79. <https://doi.org/10.1016/J.JSG.2017.10.011>
- Marti, S., Stünitz, H., Heilbronner, R., Plümper, O., Kilian, R., 2018. Syn-kinematic hydration reactions, grain size reduction, and dissolution-precipitation creep in experimentally deformed plagioclase-pyroxene mixtures. *Solid Earth* 9, 985–1009. <https://doi.org/10.5194/se-9-985-2018>
- Matsumoto, T., Dick, H.J.B., Party, A.S., 2002. Investigation of Atlantis Bank and the SW Indian Ridge from 56°E to 58°E: preliminary report. JAMSTEC Deep Sea Research, Yokosuka, Japan, p. 463.
- McAleer, R.J., Bish, D.L., Kunk, M.J., Sicard, K.R., Valley, P.M., Walsh, G.J., Wathen, B.A., Wintsch, R.P., 2017. Reaction softening by dissolution-precipitation creep in a retrograde greenschist facies ductile shear zone, New Hampshire, USA. *Journal of Metamorphic Geology* 35, 95–119. <https://doi.org/10.1111/jmg.12222>
- Mehl, L., Hirth, G., 2008. Plagioclase preferred orientation in layered mylonites: Evaluation of flow laws for the lower crust. *Journal of Geophysical Research: Solid Earth* 113, 1–19. <https://doi.org/10.1029/2007JB005075>
- Menegon, L., Fousseis, F., Stünitz, H., Xiao, X., 2015. Creep cavitation bands control porosity and fluid flow in lower crustal shear zones. *GEOLOGY* 43. <https://doi.org/10.1130/G36307.1>
- Menegon, L., Pennacchioni, G., Spiess, R., 2008. Dissolution-precipitation creep of K-feldspar in mid-crustal granite mylonites. *Journal of Structural Geology* 30, 565–579. <https://doi.org/10.1016/j.jsg.2008.02.001>
- Menegon, L., Stünitz, H., Nasipuri, P., Heilbronner, R., Svahnberg, H. 2013. Transition from fracturing to viscous flow in granulite facies perthitic feldspar (Lofoten, Norway), *J. Struct. Geol.*, 48, 95–112, <https://doi.org/10.1016/j.jsg.2012.12.004>.
- Mevel C., Cannat M., 1991. Lithospheric stretching and hydrothermal processes in oceanic gabbros from slow-spreading ridges. Peters T., Nicolas A., Coleman R.J. (Eds.), *Ophiolite Genesis and Evolution of the Oceanic Lithosphere*, Ministry of Petroleum and Minerals, Sultanate of Oman, pp. 293-312.

- Miranda, E.A., 2006. Structural Development of the Atlantis Bank Oceanic Detachment Fault System, Southwest Indian Ridge. University of Wyoming. Ph.D. dissertation.
- Miranda, E.A., John, B.E., 2010. Strain localization along the Atlantis Bank oceanic detachment fault system, Southwest Indian Ridge. *Geochemistry, Geophysics, Geosystems* 11. <https://doi.org/10.1029/2009GC002646>
- Moghadam, R.H., Trepmann, C.A., Stöckhert, B., Renner, J., 2010. Rheology of Synthetic Omphacite Aggregates at High Pressure and High Temperature. *Journal of Petrology* 51, 921–945. <https://doi.org/10.1093/petrology/egq006>
- Mukai, H., Austrheim, H., Putnis, C. V., Putnis, A., 2014. Textural evolution of plagioclase feldspar across a shear zone: Implications for deformation mechanism and rock strength. *Journal of Petrology* 55, 1457–1477. <https://doi.org/10.1093/petrology/egu030>
- Okudaira, T., Jerabek, P., Stunitz, H., Füsseis, F., 2015. High-temperature fracturing and subsequent grain-size- sensitive creep in lower crustal gabbros: Evidence for coseismic loading followed by creep during decaying stress in the lower crust? *Journal of Geophysical Research: Solid Earth* Solid Earth 1–23. <https://doi.org/10.1002/2014JB011708>.
- Oliot, E., Goncalves, P., Marquer, D., 2010. Role of plagioclase and reaction softening in a metagranite shear zone at mid-crustal conditions (Gotthard Massif, Swiss Central Alps). *Journal of Metamorphic Geology* 28, 849–871. <https://doi.org/10.1111/j.1525-1314.2010.00897.x>
- Oliot, E., Goncalves, P., Schulmann, K., Marquer, D., Lexa, O., 2014. Mid-crustal shear zone formation in granitic rocks: Constraints from quantitative textural and crystallographic preferred orientations analyses, *Tectonophysics*, 612-613, 63-80.
- Orzol, J., Trepmann, C.A., Stöckhert, B., Shi, G., 2003. Critical shear stress for mechanical twinning of jadeite—an experimental study. *Tectonophysics* 372, 135–145. [https://doi.org/10.1016/S0040-1951\(03\)00242-7](https://doi.org/10.1016/S0040-1951(03)00242-7)
- Papeschi, S., Musumeci, G., 2019. Fluid-Assisted Strain Localization in Quartz at the Brittle/Ductile Transition. *Geochemistry, Geophysics, Geosystems* 20, 3044–

3064. <https://doi.org/10.1029/2019GC008270>

Passchier, C.W., Trouw R. 2005 *Microtectonics*. Springer, Berlin, Heidelberg, 366 p.
<https://doi.org/10.1007/3-540-29359-0>

Pennacchioni, G., Mancktelow, N.S., 2018. Small-scale ductile shear zones: Neither extending, nor thickening, nor narrowing. *Earth-Science Reviews* 184, 1–12.
<https://doi.org/10.1016/J.EARSCIREV.2018.06.004>

Pennacchioni, G., Mancktelow, N.S., 2007. Nucleation and initial growth of a shear zone network within compositionally and structurally heterogeneous granitoids under amphibolite facies conditions. *Journal of Structural Geology* 29, 1757–1780. <https://doi.org/10.1016/J.JSG.2007.06.002>

Pettigrew, T.L., Casey, J.F., Miller, D.J., 1999. The scientific party. In: *Proceedings of the Ocean Drilling Program*. (Ocean Drilling Program), College Station, TX, p. 179.
<https://doi.org/10.2973/odp.proc.ir.179>. Initial Reports.

Piepenbreier, D., Stöckhert, B., 2001. Plastic flow of omphacite in eclogites at temperatures below 500°C – implications for interplate coupling in subduction zones. *International Journal of Earth Sciences* 90, 197–210.
<https://doi.org/10.1007/s005310000159>

Platt, J.P., 2015. Rheology of two-phase systems: A microphysical and observational approach. *Journal of Structural Geology* 77, 213–227.
<https://doi.org/10.1016/j.jsg.2015.05.003>

Pollitz, F.F., Wicks, C., Thatcher, W., 2001. Mantle Flow Beneath a Continental Strike-Slip Fault: Postseismic Deformation After the 1999 Hector Mine Earthquake. *Science* 293, 1814–1818. <https://doi.org/10.1126/science.1061361>

Précigout, J., Stünitz, H., 2016. Evidence of phase nucleation during olivine diffusion creep: A new perspective for mantle strain localisation. *Earth and Planetary Science Letters* 455, 94–105. <https://doi.org/10.1016/J.EPSL.2016.09.029>

Putnis, A., Austrheim, H. 2010. Fluid-induced processes: meta- somatism and metamorphism. *Geofluids* 10, 254-269.

Raimbourg, H., Toyoshima, T., Harima, Y., Kimura, G., 2008. Grain-size reduction mechanisms and rheological consequences in high-temperature gabbro mylonites of Hidaka, Japan. *Earth and Planetary Science Letters* 267, 637–653.

<https://doi.org/10.1016/J.EPSL.2007.12.012>

- Ranero, C.R., Reston, T.J. 1999. Detachment faulting at ocean core complexes: *Geology*, v. 27, p. 983–986, doi:10.1130/0091-7613(1999)027<0983:DFAOCC>2.3.CO;2.
- Raterron, P., Doukhan, N., Jaoul, O., Doukhan, J.C., 1994. High temperature deformation of diopside IV: predominance of {110} glide above 1000°C. *Physics of the Earth and Planetary Interiors* 82, 209–222. [https://doi.org/10.1016/0031-9201\(94\)90073-6](https://doi.org/10.1016/0031-9201(94)90073-6)
- Reyners, M., Eberhart-Phillips, D., Stuart, G., 2007. The role of fluids in lower-crustal earthquakes near continental rifts. *Nature* 446, 1075–1078. <https://doi.org/10.1038/nature05743>
- Rutter, E.H., 1983. Pressure solution in nature, theory and experiment. *Journal of the Geological Society* 140, 725–740. <https://doi.org/10.1144/gsjgs.140.5.0725>
- Ryan, W.B.F., Carbotte, S.M., Coplan, S., O'Hara, A., Melkonian, A., Arko, R., Weissel, R.A., Ferrini, V., Goodwillie, A., Nitcher, F., Bonczkowski, J., Zensky, R., 2009. Global multi-resolution topography (GMRT) synthesis data set. *G-cubed* 10, Q03014.
- Sammis, C.G., Osborne, R.H., Anderson, J.L., Banerdt, M., White, P., 1986. Self-similar cataclasis in the formation of fault gouge. *Pure and Applied Geophysics PAGEOPH* 124, 53–78. <https://doi.org/10.1007/BF00875719>
- Scambelluri, M., Fiebig, J., Malaspina, N., Müntener, O., Pettke, T., 2004. Serpentinite Subduction: Implications for Fluid Processes and Trace-Element Recycling. *International Geology Review* 46, 595–613. <https://doi.org/10.2747/0020-6814.46.7.595>
- Schmid, S.M., 1983. Microfabric studies as indicators of deformation mechanisms and flow laws operative in mountain building. *Mountain Building Processes* 95–110.
- Segall, P., Simpson, C., 1986. Nucleation of ductile shear zones on dilatant fractures. *Geology* 14, 56–59.
- Shipboard Scientific Party, 1989. Site 735, proc. Ocean drill. Program Initial Rep 118, 89–222. <https://doi.org/10.2973/odp.proc.ir.118.107.1989>.

- Shipboard Scientific Party, 1999a. Leg 179 summary. *Proc. Ocean Drill. Progr. Initial Rep.* 179, 1–26. <https://doi.org/10.2973/odp.proc.ir.179.101.1999>.
- Shipboard Scientific Party, 1999b. Leg 176 summary. *Proc. Ocean Drill. Progr. Initial Rep.* 176, 1–70. <https://doi.org/10.2973/odp.proc.ir.176.101.1999>.
- Skemer, P., Karato, S., 2008. Sheared Iherzolite xenoliths revisited. *Journal of Geophysical Research* 113, B07205. <https://doi.org/10.1029/2007JB005286>
- Skrotzki, W., Wedel, A., Weber, K., Muller, W.F., 1990. Microstructure and texture in Iherzolites of the Balmuccia massif and their significance regarding the thermomechanical history. *Tectonophysics* 179, 227–251.
- Spiess, R., Dibona, R., Faccenda, M., Mattioli, M., Renzulli, A., 2017. Mylonitic gabbro nodules of Stromboli (southern Italy): microstructural evidence of high-temperature deformation of cumulates during the evolution of the magmatic crustal roots of an active volcano. In: Bianchini, G., Bodinier, J.-L., Braga, R., Wilson, M. (Eds.), *The Crust-Mantle and Lithosphere-Asthenosphere Boundaries: Insights from Xenoliths, Orogenic Deep Sections, and Geophysical Studies*, vol. 526. Geological Society of America Special Paper, pp. 89–105. [https://doi.org/10.1130/2017.2526\(05\)](https://doi.org/10.1130/2017.2526(05)).
- Stakes, D., Mével, C., Cannat, M., Chaput, T., 1991. Metamorphic stratigraphy of Hole 735B. *Proceedings of the Ocean Drilling Program, Scientific Results.* 153–180.
- Stokes, M.R., Wintsch, R.P., Southworth, C.S., 2012. Deformation of amphibolites via dissolution–precipitation creep in the middle and lower crust. *Journal of Metamorphic Geology* 30, 723–737. <https://doi.org/10.1111/j.1525-1314.2012.00989.x>
- Stuart, C. A., Piazzolo, S., and Daczko, N. R., 2016. Mass transfer in the lower crust: Evidence for incipient melt assisted flow along grain boundaries in the deep arc granulites of Fiordland, New Zealand, *Geochem. Geophys. Geosyst.*, 17, 3733–3753, doi:10.1002/2015GC006236.
- Stuart, C.A., Piazzolo, S., Daczko, N.R., 2018. The recognition of former melt flux through high-strain zones. *Journal of Metamorphic Geology* 36, 1049–1069. <https://doi.org/10.1111/jmg.12427>
- Stünitz, H., 1998 Syndeformational recrystallization – dynamic or compositionally

induced? *Contrib. Mineral. Petr.*, 131, 219–236, <https://doi.org/10.1007/s004100050390>.

Stünitz, H., Fitz Gerald, J., Tullis, J., 2003. Dislocation generation, slip systems, and dynamic recrystallization in experimentally deformed plagioclase single crystals. *Tectonophysics* 372, 215–233. [https://doi.org/10.1016/S0040-1951\(03\)00241-5](https://doi.org/10.1016/S0040-1951(03)00241-5)

Stünitz, H., Neufeld, K., Heilbronner, R., Finstad, A.K., Konopásek, J., Mackenzie, J.R., 2020. Transformation weakening: Diffusion creep in eclogites as a result of interaction of mineral reactions and deformation. *Journal of Structural Geology* 139, 104129. <https://doi.org/10.1016/J.JSG.2020.104129>

Stünitz, H., Tullis, J., 2001. Weakening and strain localization produced by syn-deformational reaction of plagioclase. *International Journal of Earth Sciences* 90, 136–148. <https://doi.org/10.1007/s005310000148>

Svahnberg, H., Piazzolo, S., 2010. The initiation of strain localisation in plagioclase-rich rocks: Insights from detailed microstructural analyses. *Journal of Structural Geology* 32, 1404–1416. <https://doi.org/10.1016/J.JSG.2010.06.011>

Taufner, R., Viegas, G., Faleiros, F.M., Castellan, P., Silva, R., 2021. Deformation mechanisms of granulite-facies mafic shear zones from hole U1473A, Atlantis Bank, Southwest Indian Ridge (IODP Expedition 360). *Journal of Structural Geology* 149, 104380. <https://doi.org/10.1016/j.jsg.2021.104380>

Thatcher, W., Pollitz, F.F., 2008. Temporal evolution of continental lithospheric strength in actively deforming regions. *GSA Today*: V 18. <https://doi.org/10.1130/GSAT01804-5A.1>

Trepmann, C.A., Hsu, C., Hentschel, F., Döhler, K., Schneider, C., Wichmann, V., 2017. Recrystallization of quartz after low-temperature plasticity – The record of stress relaxation below the seismogenic zone. *Journal of Structural Geology* 95, 77–92. <https://doi.org/10.1016/j.jsg.2016.12.004>

Trepmann, C.A., Stöckhert, B., 2009. Microfabric of folded quartz veins in metagreywackes: dislocation creep and subgrain rotation at high stress. *Journal of Metamorphic Geology* 27, 555–570. <https://doi.org/10.1111/j.1525-1314.2009.00842.x>

Trepmann, C.A., Stöckhert, B., Dorner, D., Moghadam, R.H., Küster, M., Röller, K.,

2007. Simulating coseismic deformation of quartz in the middle crust and fabric evolution during postseismic stress relaxation - An experimental study. *Tectonophysics* 442, 83–104. <https://doi.org/10.1016/j.tecto.2007.05.005>
- Tucholke, B.E., Lin, J., Kleinrock, M.C., 1998. Megamullions and mullion structure defining oceanic metamorphic core complexes on the Mid-Atlantic Ridge. *Journal of Geophysical Research: Solid Earth* 103, 9857–9866. <https://doi.org/10.1029/98JB00167>
- Tullis, J., Yund, R.A., 1987. Transition from cataclastic flow to dislocation creep of feldspar: mechanisms and microstructures. *Geology* 15, 606–609.
- Van Der Werf, T., Chatzaras, V., Marcel Kriegsman, L., Kronenberg, A., Tikoff, B., Drury, M.R., 2017. Constraints on the rheology of the lower crust in a strike-slip plate boundary: Evidence from the San Quintín xenoliths, Baja California, Mexico. *Solid Earth* 8, 1211–1239. <https://doi.org/10.5194/se-8-1211-2017>
- Viegas, G., Menegon, L., Archanjo, C., 2016. Brittle grain-size reduction of feldspar, phase mixing and strain localization in granitoids at mid-crustal conditions (Pernambuco shear zone, NE Brazil). *Solid Earth* 7, 375–396. <https://doi.org/10.5194/se-7-375-2016>
- Wassmann, S., Stöckhert, B., 2013. Rheology of the plate interface — Dissolution precipitation creep in high pressure metamorphic rocks. *Tectonophysics* 608, 1–29. <https://doi.org/10.1016/J.TECTO.2013.09.030>
- White, J.C., 1996. Transient discontinuities revisited: pseudotachylyte, plastic instability and the influence of low pore fluid pressure on deformation processes in the mid-crust. *Journal of Structural Geology* 18, 1471–1486. [https://doi.org/10.1016/S0191-8141\(96\)00059-4](https://doi.org/10.1016/S0191-8141(96)00059-4)
- White, S., 1979. Grain and Sub-Grain Size Variations Across a Mylonite Zone, *Contrib. Mineral. Petrol.*
- White, S.H., Knipe, R.J., 1978. Transformation- and reaction-enhanced ductility in rocks. *Journal of the Geological Society* 135, 513–516. <https://doi.org/10.1144/gsjgs.135.5.0513>
- Wolfe, C.J., Purdy, G.M., Toomey, D.R., Solomon, S.C., 1995. Microearthquake characteristics and crustal velocity structure at 29°N on the Mid-Atlantic Ridge:

The architecture of a slow spreading segment. *Journal of Geophysical Research: Solid Earth* 100, 24449–24472. <https://doi.org/10.1029/95JB02399>

Zhang, J., Green, H.W., Bozhilov, K.N., 2006. Rheology of omphacite at high temperature and pressure and significance of its lattice preferred orientations. *Earth and Planetary Science Letters* 246, 432–443. <https://doi.org/10.1016/J.EPSL.2006.04.006>

CHAPTER 6

6 Final remarks

The petrostructural analyses of mylonites and ultramylonites in gabbroic shear zones from the lower parts of Site U1473A in the Atlantis Bank oceanic core complex (Southwest Indian Ridge) indicate that deformation occurred at high temperature conditions, in the presence of fluids. Deformation was primarily achieved by intracrystalline plasticity and brittle deformation associated with channeling of fluids assisting grain size sensitive mechanisms in highly localized zones in the long term. The polyphase matrix formed as a result of phase mixing and grain size reduction which localized the deformation by diffusion-assisted-GBS. The percolation of fluids into the shear zones contributes for decreasing the grain size of the aggregate by promoting reaction-softening mechanisms.

Taken together, these observations evidence that fluid-rock interaction in shear zones at the lower crust may be more ubiquitous than previously thought, highlighting the importance of shear zones in channeling fluids at the deepest parts of the crust. Strain tends to localize in zones of phase mixing and fine grain size, in which fluids promote reaction-softening and significantly affect the overall rheological behaviour of the lower oceanic crust. Such fluid-rock interactions are heterogeneous and point out to the way strain is distributed in the footwall of oceanic core complexes during large-scale, detachment faulting.

References

- Blackman, D.K., Cann, J.R., Janssen, B., Smith, D.K., 1998. Origin of extensional core complexes: Evidence from the Mid-Atlantic Ridge at Atlantis Fracture Zone. *Journal of Geophysical Research: Solid Earth* 103, 21315–21333. <https://doi.org/10.1029/98JB01756>
- Brun, J.P., Sokoutis, D., Tirel, C., Gueydan, F., Van Den Driessche, J., Beslier, M.O., 2018. Crustal versus mantle core complexes. *Tectonophysics* 746, 22–45. <https://doi.org/10.1016/j.tecto.2017.09.017>
- Bürgmann, R., Dresen, G., 2008. Rheology of the Lower Crust and Upper Mantle: Evidence from Rock Mechanics, Geodesy, and Field Observations. *Annu. Rev. Earth Planet. Sci.* 36, 531–567. <https://doi.org/10.1146/annurev.earth.36.031207.124326>
- Canales, J.P., Tucholke, B.E., Collins, J.A., 2004. Seismic reflection imaging of an oceanic detachment fault: Atlantis megamullion (Mid-Atlantic Ridge, 30°10' N). *Earth Planet. Sci. Lett.* 222, 543–560.
- Cann, J.R., Blackman, D.K., Smith, D.K., McAllister, E., Janssen, B., Mello, S., Avgerinos, E., Pascos, A.R., Escartin, J., 1997. Corrugated slip surfaces formed at ridge-transform intersections on the Mid-Atlantic Ridge. *Nature* 385, 329–332.
- Cannat, M., 1991. Plastic Deformation at an Oceanic Spreading Ridge: A Microstructural Study of Site 735 Gabbros (Southwest Indian Ocean), in: *Proceedings of the Ocean Drilling Program, 118 Scientific Results. Ocean Drilling Program.* <https://doi.org/10.2973/odp.proc.sr.118.134.1991>
- Cannat, M., Sauter, D., Mendel, V., Ruellan, E., Okino, K., Escartin, J., Combier, V., Baala, M., 2006. Modes of seafloor generation at a melt-poor ultraslow-spreading ridge. *Geology* 34, 605. <https://doi.org/10.1130/G22486A.1>
- Dick, H.J.B., Kvassnes, A.J.S., Robinson, P.T., MacLeod, C.J., Kinoshita, H., 2019. The Atlantis Bank Gabbro Massif, Southwest Indian Ridge. *Progress in Earth and Planetary Science* 6, 64. <https://doi.org/10.1186/s40645-019-0307-9>
- Dick, H.J.B., Meyer, P.S., Bloomer, S., Kirby, S., Stakes, D., Mawer, C., 1991. Lithostratigraphic Evolution of an In-Situ Section of Oceanic Layer 3, in: *Proceedings of the Ocean Drilling Program, 118 Scientific Results. Ocean Drilling*

Program. <https://doi.org/10.2973/odp.proc.sr.118.128.1991>

Dick, H.J.B., Natland, J.H., Alt, J.C., Bach, W., Bideau, D., Gee, J.S., Haggas, S., Hertogen, J.G.H., Hirth, G., Holm, P.M., Ildefonse, B., Iturrino, G.J., John, B.E., Kelley, D.S., Kikawa, E., Kingdon, A., LeRoux, P.J., Maeda, J., Meyer, P.S., Miller, D.J., Naslund, H.R., Niu, Y.-L., Robinson, P.T., Snow, J., Stephen, R.A., Trimby, P.W., Worm, H.-U., Yoshinobu, A., 2000. A long in situ section of the lower ocean crust: results of ODP Leg 176 drilling at the Southwest Indian Ridge. *Earth and Planetary Science Letters* 179, 31–51. [https://doi.org/10.1016/S0012-821X\(00\)00102-3](https://doi.org/10.1016/S0012-821X(00)00102-3)

Dimanov, A., Dresen, G., 2005. Rheology of synthetic anorthite-diopside aggregates: Implications for ductile shear zones. *Journal of Geophysical Research* 110, B07203. <https://doi.org/10.1029/2004JB003431>

Dimanov, A., Rybacki, E., Wirth, R., Dresen, G., 2007. Creep and strain-dependent microstructures of synthetic anorthite-diopside aggregates. *Journal of Structural Geology* 29, 1049–1069. <https://doi.org/10.1016/j.jsg.2007.02.010>

Escartín, J., Mével, C., MacLeod, C.J., McCaig, A.M., 2003. Constraints on deformation conditions and the origin of oceanic detachments: The Mid-Atlantic Ridge core complex at 15°45'N. *Geochemistry, Geophysics, Geosystems* 4. <https://doi.org/10.1029/2002GC000472>

Goldstein, J., 2003. *Scanning electron microscopy and x-ray microanalysis*. Kluwer Academic/Plenum Publishers, 689 p.

Handy, M. R., Hirth, G., Bürgmann, R., 2007. Continental fault structure and rheology from the frictional-to-viscous transition downward. In M. Handy, G. Hirth, & N. Hovius (Eds.), *Tectonic faults: Agents of change on a dynamic Earth*, 131–181. Cambridge, Mass, Berlin: MIT Press; in cooperation with the Freie Universität Berlin.

Hansen, L.N., Cheadle, M.J., John, B.E., Swapp, S.M., Dick, H.J.B., Tucholke, B.E., Tivey, M.A., 2013. Mylonitic deformation at the Kane oceanic core complex: Implications for the rheological behavior of oceanic detachment faults. *Geochemistry, Geophysics, Geosystems* 14, 3085–3108. <https://doi.org/10.1002/ggge.20184>

- Hirth, G., Teyssier, C., Dunlap, J.W., 2001. An evaluation of quartzite flow laws based on comparisons between experimentally and naturally deformed rocks. *Int. J. Earth Sci.* 90, 77–87. <https://doi.org/10.1007/s005310000152>
- Ildefonse, B., Blackman, D.K., John, B.E., Ohara, Y., Miller, D.J., MacLeod, C.J., 2007. Oceanic core complexes and crustal accretion at slow-spreading ridges. *Geology* 35, 623–626. <https://doi.org/10.1130/G23531A.1>
- Johnson, E., Rossman, G.R., 2003. The concentration and speciation of hydrogen in feldspars using FTIR and ¹H MAS NMR spectroscopy. *American Mineralogist* 88, 901–911.
- Koga, K., Hauri, E., Hirschmann, M., Bell, D., 2003. Hydrogen concentration analyses using SIMS and FTIR: Comparison and calibration for nominally anhydrous minerals. *Geochemistry, Geophys. Geosystems* 4. <https://doi.org/10.1029/2002GC000378>
- Lavier, L. L., Buck, W. R., Poliakov, A. N. B., 1999. Self-consistent rolling-hinge model for the evolution of large-offset low-angle normal faults. *Geology* 27(12), 1127–1130, doi:10.1130/0091-7613(1999)027<1127:SCR HMF>2.3.CO;2
- MacLeod, C. J., Escartín, J., Banerji, D., Banks, G. J., Gleeson, M., Irving, D. H. B., Lilly, R. M., McCaig, A. M., Niu, Y., Allerton, S., Smith, D. K., 2002. Direct geological evidence for oceanic detachment faulting: The Mid-Atlantic Ridge, 15°45'N, *Geology*, 30(10), 879–882, doi:10.1130/0091-7613(2002)030<0879:DGEFOD>2.0.CO;2. MacLeod,
- MacLeod, C.J., Searle, R.C., Murton, B.J., Casey, J.F., Mallows, C., Unsworth, S.C., Achenbach, K.L., Harris, M., 2009. Life cycle of oceanic core complexes. *Earth and Planetary Science Letters* 287, 333–344. <https://doi.org/10.1016/J.EPSL.2009.08.016>
- Mehl, L., Hirth, G., 2008. Plagioclase preferred orientation in layered mylonites: Evaluation of flow laws for the lower crust. *Journal of Geophysical Research: Solid Earth* 113. <https://doi.org/10.1029/2007JB005075>
- Mezri, L., Le Pourhiet, L., Wolf, S., Burov, E., 2015. New parametric implementation of metamorphic reactions limited by water content, impact on exhumation along detachment faults. *Lithos* 236–237, 287–298.

- Miranda, E.A., John, B.E., 2010. Strain localization along the Atlantis Bank oceanic detachment fault system, Southwest Indian Ridge. *Geochemistry, Geophysics, Geosystems* 11. <https://doi.org/10.1029/2009GC002646>
- Mori, T., Onaka, S., Wakashima, K., 1998. Role of grain boundary sliding in diffusional creep of polycrystals. *Journal of Applied Physics* 83, 7547±7552
- Paterson, M.S., 1982. The determination of hydroxyl by infrared absorption in quartz, silicate glasses and similar materials. *Bulletin de Mineralogie* 105, 20–29.
- Prior, D. J., Boyle, A.P. et al. (1999). *Amer. Mineral.*, 84, 1741-1759.
- Ranero, C. R., and T. J. Reston (1999), Detachment faulting at ocean core complexes, *Geology*, 27, 983–986, doi:10.1130/0091-7613(1999)027<0983:DFAOCC>2.3.CO;2
- Schroeder, T., John, B.E., 2004. Strain localization on an oceanic detachment fault system, Atlantis Massif, 30°N, Mid-Atlantic Ridge. *Geochemistry, Geophysics, Geosystems* 5, 1–30. <https://doi.org/10.1029/2004GC000728>
- Smith, D.K., Cann, J.R., 1993. Building the crust at the Mid-Atlantic Ridge. *Nature* 365, 707–715. <https://doi.org/10.1038/365707a0>
- Smith, D.K., Cann, J.R., Escartín, J., 2006. Widespread active detachment faulting and core complex formation near 13° N on the Mid-Atlantic Ridge. *Nature* 442, 440–443. <https://doi.org/10.1038/nature04950>
- Tucholke, B.E., Fujioka, K., Ishihara, T., Hirth, G., Kinoshita, M., 2001. Submersible study of an oceanic megamullion in the central North Atlantic. *Journal of Geophysical Research: Solid Earth* 106, 16145–16161. <https://doi.org/10.1029/2001JB000373>
- Tucholke, B.E., Lin, J., Kleinrock, M.C., 1998. Megamullions and mullion structure defining oceanic metamorphic core complexes on the Mid-Atlantic Ridge. *Journal of Geophysical Research: Solid Earth* 103, 9857–9866. <https://doi.org/10.1029/98JB00167>
- Whitney, D.L., Teyssier, C., Rey, P., Buck, W.R., 2013. Continental and oceanic core complexes. *Geol. Soc. Am. Bull.* 125, 273–298
- Schroeder, T., John, B.E., 2004. Strain localization on an oceanic detachment fault

system, Atlantis Massif, 30°N, Mid-Atlantic Ridge. *Geochemistry, Geophysics, Geosystems* 5, 1–30. <https://doi.org/10.1029/2004GC000728>